

NPS-OC-98-003

# NAVAL POSTGRADUATE SCHOOL MONTEREY, CALIFORNIA



## THESIS

**A WIND-FORCED MODELING STUDY OF THE  
CANARY CURRENT SYSTEM FROM**

**30° N TO 42.5° N**

by

Daniel W. Bryan

June 1998

Thesis Advisor:

Mary L. Batteen

Approved for public release; distribution is unlimited.

Prepared for:  
Office of Naval Research  
800 N. Quincy Street  
Arlington, VA 22217

**DTIC QUALITY INSPECTED 1**

19980810 034

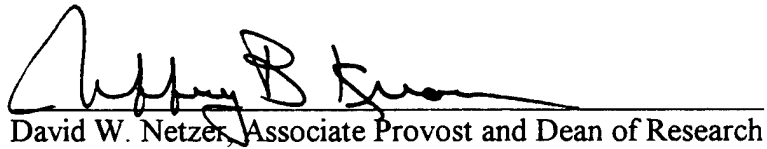
**NAVAL POSTGRADUATE SCHOOL  
MONTEREY, CALIFORNIA 93943**

Rear Admiral Robert C. Chaplin  
Superintendent

This thesis was prepared in conjunction with research sponsored in part by the Office of Naval Research, 800 N. Quincy Street, Arlington, VA 22217.

Reproduction of all or part of this report is authorized.

Released by:

  
David W. Netzer, Associate Provost and Dean of Research

# REPORT DOCUMENTATION PAGE

Form Approved OMB No. 0704-0188

Public reporting burden for this collection of information is estimated to average 1 hour per response, including the time for reviewing instruction, searching existing data sources, gathering and maintaining the data needed, and completing and reviewing the collection of information. Send comments regarding this burden estimate or any other aspect of this collection of information, including suggestions for reducing this burden, to Washington Headquarters Services, Directorate for Information Operations and Reports, 1215 Jefferson Davis Highway, Suite 1204, Arlington, VA 22202-4302, and to the Office of Management and Budget, Paperwork Reduction Project (0704-0188) Washington DC 20503.

|  |  |   |                                  |
|--|--|---|----------------------------------|
| 1. AGENCY USE ONLY <i>(Leave blank)</i>  | 2. REPORT DATE<br>June 1998                              | 3. REPORT TYPE AND DATES COVERED<br>Master's Thesis   |                                  |
| 4. TITLE AND SUBTITLE<br>A WIND-FORCED MODELING STUDY OF THE CANARY CURRENT SYSTEM FROM 30° N TO 42.5° N   |  | 5. FUNDING NUMBERS  |                                  |
| 6. AUTHOR(S)<br>Daniel W. Bryan in conjunction with Mary L. Batteen and Eric J. Buch   |  | 8. PERFORMING ORGANIZATION REPORT NUMBER<br>NPS-OC-98-003   |                                  |
| 7. PERFORMING ORGANIZATION NAME(S) AND ADDRESS(ES)<br>Naval Postgraduate School<br>Monterey, CA 93943-5000   |  | 10. SPONSORING/MONITORING AGENCY REPORT NUMBER  |                                  |
| 9. SPONSORING/MONITORING AGENCY NAME(S) AND ADDRESS(ES)<br>Office of Naval Research<br>800 N. Quincy Street, Arlington, VA 22217   |  | 11. SUPPLEMENTARY NOTES<br>The views expressed in this thesis are those of the author and do not reflect the official policy or position of the Department of Defense or the U.S. Government. |                                  |
| 12a. DISTRIBUTION/AVAILABILITY STATEMENT<br>Approved for public release; distribution is unlimited.  |  | 12b. DISTRIBUTION CODE  |                                  |
| 13. ABSTRACT <i>(maximum 200 words)</i><br>A high-resolution, multi-level, primitive equation ocean model is used to investigate the roles of wind forcing and irregular coastline geometry in the generation of currents, eddies, jets and filaments in the Canary Current System (CCS) from 30° N to 42.5° N. To study the generation, evolution, and sustainment of the currents, eddies, jets and filaments in the CCS, the model is forced from rest using seasonal climatological winds and a realistic coastline. Results of the experiment show that wind forcing alone is capable of generating surface currents, undercurrents, meanders, eddies, and filaments. Preferred eddy generation locations, enhanced growth of meanders, eddies, and filaments are seen. The features produced by the model are consistent with available observations of the CCS. |  |   |                                  |
| SUBJECT TERMS<br>Primitive equation model, Canary Current System, currents, meanders, eddies, filaments  |  | 15. NUMBER OF PAGES<br>96   | 16. PRICE CODE                   |
| 17. SECURITY CLASSIFICATION OF REPORT<br>Unclassified  | 18. SECURITY CLASSIFICATION OF THIS PAGE<br>Unclassified | 19. SECURITY CLASSIFICATION OF ABSTRACT<br>Unclassified   | 20. LIMITATION OF ABSTRACT<br>UL |



Approved for public release; distribution is unlimited.

**A WIND-FORCED MODELING STUDY OF THE CANARY CURRENT SYSTEM  
FROM 30° N TO 42.5° N**

Daniel W. Bryan  
Lieutenant, United States Navy  
B.S., United States Naval Academy, 1990

Submitted in partial fulfillment  
of the requirements for the degree of

**MASTER OF SCIENCE IN PHYSICAL OCEANOGRAPHY**

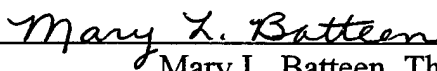
from the

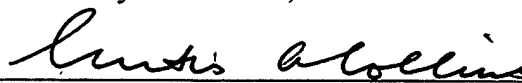
**NAVAL POSTGRADUATE SCHOOL  
June 1998**

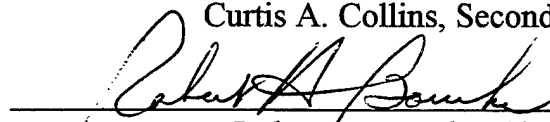
Author:

  
\_\_\_\_\_  
Daniel W. Bryan

Approved by:

  
\_\_\_\_\_  
Mary L. Batteen, Thesis Advisor

  
\_\_\_\_\_  
Curtis A. Collins, Second Reader

  
\_\_\_\_\_  
Robert H. Bourke, Chairman  
Department of Oceanography



## **ABSTRACT**

A high-resolution, multi-level, primitive equation ocean model is used to investigate the roles of wind forcing and irregular coastline geometry in the generation of currents, eddies, jets and filaments in the Canary Current System (CCS) from 30° N to 42.5° N. To study the generation, evolution, and sustainment of the currents, eddies, jets and filaments in the CCS, the model is forced from rest using seasonal climatological winds and a realistic coastline. Results of the experiment show that wind forcing alone is capable of generating surface currents, undercurrents, meanders, eddies, and filaments. Preferred eddy generation locations, enhanced growth of meanders, eddies, and filaments are seen. The features produced by the model are consistent with available observations of the CCS.





## TABLE OF CONTENTS

|      |  |    |
|------|--|----|
| I.   | INTRODUCTION.....                                      | 1  |
| II.  | MODEL DESCRIPTION.....                                 | 5  |
|      | A.    MODEL EQUATIONS.....                             | 5  |
|      | B.    TYPE OF WIND FORCING.....                        | 7  |
|      | C.    EXPERIMENTAL DESIGN.....                         | 8  |
| III. | RESULTS FROM THE MODEL SIMULATION .....                | 11 |
|      | A.    SPIN-UP PHASE .....                              | 11 |
|      | B.    QUASI-EQUILBRIUM PHASE .....                     | 12 |
|      | C.    COMPARISONS OF MODEL RESULTS WITH OBSERVATIONS.. | 15 |
|      | 1.    Comparison of Ocean Currents.....                | 16 |
|      | 2.    Comparison of Eddies .....                       | 17 |
|      | 3.    Comparison of Upwelling.....                     | 17 |
|      | 4.    Comparison of Filaments .....                    | 18 |
| IV.  | SUMMARY .....  | 21 |
|      | APPENDIX. METHOD OF SOLUTION.....                      | 67 |
|      | LIST OF REFERENCES .....                               | 73 |
|      | INITIAL DISTRIBUTION LIST .....                        | 79 |



## LIST OF FIGURES

1. The model domain for the Canary Current System (CCS) is bounded by  $30^{\circ}$  N to  $42.5^{\circ}$  N,  $5^{\circ}$  W to  $17.5^{\circ}$  W. The cross-shore (alongshore) resolution is 9 km (11 km). Geographic locations and prominent features are labeled. .... 25
2. Climatological (1980-1989) ECMWF winds in m/s for: (a) February, (b) July, (c) September, and (d) November. Maximum wind vector is 10 m/s. .... 26
3. Figure 3. Temperature contours and velocity vectors at 30 m depth at days (a) 150, (b) 195, (c) 285 and (d) 360. The contour interval is  $1^{\circ}$ C. To avoid clutter, the velocity vectors are plotted every third grid point in the cross-shore direction and every fourth grid point in the along-shore direction. Maximum current velocity is 100 cm/s. .... 30
4. Cross-shore sections of isotherms on day 195 at (a)  $33^{\circ}$  N and (b)  $39^{\circ}$  N. Contour interval is  $1^{\circ}$  C. .... 34
5. Cross-shore sections of meridional velocity ( $v$ ) on day 240 at (a)  $39.5^{\circ}$  N, and (b)  $35.5^{\circ}$  N. Solid lines indicate poleward flow, while dashed lines indicate equatorward flow. The contour interval is 2.5 cm/s for poleward flow and 5 cm/s for equatorward flow. .... 36
6. Figure 6. Temperature contours (b-e) and velocity vectors (a-e) at 30 m depth in the third year of the model simulation time-averaged over the months of (a) January, (b) June, (c) August, (d) September and (e) November. The contour interval is  $1^{\circ}$  C. Maximum current velocity is 100 cm/s. .... 38
7. Cross-shore sections of meridional velocity ( $v$ ) in the third year of model simulation time-averaged for (a) January at  $39.4^{\circ}$  N, (b) June at  $38^{\circ}$  N and (c)  $38.6^{\circ}$  N, (d) August at  $37.5^{\circ}$  N, and (e) December at  $41.5^{\circ}$  N. Solid lines indicate poleward flow, while dashed lines indicate equatorward flow. The contour interval is 2.5 cm/s for poleward flow in (a), (d) and (e), 5 cm/s for poleward flow in (b) and (c), and 5 cm/s for equatorward flow. .... 43

8. Time-averaged plots for the peak upwelling season (July-September) of temperature contours and velocity vectors (a) at 30 m depth and (d) at 1226 m depth, and a cross-shore section of velocity ( $v$ ) at (b) 37.5° N, (c) 39° N and (e) 37.4° N. The contour interval is 1° C in (a). The maximum current velocity is 100 cm/s in (a) and 40 cm/s in (d). In (b), (c) and (d) solid lines indicate poleward flow, while dashed lines indicate equatorward flow. The contour interval for poleward flow is 2.5 cm/s in (b) and (c) and 5 cm/s in (e). The contour interval for equatorward flow is 5 cm/s. .... 48
9. (a) Mean and (b) eddy kinetic energy at 30 m depth for the peak upwelling season (July through September). Contour interval is 100 cm<sup>2</sup>/s<sup>2</sup>. .... 53
10. Computer representation of AVHRR NOAA7 Sea Surface Temperatures (SST) with observed eddy formations from 5 August 1982. "After Fiuza 1984." ..... 55
11. Temperature contours and velocity vectors at 30 m showing upwelling in the third year at day (a) 137, (b) 152, (c) 173, (d) 209, (e) 263, (f) 290, and (g) 317. The contour interval is 1° C. The maximum current velocity is 100 cm/s. .... 56
12. AVHRR sea surface temperatures (SST) from (a) 21 June 1995 showing increased cold SST southwest of Cabo de Sao Vincent caused by intensified upwelling and advection of upwelled water around the cape and (b) 27 July 1993 showing strong upwelling and numerous filaments off the west coast of the IP. In (c) SST show intense upwelling north of Cabo da Roca on 29 July 1977. Figures (a) and (b) are from the Remote Sensing Data Analysis Service (RSDAS), Plymouth Marine Laboratory, UK. Figure (c) is from Fiuza (1982). .... 63

## LIST OF TABLES

|   |    |
|---|----|
| 1. Values of Constants Used in the Model..... | 71 |
|---|----|



## ACKNOWLEDGEMENT

The professional guidance and considerable knowledge of Dr. Mary Batteen made this study possible. Hugh thanks to Pete Braccio, Mike Cook and Phaedra Green for FORTRAN, FERRET and MATLAB assistance. Thanks also to NERC Remote Sensing Data Analysis Service, Plymouth Marine Laboratory, UK for the use of their high quality AVHRR SST images (<http://www.ac.uk/rsdas>).

Finally, I would like to thank my wife for her patience and support during the last twenty-one months.





## I. INTRODUCTION

The Canary Current System (CCS) is a classical eastern boundary current (EBC) system located off the west coasts of Northwest Africa and the Iberian Peninsula (IP). It extends from  $\sim 10^\circ$  N to  $45^\circ$  N, and forms the closing, eastern boundary of the North Atlantic gyre. The climatological mean CCS consists of several large-scale currents of which the Canary Current (CC) is predominant. Like other EBCs, the CC is a broad ( $\sim 1000$  km), relatively slow ( $\sim 10$ - $30$  cm/s), equatorward, yearlong surface flow extending to depths of  $\sim 500$  m (Wooster *et al.*, 1976). The portion of the CC which lies off the west coast of the IP is occasionally referred to as the Portugal Current (e.g., Tomczak and Godfrey, 1994). Embedded in the CC are narrower, somewhat swifter flows occasionally reaching speeds of 100 cm/s (DMAH/TC, 1988)).

Beneath the CC and near the coast, a narrower ( $\sim 10$ - $40$  km) and weaker ( $\sim 2$ - $10$  cm/s) poleward undercurrent is present. While the undercurrent is usually strongest between 100 and 600 m depth (Haynes and Barton, 1990), the depth and strength of the undercurrent can vary both seasonally and latitudinally. During the winter the undercurrent shoals to the north, occasionally reaching the surface, to form a third flow component referred to as the Iberian Current (IC) (Haynes and Barton, 1990). The IC is a narrow (25-40 km), relatively weak ( $\sim 20$ - $30$  cm/s) seasonal surface poleward current found trapped near the coast against the shelf break (Fiuza, 1980; Frouin *et al.*, 1990; Haynes and Barton, 1990). Geographically, the IC is normally found north of Cabo da Roca (see Figure 1 for geographical locations) but occasionally extends south nearly to Cabo de Sao Vincent during the winter months. A second deeper undercurrent also flows poleward off the west coast of the IP. Attributed to the Mediterranean Outflow (MO), this flow has at least two main cores, a shallow core at depths of 600-900 m and a deeper core at 1100-1200 m (Ambar, 1980). An additional third, and shallower, poleward core of Mediterranean water has also been shown to exist near 400 m (Fiuza, 1979; Ambar, 1980).

The CCS is influenced predominantly by equatorward, upwelling favorable winds produced by the Azores High. The Azores High is a semi-permanent subtropical high pressure system similar in nature and behavior to its counterpart off the west coast of North America, the North Pacific Subtropical High, as described in Nelson (1977). The center of the Azores High migrates meridionally with the seasons, reaching  $\sim 27^\circ$  N, its southernmost extent, in March and ridging north to  $\sim 33^\circ$  N by August. As a result of this migration, maximum wind stress values vary temporally at given locations. The summer mean east-west pressure contrast between Portugal and the center of the Azores High is  $\sim 8$  mb. During the winter, the contrast lessens to  $\sim 1$  mb. This pressure difference results in correspondingly strong northerly to northwesterly winds during the summer and weaker northwesterly to even slight southerly winds off of northern Portugal and northwest Spain during the winter. The shift of maximum wind stress also causes the upwelling favorable winds to shift from  $\sim 27^\circ$  N near the Canary Islands in January, to  $\sim 43^\circ$  N off the IP by July. (Fiuza, 1982)

Recent observations have shown highly energetic, mesoscale features such as jet-like surface currents, meanders, eddies, and filaments superimposed on the broad, climatological mean flow of the CC and other EBCs. Specifically, satellite images of sea surface temperatures have shown several filaments extending off the coast of Portugal and northwest Spain (Fiuza *et al.*, 1989) as well as off Cape Ghir in northwest Africa (Van Camp *et al.*, 1991; Hagen *et al.*, 1996). Observations have also shown pairs of anticyclonic and cyclonic mesoscale eddies on the order of 100 km off the coast of Iberia (Fiuza, 1984). Observed during periods of predominantly equatorward, upwelling favorable winds, these features seem to be located near prominent coastal features such as capes. These observations provide evidence that wind forcing and coastal irregularities could be important mechanisms in the formation and sustainment of many of the mesoscale features found in EBC regions.

Over the past few decades numerous wind forcing models of EBCs, particularly of the California Current System, have been conducted. Early work included steady wind

stress (Pedlosky, 1974) and transient wind forcing (Philander and Yoon, 1982). The response of reduced gravity models to realistic coastal winds was investigated by Carton (1984) and Carton and Philander (1984). McCreary *et al.* (1987) conducted a series of experiments using a linear model with both transient and steady wind forcing in the California Current System. In each of these previous models, relatively weak currents (5-10 cm/s) were generated and no eddies or filaments developed.

Recent modeling studies have focused on the driving mechanisms of complex features, such as filaments, observed in EBC regions. Ikeda *et al.* (1984a, b) and Haidvogel *et al.* (1991) studied baroclinic and barotropic instability, coastal irregularities, and bottom topography as possible mechanisms, while Batteen *et al.* (1989), McCreary *et al.* (1991), Pares-Sierra *et al.* (1993), and Batteen (1997) studied wind forcing as a possible generative mechanism. Recently, a multilevel primitive equation (PE) model of the California Current System from 35° N to 47.5° N was used by Batteen (1997) to study the effects of seasonal winds and coastal irregularities and by Batteen and Vance (1998) to study the additional effects of thermohaline gradients. In a more recent study Batteen and Monroe (1998) studied the contribution of seasonal wind forcing, thermohaline gradients and irregular coastline geometry to the generation of eddies and filaments for the entire California Current System, i.e., from 22.5° N to 47.5° N. The results showed that wind forcing was the dominant process responsible for many of the observed features of the California Current System.

In contrast, coastal modeling studies of the CCS have been scarce. McClain *et al.* (1986) performed the first limited modeling study in the region, using ship-derived winds to produce a large negative wind stress curl off the northwest coast of the IP, resulting in opposing equatorward and poleward surface currents. Recently Batteen *et al.* (1992) used an eddy resolving PE model with both uniform and variable wind stress, the latter computed from synoptic surface pressure analyses, to produce realistic currents as well as mesoscale eddies. This study, however, covered only a limited region of the CCS (the northwest coast of the IP) and had a straight coast in its model domain.

The objective of this study is to investigate the roles of seasonal climatological wind forcing and irregular coastline geometry in the generation of currents, eddies, jets and filaments in the CCS. The high-resolution, multi-level, PE model of Batteen and Monroe (1998) will be used. To allow larger scale eddies and elongated filaments to be generated and the model to reach quasi-equilibrium, the model will be allowed to run for ~3 years.

This study is organized as follows: the PE model, type of wind forcing, initial and specific experimental conditions, and the energy analysis technique are described in chapter II. Results of the model simulations and comparisons with observations are discussed in chapter III. A summary and discussion are presented in chapter IV.

## II. MODEL DESCRIPTION

### A. MODEL EQUATIONS

The PE numerical model used in this study was originally a coarse resolution model used by Haney (1974) to study closed basins. It has since been adapted for eddy-resolving, limited EBC regions with open northern, western, and southern boundaries by Batteen (1997). The multi-level, non-adiabatic, model uses beta-plane, hydrostatic, Boussinesq, and rigid lid approximations and has baroclinic and barotropic velocity components. Equations governing the model are as follows:

$$\frac{du}{dt} = \frac{-1}{\rho_0} \frac{\partial p}{\partial x} + fv - A_M \nabla^4 u + K_M \frac{\partial^2 u}{\partial z^2} \quad (1)$$

$$\frac{dv}{dt} = \frac{-1}{\rho_0} \frac{\partial p}{\partial y} - fu - A_M \nabla^4 v + K_M \frac{\partial^2 v}{\partial z^2} \quad (2)$$

$$\frac{\partial u}{\partial x} + \frac{\partial v}{\partial y} + \frac{\partial w}{\partial z} = 0 \quad (3)$$

$$\frac{\partial p}{\partial z} = -\rho g \quad (4)$$

$$\rho = \rho_0 [1 - \alpha(T - T_0) + \beta(S - S_0)] \quad (5)$$

$$\frac{dT}{dt} = -A_H \nabla^4 T + K_H \frac{\partial^2 T}{\partial z^2} \quad (6)$$

$$\frac{dS}{dt} = -A_H \nabla^4 S + K_H \frac{\partial^2 S}{\partial z^2} \quad (7)$$

In the above equations,  $t$  is time,  $T$  is temperature,  $S$  is salinity,  $\rho$  is density, and  $p$  is pressure. A right-handed Cartesian coordinate system  $(x,y,z)$  is used where  $x$  points toward shore,  $y$  alongshore, and  $z$  upward. The corresponding velocity components are  $(u,v,w)$ . Table 1 provides a list of symbols found in the model equations, as well as values of constants used throughout the study.

A space-staggered B-scheme (Arakawa and Lamb, 1977) is used for the horizontal finite differencing. This scheme has been shown by Batteen and Han (1981) to be appropriate when the grid spacing is approximately on the same order as, or less than, the Rossby radius of deformation. The horizontal grid spacing is 9 km in the east-west direction and 11 km in the north-south direction, while the internal Rossby radius of deformation is ~30 km.

Consistent with Haney (1974), the vertical spacing scheme of the model concentrates more layers above the thermocline in the dynamically active portion of the ocean. Specifically, the model uses ten vertical layers, with constant z-levels, at depths of 10, 30, 75, 150, 250, 400, 600, 1226, 2283, and 3656 m.

The model domain (Figure 1) encompasses the west coasts of the IP and northwest Africa, from 30° N to 42.5° N (1408 km alongshore), and from 5° W to 17.5° W (1152 km cross-shore). The coastal boundaries of the model domain are closed, and have both the tangential and normal components of velocity set to zero. To highlight the role played by climatological wind forcing, bottom topography has been omitted and the eastern boundary is modeled as a vertical wall. The constant depth used in the model is 4500 m.

A modified version of the radiation boundary conditions of Camerlengo and O'Brien (1980) is used for the open ocean domain boundaries to the north, south, and west. In particular, whether a boundary grid point is treated as an inflow point or an outflow point for a particular prognostic variable is determined by the sign of a dynamically computed effective group velocity. This group velocity is defined as the ratio of the local time derivative and the local space derivative normal to the boundary. If the boundary grid point is thereby determined to be an inflow point, then the value of the prognostic variable is set to its value at the previous timestep. If the boundary point is determined to be an outflow point, its value is set to that of the nearest interior point. Spatial smoothing is also applied with a 1-2-1 weighting window within five grid points (~50 km) of the open boundaries.

Biharmonic lateral heat and momentum diffusion is used in the model with the same choice of coefficients (i.e.,  $2.0 \times 10^{17} \text{ cm}^4/\text{s}$ ) as in Batteen (1997). Holland (1978) showed that highly selective biharmonic diffusion acts predominantly on submesoscales, while Holland and Batteen (1986) found that baroclinic mesoscale processes can be damped by Laplacian lateral heat diffusion. As a result, the use of biharmonic lateral diffusion should allow mesoscale eddy generation via barotropic (horizontal shear) and/or baroclinic (vertical shear) instability mechanisms. As in Batteen (1997), weak ( $0.5 \text{ cm}^2/\text{s}$ ) vertical eddy viscosities and conductivities are used. Bottom stress is parameterized by a simplified quadratic drag law (Weatherly, 1972), as in Batteen (1997).

The method of solution is straightforward with the rigid lid and flat bottom assumptions because the vertically integrated horizontal velocity is subsequently nondivergent. The vertical mean flow can be described by a streamfunction which can be predicted from the vorticity equation, while the vertical shear currents can be predicted after the vertical mean flow is subtracted from the original equations. The other variables, i.e. temperature, salinity, vertical velocity, and pressure, can be explicitly obtained from the thermodynamic energy equation (6), salinity equation (7), continuity equation (3), and hydrostatic equation (4), respectively (For more complete details on the method of solution, see the Appendix).

## **B. TYPE OF WIND FORCING**

Previous experiments by Batteen *et al.* (1992) investigated the role of steady equatorward winds with anticyclonic wind stress curl in the generation of features off the IP. In a more recent study Batteen and Monroe (1998) studied the contributions of seasonal wind forcing and irregular coastline geometry in the generation of eddies and filaments in the California Current system. Following Batteen and Monroe (1998), in this

study, seasonal wind forcing and irregular coastline geometry will be used to investigate the generation of similar features in the CCS.

To explain the effects of seasonal wind, the model is forced from rest with climatological wind fields from a  $2.5^\circ$  by  $2.5^\circ$  grid of the European Centre for Medium Range Weather Forecasts (ECMWF) near-surface wind analyses (Trenberth et al., 1990). The monthly mean stresses based on twice daily wind analyses from 1980-1989 have been interpolated spatially to the 9 by 11 km model resolution and temporally to daily wind values.

Sample wind fields used can be seen in Figure 2, which shows the annual migration of the Azores Subtropical High from the south in the winter (e.g., Figure 2d), to its most northern extent in the summer (e.g., Figure 2b). The atmospheric pressure pattern for November (Figure 2d) depicts a low to the north and the Azores High to the south, which results in a wind divergence at  $\sim 40^\circ$  N. This pattern of weakly poleward winds north of  $40^\circ$  N and equatorward winds to the south continues through December. During January (not shown) and February (Figure 2a) the divergence in the wind field migrates poleward. By March (not shown) an equatorward component in the wind field is observed along the entire domain. The strongest equatorward winds are discernible from July (Figure 2b) through August (not shown). By September (Figure 2c) the winds start to weaken throughout the domain, and divergence in the wind field is observed in the north in October (not shown). In November (Figure 2d) the wind divergence returns to  $\sim 40^\circ$  N.

### **C. EXPERIMENTAL DESIGN**

The design of the model experiment is as follows. The model is forced from rest with seasonal ECMWF winds. The initial mean stratification used are annual climatological temperature fields based on Levitus and Boyer (1994) centered at  $\sim 37.5^\circ$  N (corresponding to the center of the model domain). The temperatures ( $^\circ\text{C}$ ) used for the



ten levels from the surface to 4500 m are 17.5, 17.3, 16.5, 15.0, 13.7, 12.5, 11.0, 8.52, 3.59, and 2.09, respectively, while a salinity constant of 34.7 is used for all levels.

Like all major EBC systems, the CCS is a region of net annual gain. This heat gain occurs because of relatively low cloud cover (compared with farther offshore), reduced latent heat flux, and downward sensible heat flux due to the presence of cold upwelled water during summer. To focus the experiment on wind forcing as a possible mechanism for the generation of thermal variability in the CCS, the surface thermal forcing in the model was highly simplified. The solar radiation at the sea surface  $S_0$ , was specified to be the summer mean and CCS mean value. On the other hand, the sum of the net longwave radiation, latent, and sensible heat fluxes,  $Q_b$ , was computed during the model's experiments from standard bulk formulas (Haney et al. 1978) using the summer and CCS-mean value of the alongshore wind (above), cloud cover, relative humidity, air temperature, and model-predicted sea surface temperature. The initial sea surface temperature was chosen so that the total heat flux across the sea surface,  $S_0 - Q_b$ , was zero at the initial time. Therefore, the only surface heat flux forcing in the experiments was that which developed in  $Q_b$  as a result of (wind forced) fluctuations in the sea surface temperature. As discussed in Haney (1985), such a surface thermal forcing damps the sea surface temperature fluctuations to the atmosphere on a time scale of the order of 100 days. Consequently, sea surface temperature fluctuations that develop due to wind forcing should be observed long before they are damped by the computed surface heat flux.



### III. RESULTS FROM THE MODEL SIMULATION

#### A. SPIN-UP PHASE

On day one of the model (1 January), the Azores High is stationed near its southernmost position. In response to predominantly equatorward winds, a coastal equatorward surface current develops in the southern end of the domain and by day 60 extends along the entire coast (not shown).

In the spring as the Azores High migrates north, the wind intensifies and transitions to equatorward flow over the entire domain. As a result, increased stress is exerted on the ocean surface creating Ekman transport offshore and upwelling of cooler water along the coast. Upwelling predominantly occurs in the south where stronger winds exist (e.g., Figure 3a), but by mid-summer is evident along the entire coast (e.g., Figures 3b and 4). Upwelling is enhanced near capes (e.g., Figure 3b), where both the alongshore component of the wind stress and the coastal current velocity are at local maxima (Batteen, 1997).

Below the equatorward surface current, a poleward undercurrent develops first at the equatorward side and then at the poleward side of the model domain. The coastal jet extends from ~200 m depth near the coast to ~600-800 m depth offshore, and has a peak core velocity of ~30-45 cm/s (Figures 5a and 5b). Along the west coast of the IP (e.g., Figure 5a) and Morocco (not shown) the undercurrent develops separate cores at ~400 m depth and 1200 m depth. The ~400 m depth core of the undercurrent has a peak velocity of ~5-10 cm/s and remains within ~20-30 km of the coast. The ~1200 m depth core of the undercurrent has a peak velocity of ~5-10 cm/s and generally remains within ~40-50 km of the coast.

In the Gulf of Cadiz there is no separation of the undercurrent cores. The core of the undercurrent is found between  $\sim 400$  and  $1200$  m depth and has speeds of  $5$  cm/s (Figure 5b).

As the coastal jet and the subsurface undercurrent become fully established (for example, see Figures 5a and 5b, which shows the structure of the currents prior to meander formation), strong vertical and horizontal shears develop in the upper layers between the opposing currents. This shear causes the flow to become both barotropically and baroclinically unstable and leads to the formation of meanders and filaments. Meanders occur first off Cape Ghir, Cabo da Roca and Cabo de Sao Vincent. These meanders intensify and develop into predominantly cyclonic cold core eddies, which in time coalesce with other eddies to form larger cyclonic eddies on the order of  $\sim 150$ - $250$  km. By day 285 (Figure 3c) meanders and eddies are visible throughout the coastal region.

In the late fall as the Azores High migrates south, first the winds and then the currents begin to weaken. In time, upwelling, as expected, also weakens. By the end of the first year of model simulation (Figure 3d), the equatorward surface flow extends as far as  $\sim 350$  km offshore and has taken the form of a meandering jet embedded with predominantly cyclonic eddies.

## **B. QUASI-EQUILIBRIUM PHASE**

Continuous formation and sustainment of meanders, eddies and filaments indicate that the model has reached a quasi-equilibrium state by year three. Time-averaging model output fields for each month as well as the peak upwelling season (July through September) in year three provides an opportunity to see the complex structure and seasonal variability of the CCS.

The winter model results (e.g., Figure 6a) depict a predominantly equatorward flow, which is embedded with eddies throughout the domain. Along the IP, a surface

coastal poleward flow with speeds as high as  $\sim 22.5$  cm/s is visible (Figures 6a and 7a). Beneath the surface (Figure 7a), cores of poleward flow with speeds of  $\sim 10$ - $17.5$  cm/s at  $\sim 600$  and  $\sim 1200$  m depth are discernible. An additional third core of poleward flow at  $\sim 250$  m depth with a speed of  $\sim 10$  cm/s is also formed along the IP in the vicinity of  $\sim 39^\circ$  N (Figure 7a).

By early spring an equatorward coastal jet appears off the coast of Morocco south of  $32^\circ$  N and upwelling resumes (not shown). By June (Figure 6b) upwelling appears all along the IP and a strong equatorward current with speeds of  $\sim 25$ - $40$  cm/s meanders along the IP. Off Cabo da Roca the equatorward current weakens as it flows into the Gulf of Cadiz. South of  $35^\circ$  N the equatorward current becomes a coastal jet with speeds of  $\sim 40$  cm/s. Downstream of Cabo da Roca (Figure 6b) and Cape Beddouzza (not shown) pairs of cyclonic (Figures 6b and 7b) and anticyclonic (Figures 6b and 7c) eddies of  $O(150)$  km in size and extending to greater than 1400 m depth are discernible.

In the summer (Figure 6c) upwelling is visible along the western and southern coast of the IP as well as along the coast of Morocco. As the equatorward jet flows along the IP, it impinges upon Cabo da Roca and is deflected offshore advecting cold water with it, resulting in the formation of filaments (e.g., Figure 6c) off Cabo da Roca and Cabo de Sao Vincent. Filaments are also discernible off Cabo de Santa Maria and the southern coast of Portugal (Figure 6d). The filaments typically extend from  $\sim 75$  to 150 m depth (not shown). Beneath the surface (Figure 7d), cores of poleward flow with speeds of  $\sim 5$ - $7.5$  cm/s at  $\sim 600$  and  $\sim 1200$  m depth are evident. An additional weaker core of poleward flow at  $\sim 250$  m depth with a speed of  $\sim 5$  cm/s is also formed off the west coast of the IP in the vicinity of  $37^\circ$  N.

The results (Figure 8) of averaging the temperature and current fields for the period when the most intense upwelling (i.e., July through September) occurs off both the IP and Morocco shows that a meandering equatorward current offshore, an equatorward coastal jet, subsurface poleward flow with cores at  $\sim 600$  m depth and  $\sim 1200$  m depth, coastal upwelling, filaments and eddies are regular features of the CCS during the

upwelling season. Figure 8a shows the surface equatorward current offshore of the  $\sim 17.5^\circ$  C isotherm until south of Cabo da Roca where the  $16.5^\circ$  C and  $17.5^\circ$  C isotherms separate. South of Cabo de Sao Vincent the offshore equatorward current once again splits into two distinct flows. The westernmost flow continues equatorward while the easternmost flow meanders cyclonically and joins the coastal jet in the Gulf of Cadiz. Off Cape Beddouzza the offshore flow and coastal current rejoin, and continue down the coast of Morocco. The offshore current has speeds of  $\sim 15$ - $45$  cm/s and extends to  $\sim 1000$  m depth (Figures 8b and 8c). The coastal jet has peak speeds of  $\sim 45$  cm/s and extends to  $\sim 250$  m depth near the coast (Figure 8c). Upwelling is visible all along the IP coast as well as along the coast of Morocco (Figure 8a). Cold, upwelled filaments are also discernible downstream of prominent capes (Figure 8a). The filaments typically extend  $\sim 125$  km offshore, have widths of  $\sim 75$  km and extend to  $\sim 100$  m depth (not shown). Figure 8b shows the often fused  $\sim 250$  m depth and  $600$  m depth undercurrent cores found between Cabo da Roca and Cabo de Sao Vincent as well as the  $\sim 1200$  m depth undercurrent core. The  $\sim 250$  m and  $600$  m depth cores reach speeds of  $\sim 10$  cm/s while the  $1200$  m depth core reaches speeds of  $\sim 2.5$ - $5$  cm/s. Figure 8d shows the  $\sim 1200$  m depth undercurrent as it flows along the entire coast from Morocco into the Gulf of Cadiz and along the IP during the peak upwelling season. Offshore of the undercurrent are both cyclonic and anticyclonic eddies of  $O(150)$  km in size that extend to at least  $1000$  m depth (Figures 8d and 8e).

Figures 9a and 9b show horizontal maps of upper layer mean kinetic energy (MKE) and eddy kinetic energy (EKE) averaged during the peak upwelling season. Holland *et al.* (1983) showed that maps of MKE and EKE can be used to locate sources of mean and eddy energy. From Figure 9a it can be seen that high values of MKE follow the equatorward jet and that the highest values of MKE appear near areas of tightened temperature gradients off Cabo da Roca, in the Gulf of Cadiz and off Cape Beddouzza.

A comparison of Figures 8a and 9b shows maximum values of EKE in the vicinity of the large cyclonic meander that extends downstream from Cabo da Roca. High values

are also formed along the axes of the equatorward jet on the west coast of the Gulf of Cadiz and offshore of Cape Ghir and Cape Beddouzza. The lowest coastal values of EKE are along the southern coast of the IP, indicating that this region is not a primary source of eddy energy.

A comparison of Figures 8a, 9a and 9b shows that overall, the regions of maximum MKE and EKE are found along the axes of the equatorward jet. This is consistent with the results of the model simulation, which showed that the eddies are generated from instabilities of the mean equatorward current and subsurface undercurrent via baroclinic and/or barotropic instability processes.

By Fall (e.g., Figure 6e) upwelling has weakened and the coastal jet is no longer visible north of Cabo da Roca. Offshore, a meandering equatorward current embedded with westward propagating, cyclonic eddies is discernible. Farther south, the coastal jet leaves the coast at Cape Beddouzza and is entrained in a large cyclonic eddy  $O(200 \text{ km})$  prior to continuing south along the coast of Morocco. By winter, poleward surface flow with speeds of  $\sim 15\text{-}25 \text{ cm/s}$  has developed north of  $41^\circ \text{ N}$ . The flow is found within  $\sim 60 \text{ km}$  of the coast and extends to  $\sim 200 \text{ m}$  depth (Figure 7e).

### **C. COMPARISONS OF MODEL RESULTS WITH OBSERVATIONS**

To ensure model results are consistent with realistic features of the CCS, the model results are compared to available field and satellite observations. Since this is an idealized process-oriented study and not a model hindcast, direct comparisons are not valid; however, it can be shown that the model's phenomenological behavior is qualitatively similar to observed data. The discussion in the ensuing paragraphs first details general CCS features and then specific magnitudes and characteristics of features generated along the western coasts of the IP and Northwest Africa. Overall, there exists impressive similarities between the results of the model simulation and the major characteristics of the CCS.

## **1. Comparison of Ocean Currents**

The major characteristics of the modeled Canary Current off western Iberia and northwestern Africa are consistent with the few field observations and studies available. Satellite imagery also reveals a system of meanders, eddies, and along-shelf jets, on a range of length scales that correspond closely with model output.

### ***a. Equatorward Flow***

Using climatological wind data and a realistic coastline, the model develops an ocean current with features similar to those observed in the CCS. The broad, equatorward flow found throughout the model domain matches the general description of classical EBCs by Wooster and Reid (1963). The sustained magnitude of the model's equatorward flow also compares favorably with available data. For example, DMAH/TC (1988) shows a mean predominantly equatorward flow of ~0.5 to 0.7 kts (~25-35 cm/s), which is consistent with velocities found in the model simulation (e.g., Figures 8a and 8c).

### ***b. Poleward Flow***

The model establishes a poleward undercurrent with cores at ~600 m depth and ~1200 m depth throughout the domain (Figures 5a, 7a, 8b, and 8c). In addition, a third core of poleward flow at ~250 m depth is seen near 37° N along the west coast of the IP predominantly during June, July and August (e.g., Figure 7d) and near 39° N during November and January (e.g., Figure 7a). The depths and magnitudes of the 600 m and 1200 m depth model's poleward flow cores are consistent with Ambar (1980), which shows these cores located between 600-900 m and 1100-1200 m depth along the entire western coast of the IP. The depth and speed of the 250 m model's poleward flow is consistent with Haynes and Barton (1990), which shows this core located between 100 and 600 m depth off the IP.



Recent studies by Frouin *et al.* (1990) and Haynes and Barton (1990), using high resolution infra-red images from NOAA7 and NOAA9 and numerous in-situ measurements, reveal the existence of surface poleward flow off the northern coast of Portugal and northwestern Spain. These studies show a current ~25-40 km wide, that extends to ~200 m depth and reaches speeds of ~20-25 cm/s. Similarly, in response to the shift in the climatological winds from northerly to southwesterly late in the year (see Figure 2), the model generates surface poleward flow in the northern end of the domain. As seen in Figures 6a, 7a and 7e surface poleward flow with speeds of 15-25 cm/s develops within 60 km of the coast and to a depth of ~200 m.

## **2. Comparison of Eddies**

High resolution satellite imagery and observations by Fiuza (1984) show pairs of mesoscale eddies on the order of 100 km off the west coast of the IP (Figure 10). This study confirms the model's generation of numerous eddies on the order of 100 km in the CCS.

Preferred locations of instability onset (eddy generation) occur where the coastline significantly changes, i.e., near Cabo da Roca, Cabo de Sao Vincent, the Gulf of Cadiz, and Cape Beddouzza/Cape Ghir. A comparison of the results of Fiuza (1984) (Figure 10), with the results of the model simulation (e.g., Figures 3c, 3d, 6 and 11) shows that the model generates eddies in similar locations.

## **3. Comparison of Upwelling**

Upwelling varies by season throughout the domain as a result of the seasonally oscillating winds seen in Figure 2. Observations show that upwelling appears first off Cape Ghir/Cape Beddouzza in early spring as seen in Van Camp *et al.* (1991), and then progressively to the north as the Azores High moves up the Moroccan coast. This progression of upwelling is well simulated in the model (e.g., Figures 11a and 11b). Observed upwelling off Portugal from ~43° N to Cabo de Sao Vincent in the south

(Figure 12a) and along the southern coast of Portugal to Cabo de Santa Maria,  $\sim 8^\circ$  W (Folkard et al., 1997) is also well depicted by the model (e.g., Figure 11c). Observations of peak upwelling during July, August and September are shown in Figures 12b and 12c while Figures 8a, 11d and 11e show the model depicting the most intense upwelling during this period as well.

#### **4. Comparison of Filaments**

Several studies by Fiuza (1983), Barton (1986), Fiuza and Sousa (1989), Folkard et al., (1997), Van Camp et al. (1991) and Hagen et al. (1996) have confirmed the existence of cold filaments extending off the west coasts of the IP and Morocco depicted by the model.

##### ***a. West Coast of Iberia***

Fiuza (1983) was the first study to indicate the existence of filaments off the west coast of the IP. Subsequent studies by Fiuza and Sousa (1989) using CTD data and satellite imagery confirmed the existence of filaments including a large filament off Cabo de Roca. In addition, recent SST observations show several good images of filaments occurring along the entire west coast of the IP (e.g., Figure 12b) with a particularly long filament at  $40.5^\circ$  N. The model depicts filaments in many of the same locations as well (Figures 11d, 11e, 11f and 11g). A filament exists near  $\sim 41^\circ$  N (Figures 11d and 11e) while a rather strong filament is also evident at  $\sim 39^\circ$  N (Figures 11d, 11f and 11g) and downstream of Cabo da Roca (Figures 11d and 11e).

##### ***b. South Coast of Iberia/Gulf of Cadiz***

While investigating the waters of southern Iberia in the Gulf of Cadiz, Folkard et al. (1997) observed cold, upwelled filaments extending southward from the

coast. The model results shown in Figures 6d, 6e, 11f and 11g depict these filaments as well.

*c. Cape Ghir/Northwest Africa*

Satellite observations from Van Camp *et al.* (1991) and Hagen *et al.* (1996) show a filament of cold, upwelled water extending off Cape Ghir near 31° N for about 200 km. Consistent with these observations, the model depicts this filament as an equatorward meandering coastal jet which transports cold, upwelled water offshore (Figure 11e). Observations show that the coastal jet and subsequent frontal zone caused by the advected cold water results in the generation near ~12° W of a cyclonic eddy-like feature on the southern side of the jet, while an anticyclonic eddy forms on the northern side. The model results (Figure 11e) show that, consistent with the observations, on the northern side of the jet is an anticyclonic eddy centered at ~12° W, 33° N and on the southern side of the jet a cyclonic eddy at ~12° W, 31.5° N.

In summary, the variety of length scales and life time scales, in conjunction with the differences in field observations themselves, emphasize the complex flow region of the CCS. Despite this complexity, the numerical model results show striking similarities to available field observations of surface and subsurface currents, upwelling, filaments, meanders, and cyclonic and anticyclonic eddies.



#### IV. SUMMARY

The objective of this study was to investigate the role of seasonal climatological wind forcing in the generation of currents, eddies, jets, and filaments in the CCS. Toward this end, a high resolution, multi-level, PE model using a realistic coastline was forced from rest using spatially and temporally varying winds. The cyclic migration of the Azores High, and the subsequent role it has on the seasonal variability of alongshore winds, was shown to play a significant role in the generation, evolution and sustainment of mesoscale features in the CCS.

An equatorward surface current and a subsurface poleward current with cores at ~600 m and 1200 m depth developed and were maintained throughout the year. A third core of poleward flow was also generated at ~250 m depth at ~37° N from June through August and at ~39° N during January and November. Along the northern IP, surface poleward flow developed in the late fall and lasted until late spring. The opposing nature of the equatorward and subsurface poleward currents resulted in both horizontal (barotropic instability) and vertical (baroclinic instability) shear. This shear caused the currents to become unstable, meander, and eventually lead to the formation of cyclonic and anticyclonic eddies. As meanders intensified along the coast, cold, upwelled water was advected offshore forming filaments.

Model results also depicted a seasonal upwelling cycle tied to the migrating Azores High. Upwelling began in the spring along the southern coast of Morocco, progressed northward, and by mid-summer was visible along the coast throughout the domain. During the upwelling season a surface equatorward coastal jet overlying the poleward undercurrent was generated. As the coastal jet reached its maximum velocity during the peak upwelling season (July through September), eddy formation along the coast increased. Seasonal filament generation also occurred during and just after the upwelling season.

Coastline irregularities also appeared to play a significant role in the formation of mesoscale features. Specifically, the capes acted as barriers that forced the coastal equatorward flow offshore. This continuous offshore deflection caused some meanders and eddies to appear as quasi-permanent rather than seasonal features. Capes were also areas of enhanced upwelling and were significant in the location and formation of filaments.

A comparison of the currents, eddies, jets, and filaments generated by the model with available observations showed that the model successfully simulated the location, size, and velocity of these features. Of the features generated, the poleward undercurrent and its cores are of particular interest. Until now, it has generally been accepted, that these cores were the result of Mediterranean Outflow influence (e.g., Ambar, 1980). This study showed, however, that the cores could be generated by wind forcing alone.

Future modeling efforts to enhance the simulation and resolution of CCS features should include the addition of thermohaline gradients, bottom topography and MO. Observations have shown that, depending on prevailing wind direction, an inflow or outflow through the Strait of Gibraltar can exist, which can affect the flow in the Gulf of Cadiz (e.g., Folkard et al., 1997). Opening the Strait of Gibraltar into the Mediterranean Sea would also allow the study of density-driven undercurrent components. With the addition of bottom topography, the topographical steering of MO and anchoring of coastal features could be studied.

Using ECMWF winds of relatively coarse spatial resolution, this study focused on the role of seasonal winds in the CCS. It would be of interest to investigate this role using winds of higher spatial and temporal resolution. The use of winds with spatial resolution down to  $\sim 1$  km and temporal resolution of  $\sim 1$  day would allow the oceanic response to wind events, relaxations, and reversals to be studied.

The lack of readily available data along the Moroccan and IP coasts was a concern to this study. Although several studies discuss briefly the surface temperature, salinity, and density patterns off the IP, and northwest Africa and for the Cape Ghir Filament, little

discussion is available about the basics. Few observations concerning the velocity and structure of equatorward flow exist. Fewer still are observations of surface poleward flow along the IP and subsurface observations of filaments, meanders and eddies. In short, this area remains a prime candidate for a refreshing update of the generalization given the Canary Current by Wooster and Reid (1963).

Nevertheless, the results from this experiment show surprising similarities to the large-scale observational data available in the area studied. The results also support the hypothesis that wind forcing and coastal irregularities play a key role in the generation, evolution, and sustainment of the currents, meanders, eddies, and filaments of the CCS.





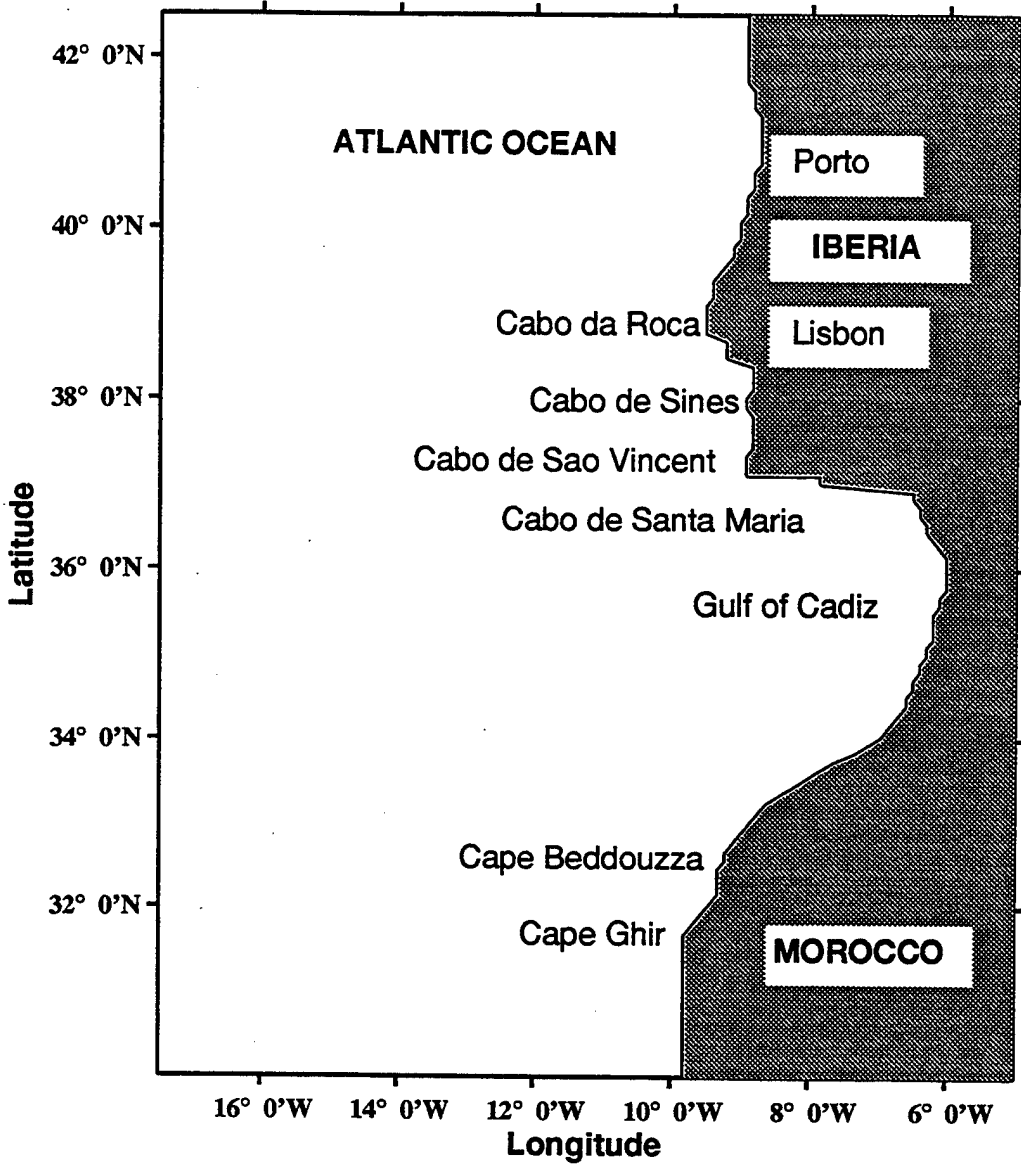
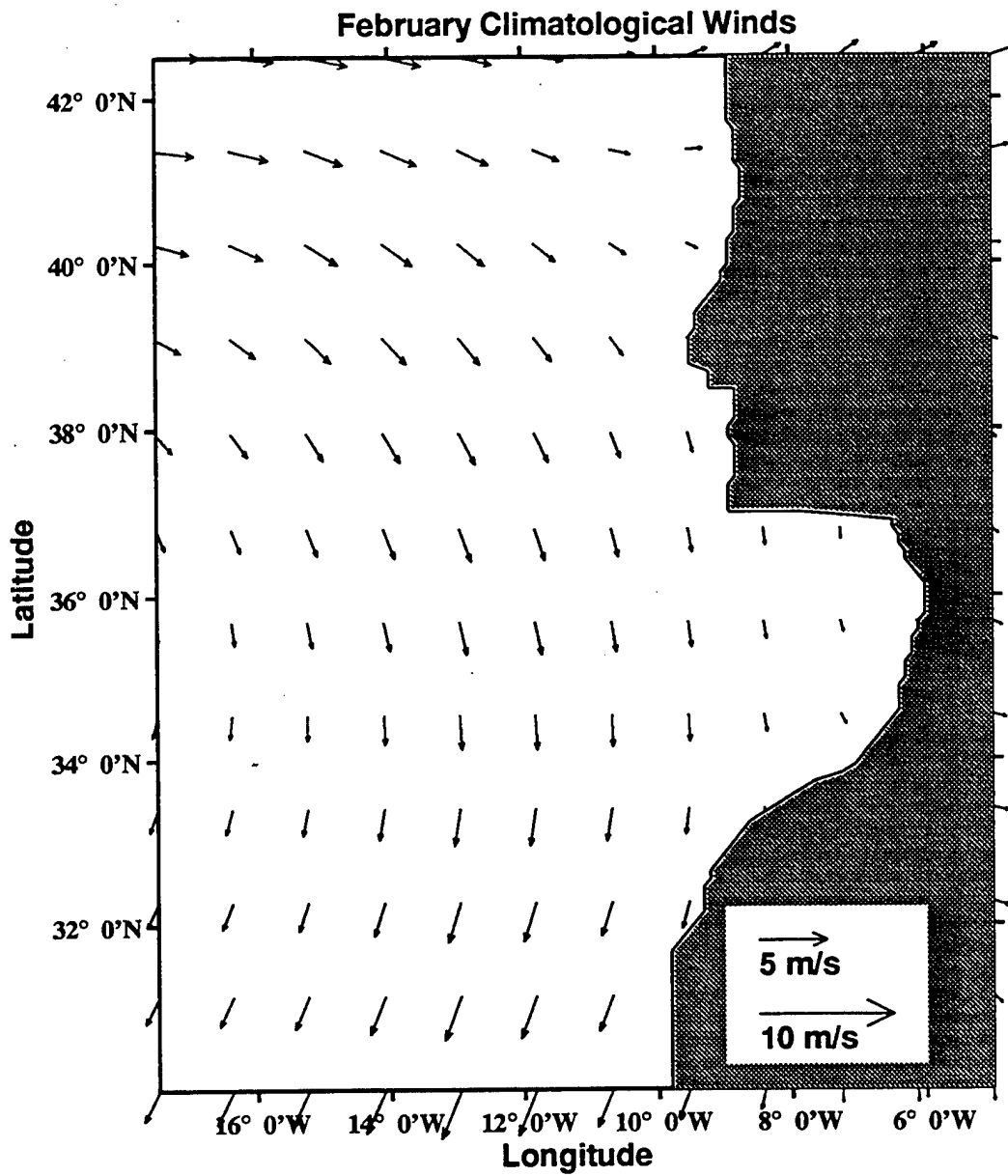


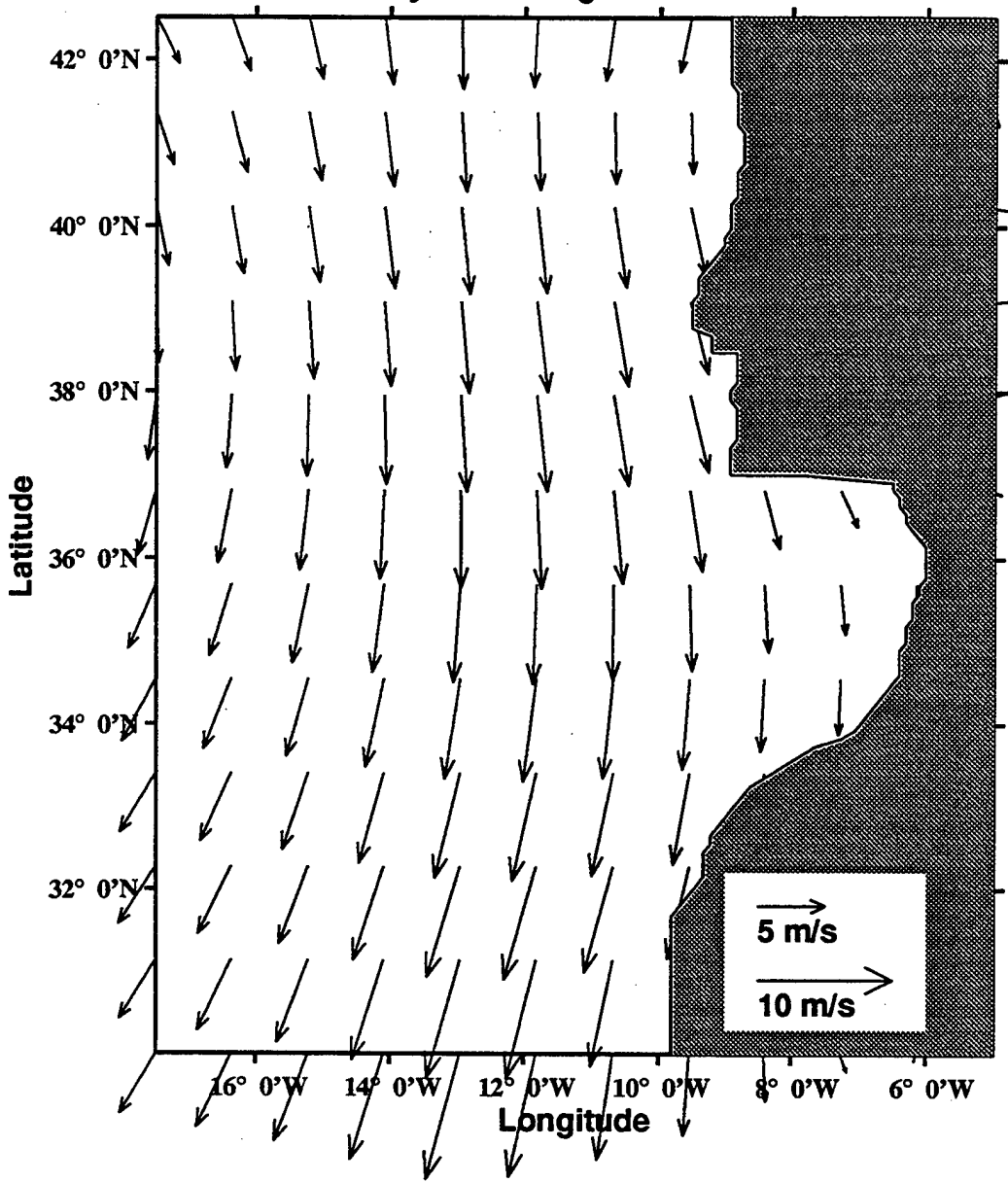
Figure 1. The model domain for the Canary Current System (CCS) is bounded by 30° N to 42.5° N, 5° W to 17.5° W. The cross-shore (alongshore) resolution is 9 km (11 km). Geographic locations and prominent features are labeled.



a.

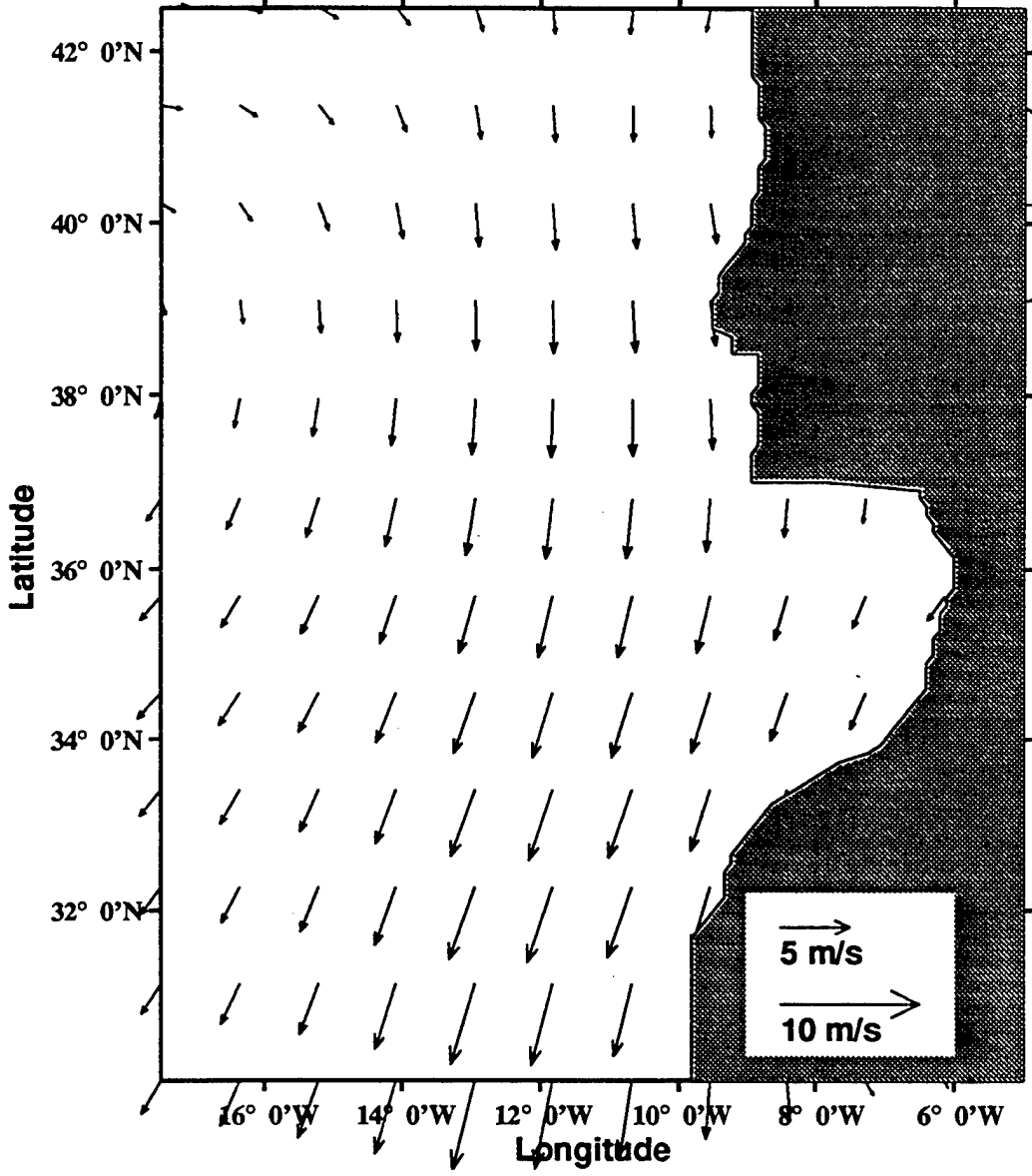
Figure 2. Climatological (1980-1989) ECMWF winds in m/s for: (a) February, (b) July, (c) September, and (d) November. Maximum wind vector is 10 m/s.

### July Climatological Winds

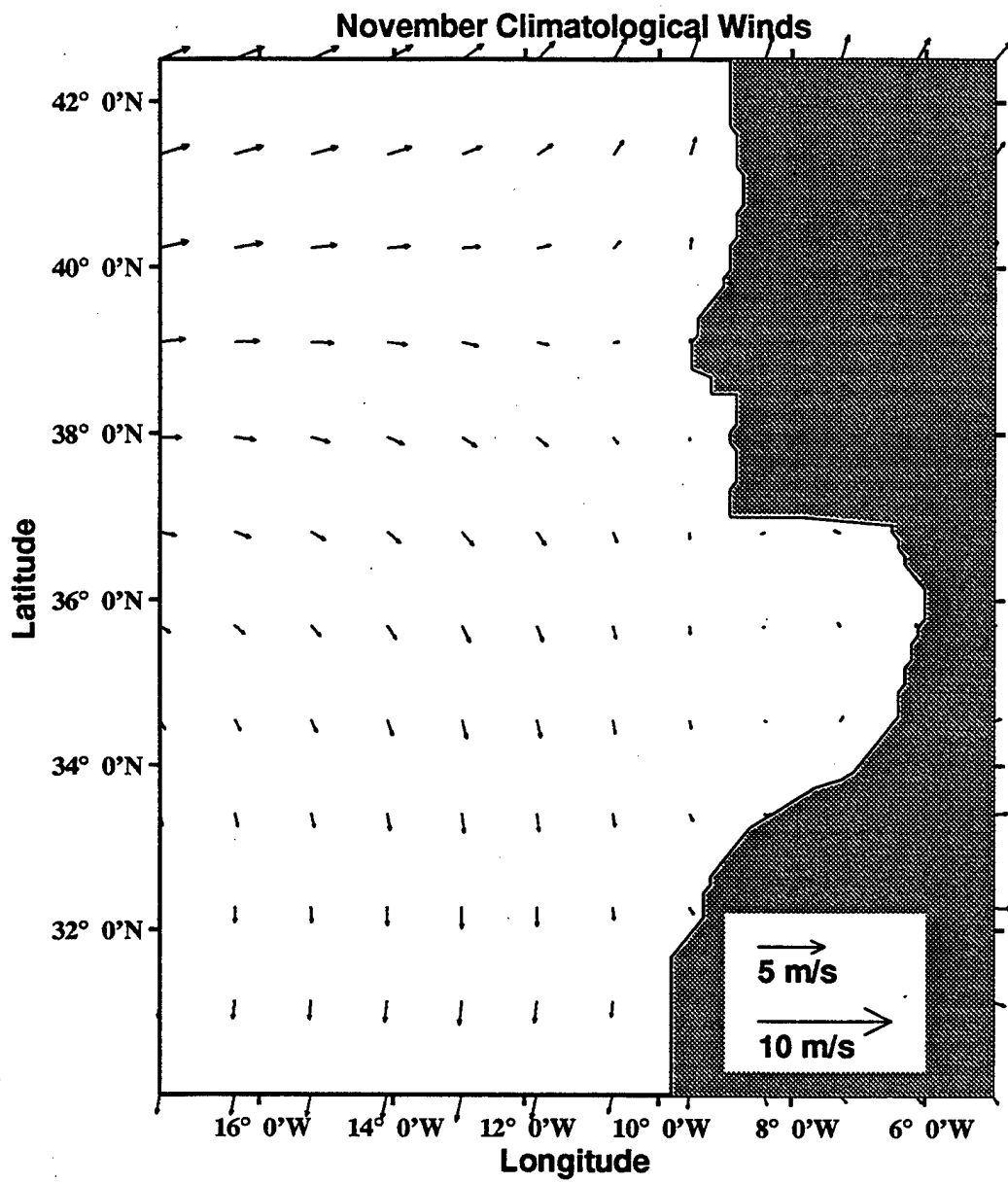


b.

### September Climatological Winds



c.



d.

DEPTH : 30m  
T : 150

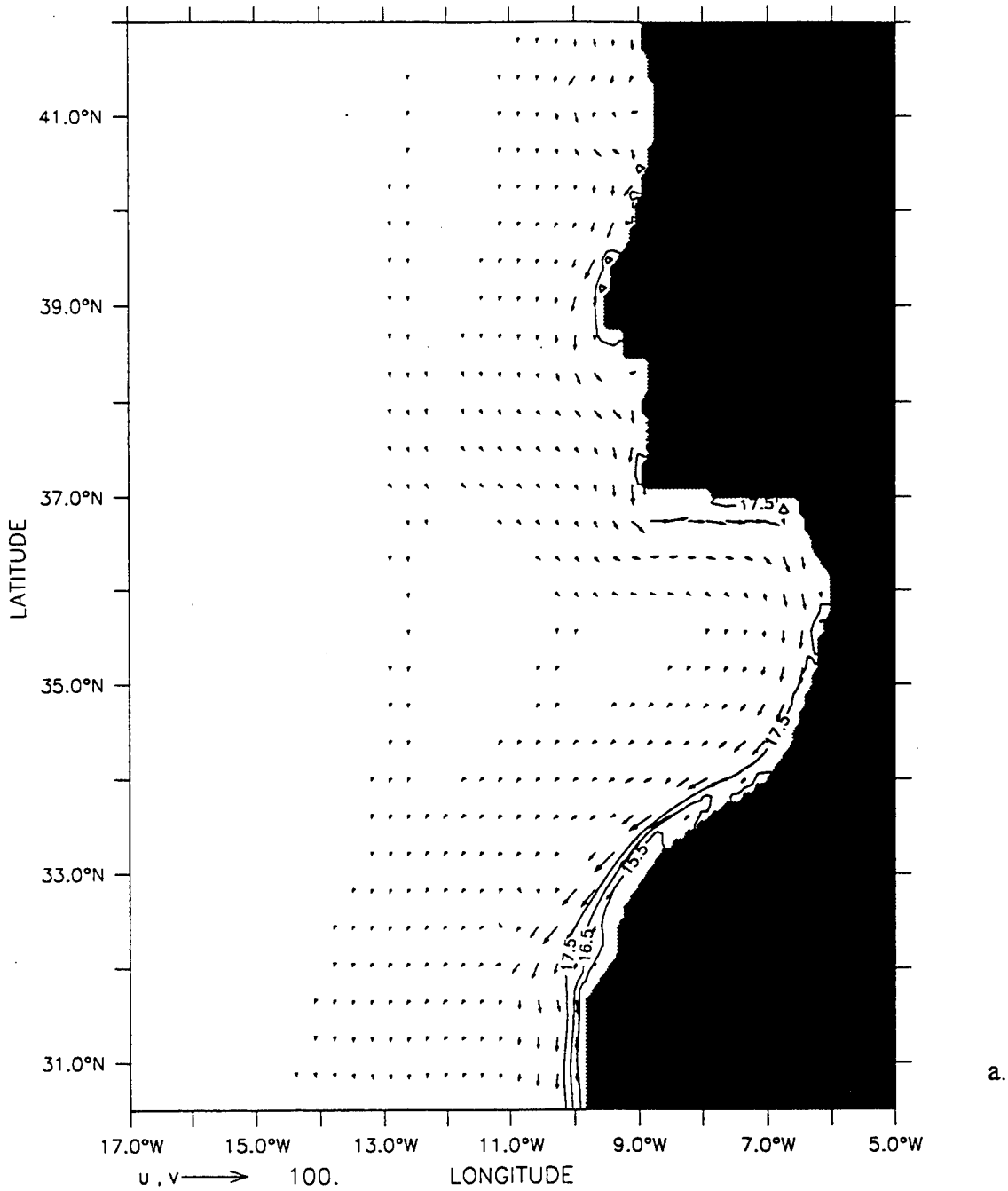
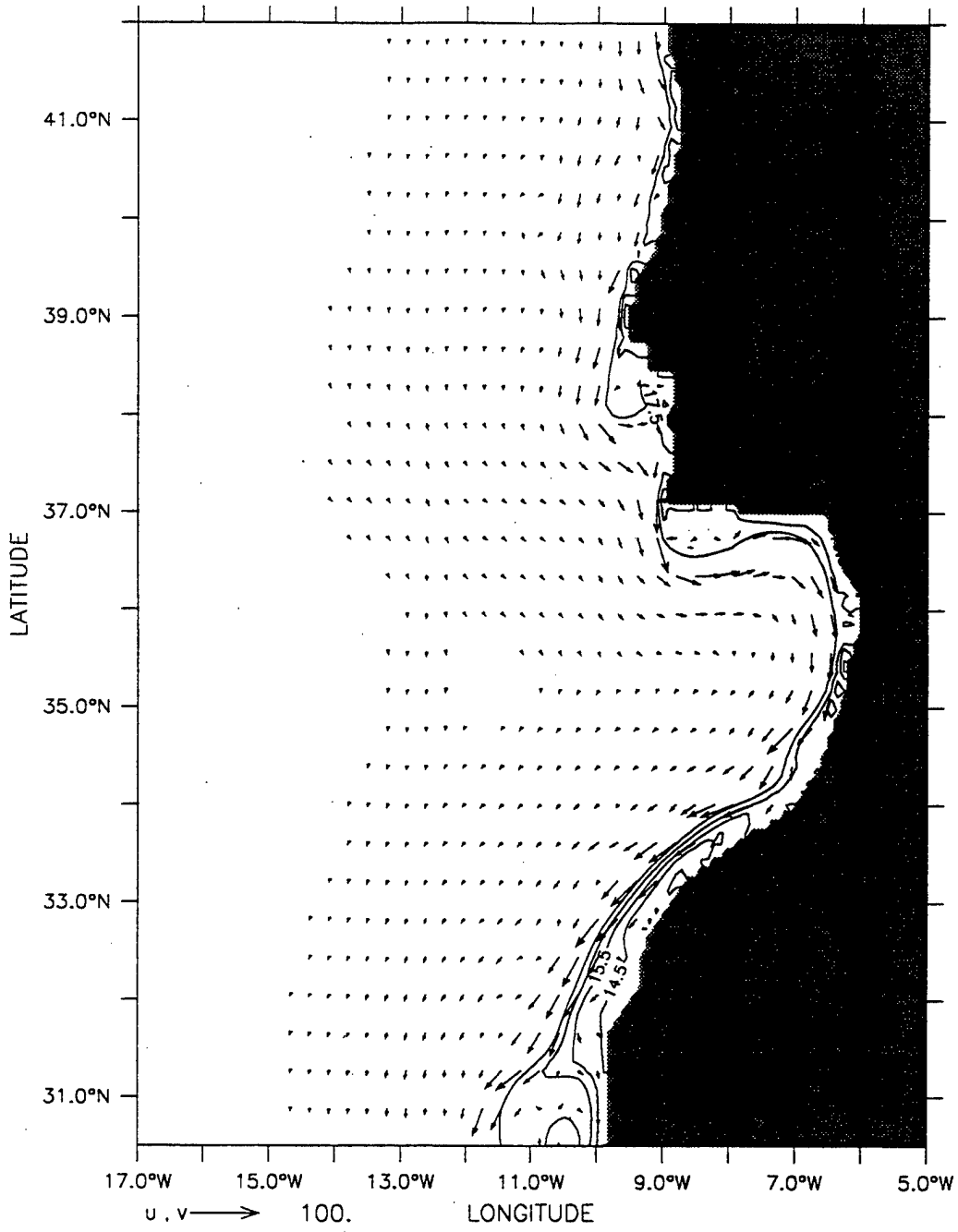


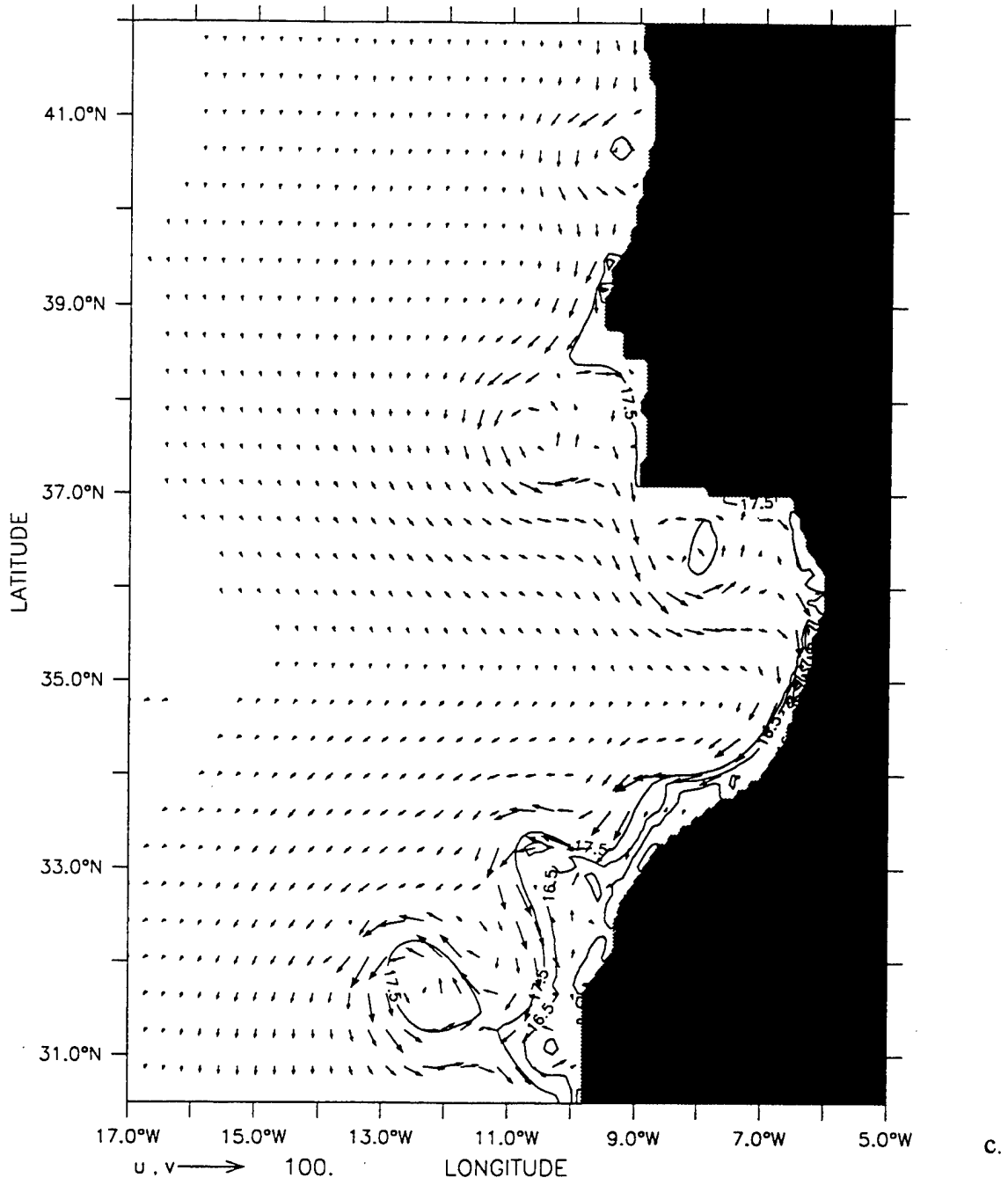
Figure 3. Temperature contours and velocity vectors at 30 m depth at days (a) 150, (b) 195, (c) 285 and (d) 360. The contour interval is 1°C. To avoid clutter, the velocity vectors are plotted every third grid point in the cross-shore direction and every fourth grid point in the along-shore direction. Maximum current velocity is 100 cm/s.

DEPTH : 30m  
T : 195



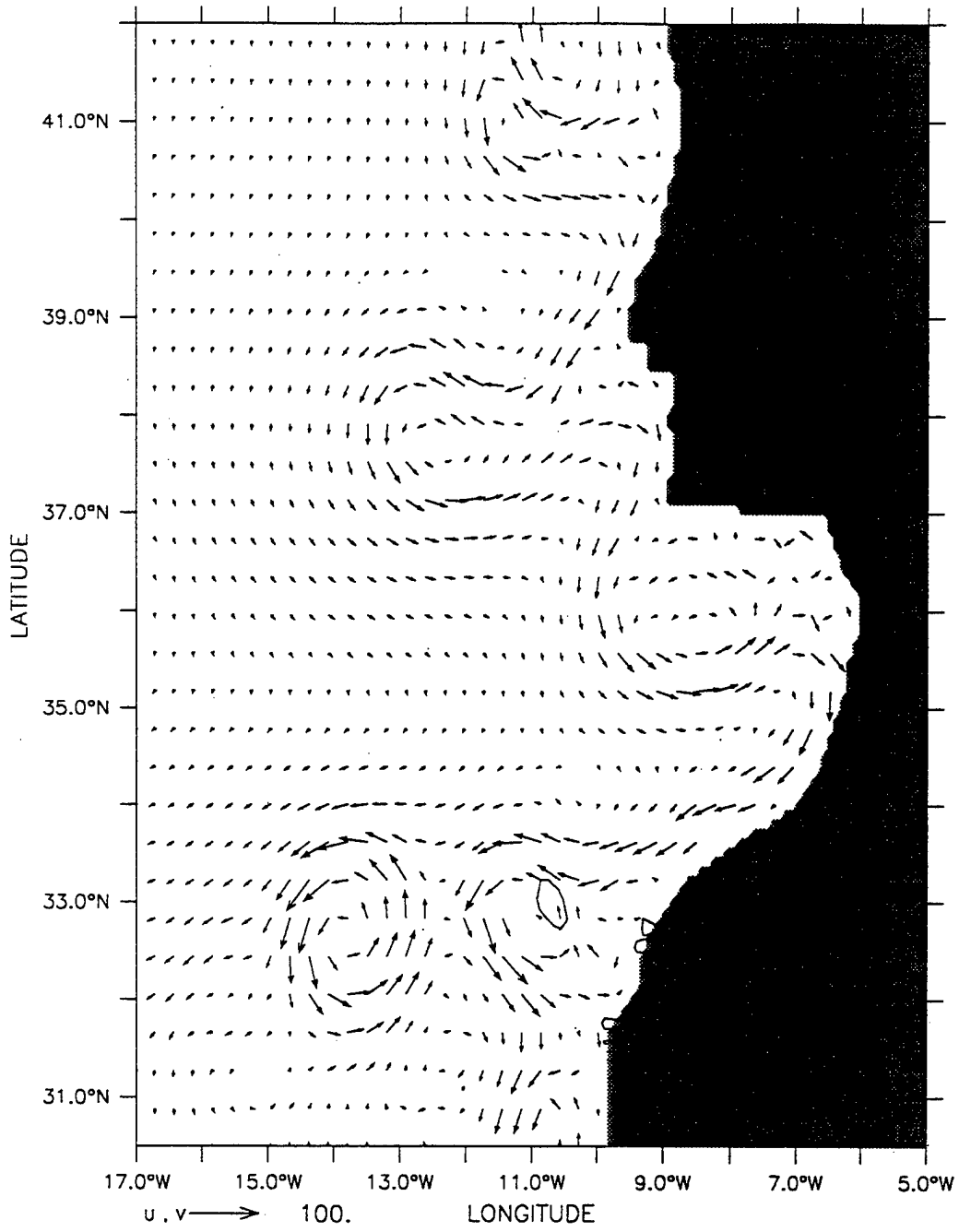
b.

DEPTH : 30m  
T : 285

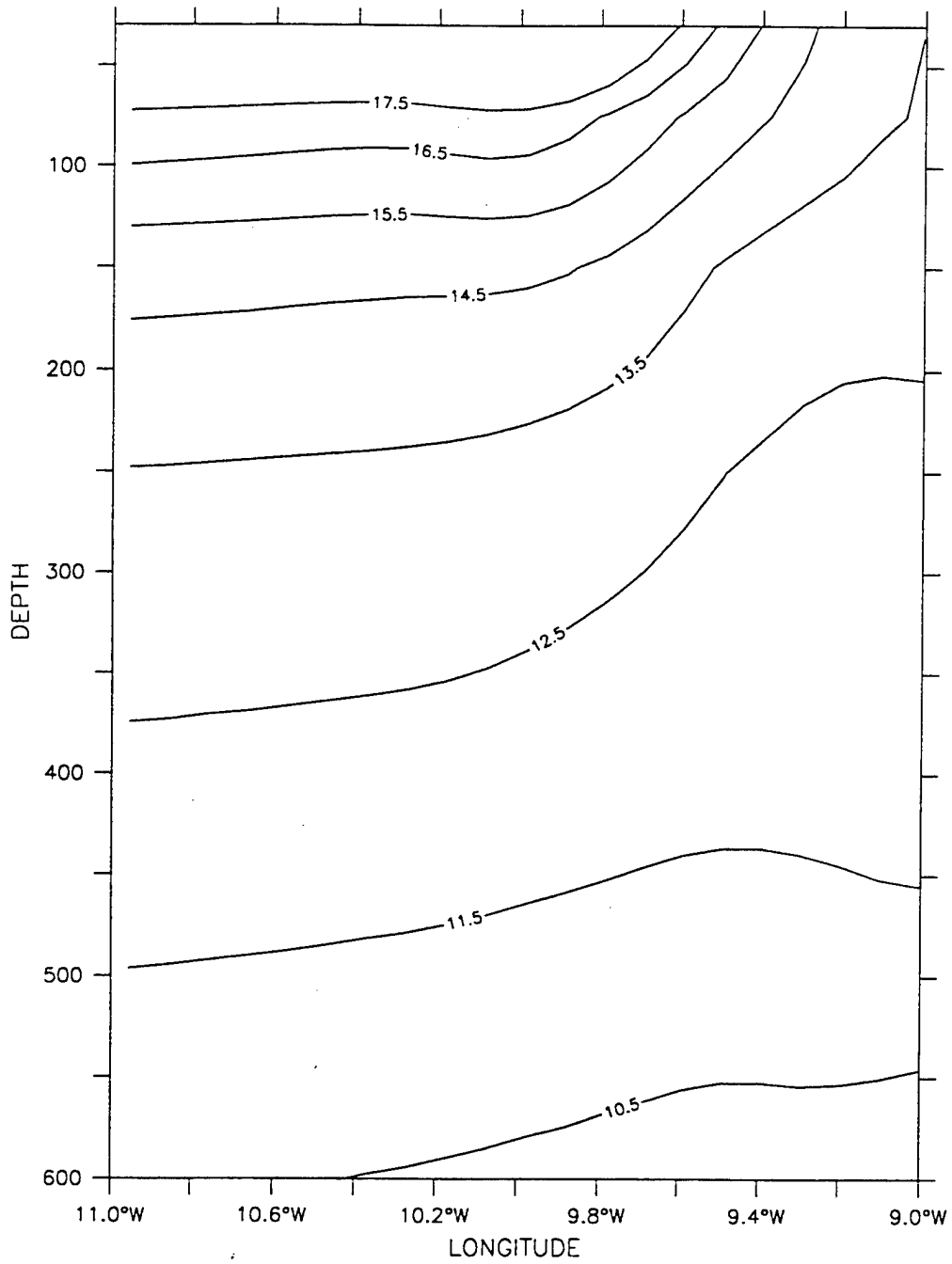




DEPTH : 30m  
T : 360



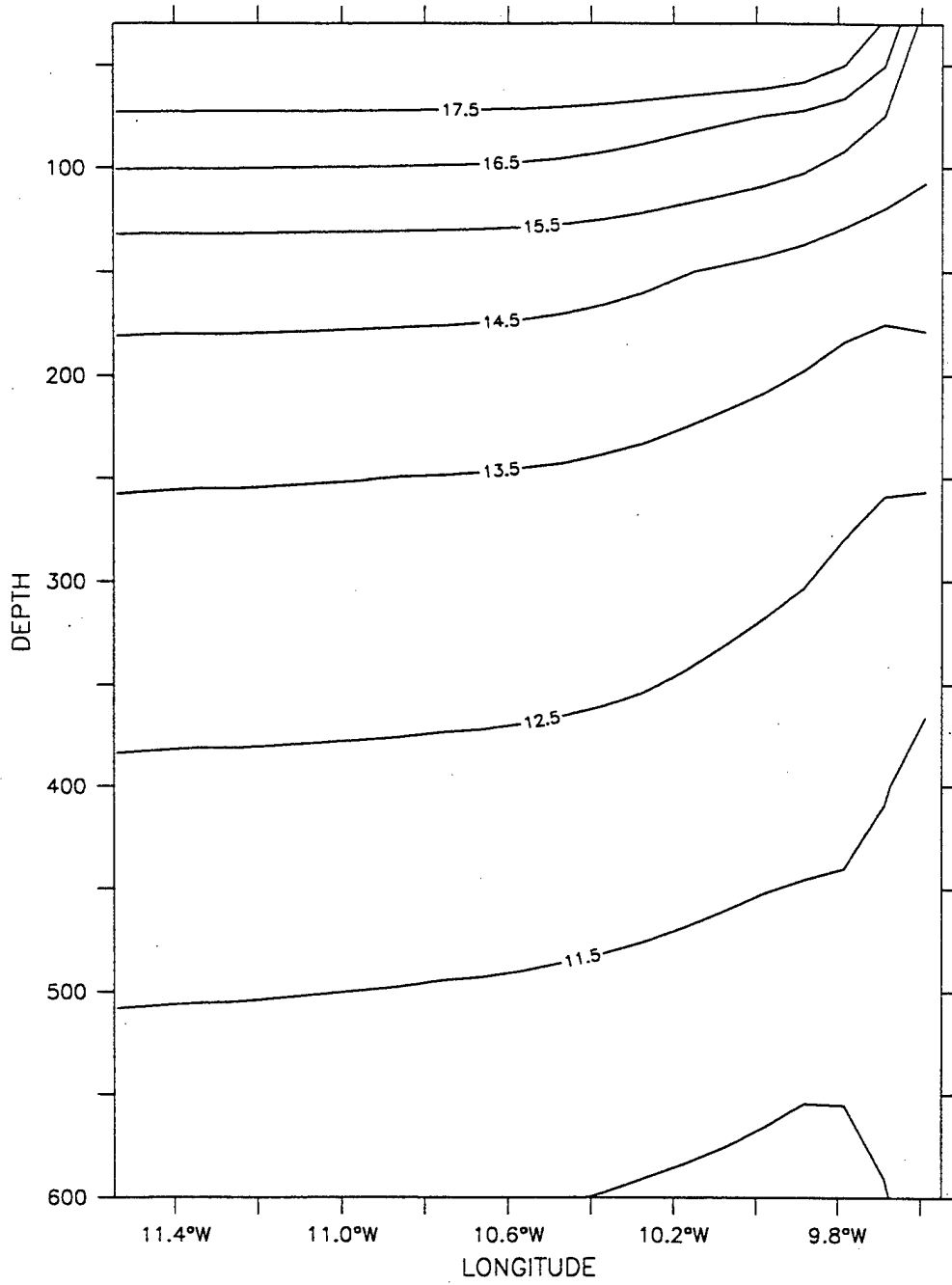
LATITUDE : 33N  
T : 195



a.

Figure 4. Cross-shore sections of isotherms on day 195 at (a) 33° N and (b) 39° N. Contour interval is 1° C.

LATITUDE : 39N  
T : 195



b.

LATITUDE : 39.5N  
T : 240

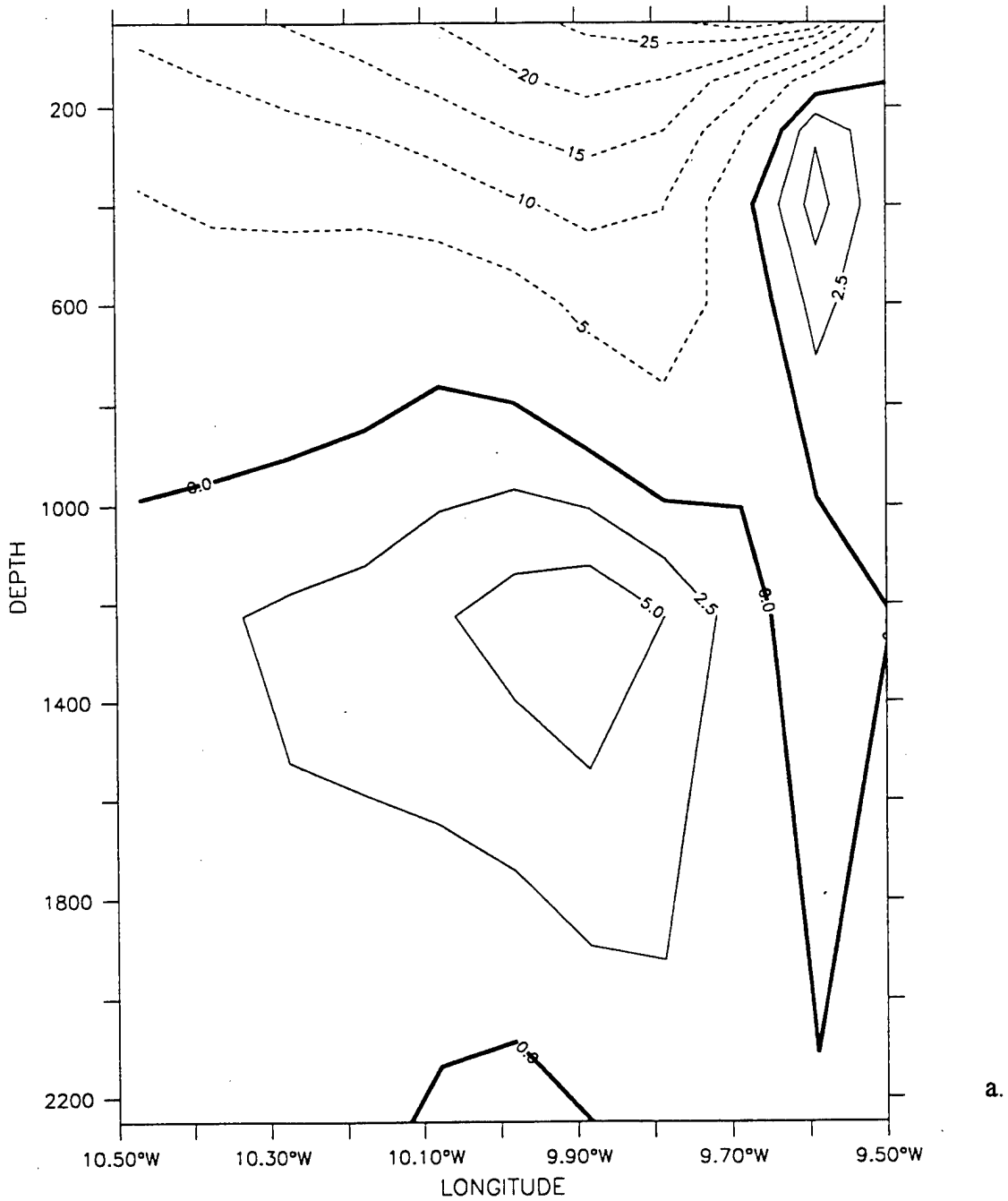
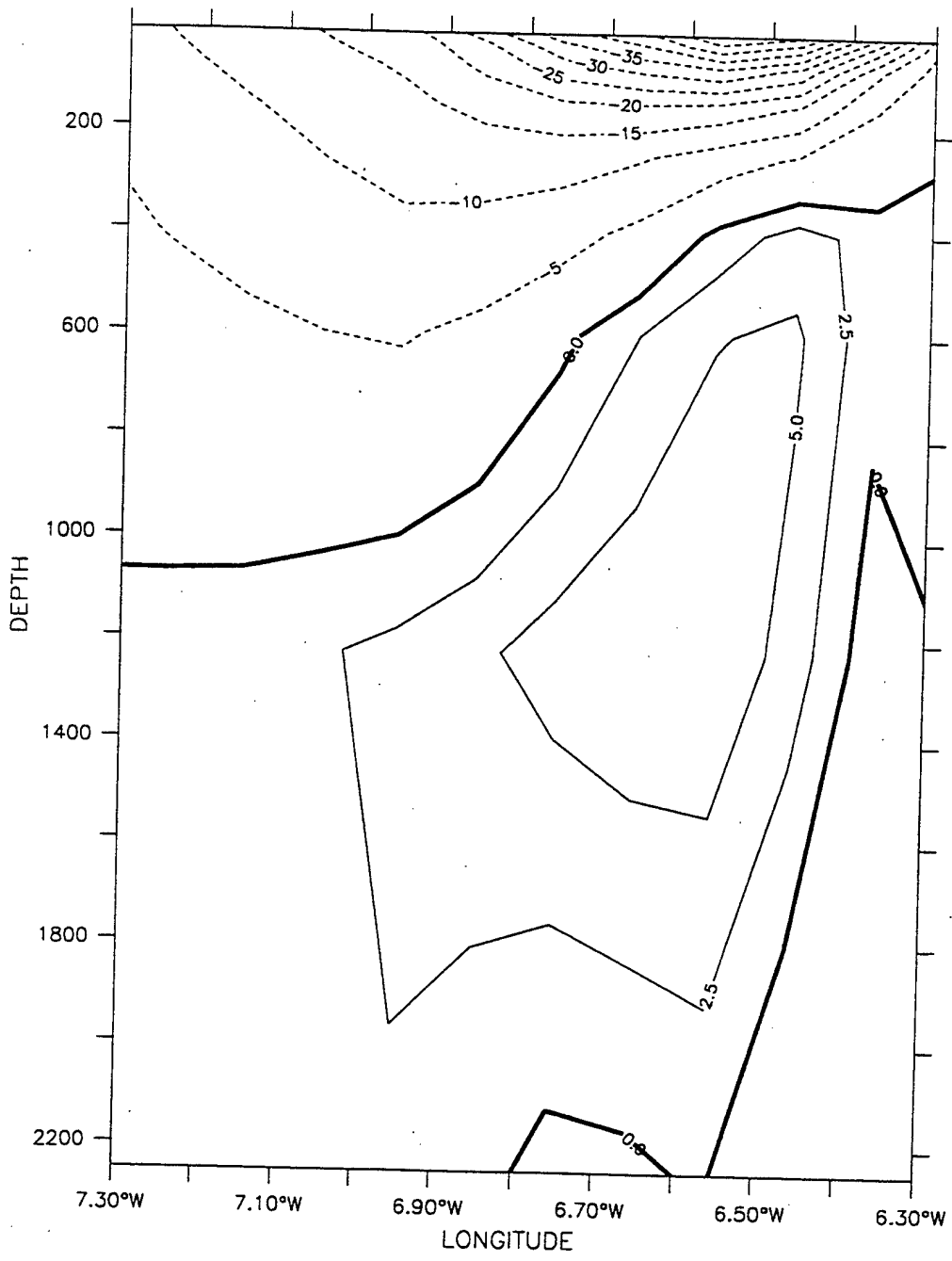


Figure 5. Cross-shore sections of meridional velocity ( $v$ ) on day 240 at (a)  $39.5^\circ\text{N}$ , and (b)  $35.5^\circ\text{N}$ . Solid lines indicate poleward flow, while dashed lines indicate equatorward flow. The contour interval is  $2.5\text{ cm/s}$  for poleward flow and  $5\text{ cm/s}$  for equatorward flow.

LATITUDE : 35.5N  
T : 240



b.

DEPTH : 30m

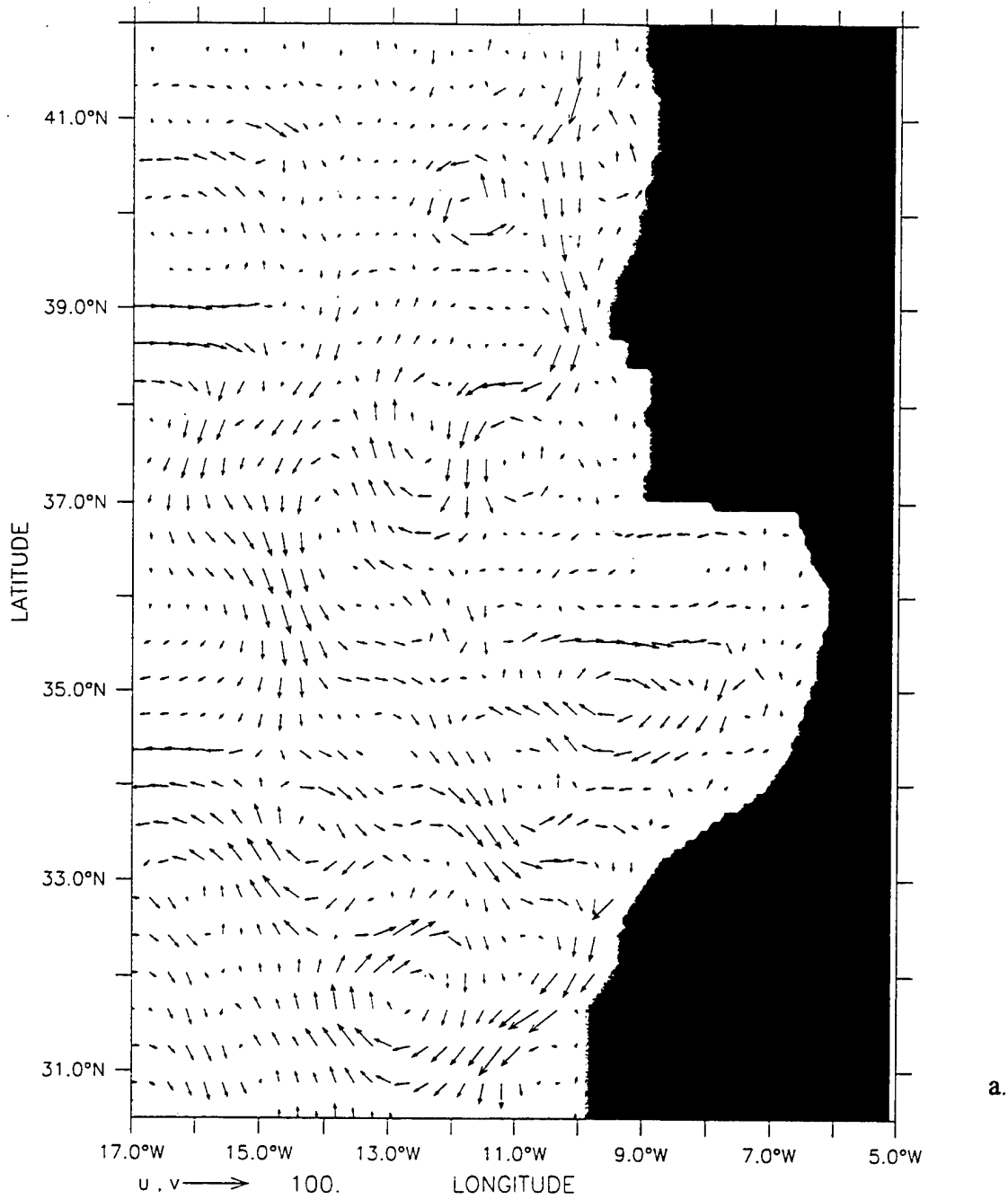
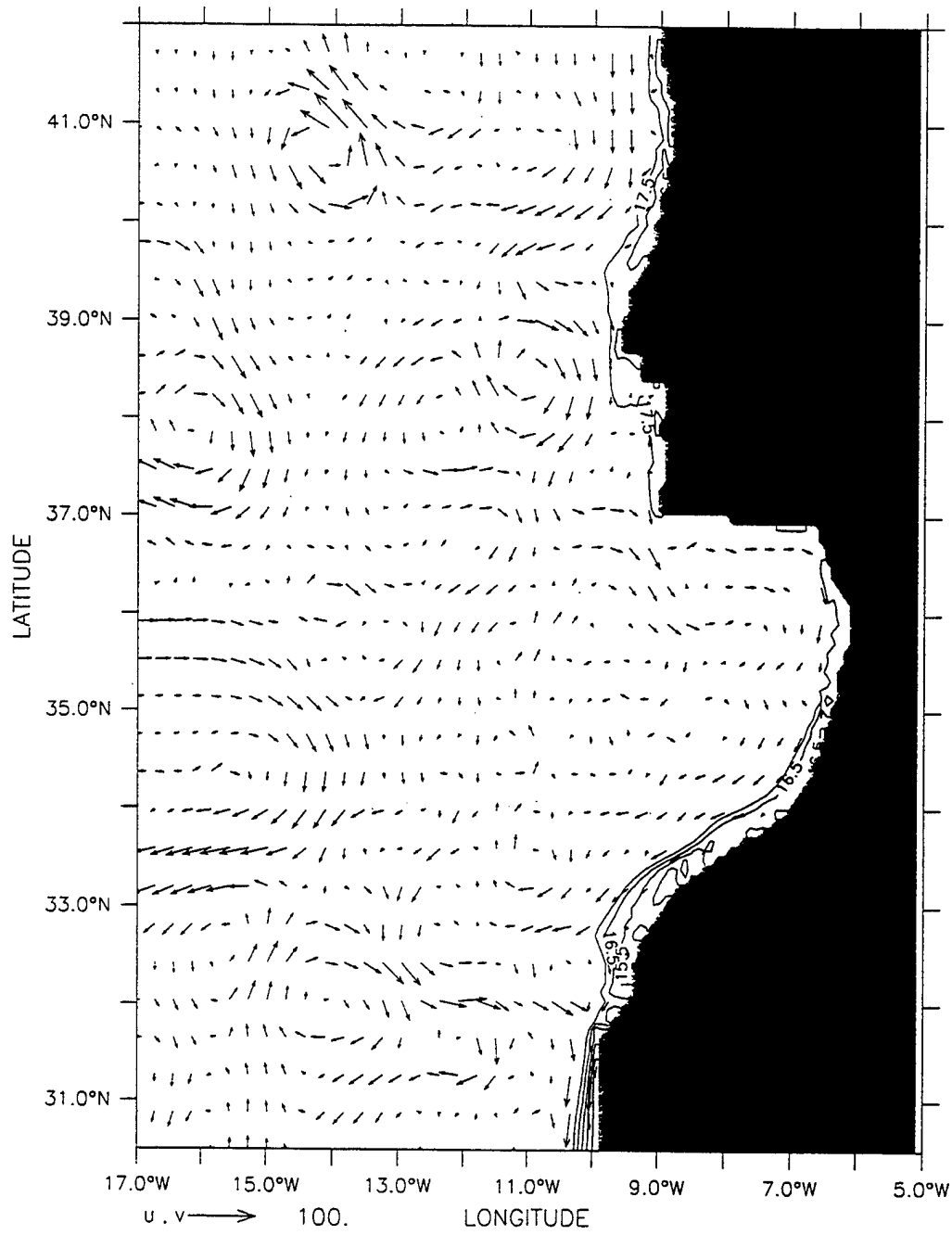


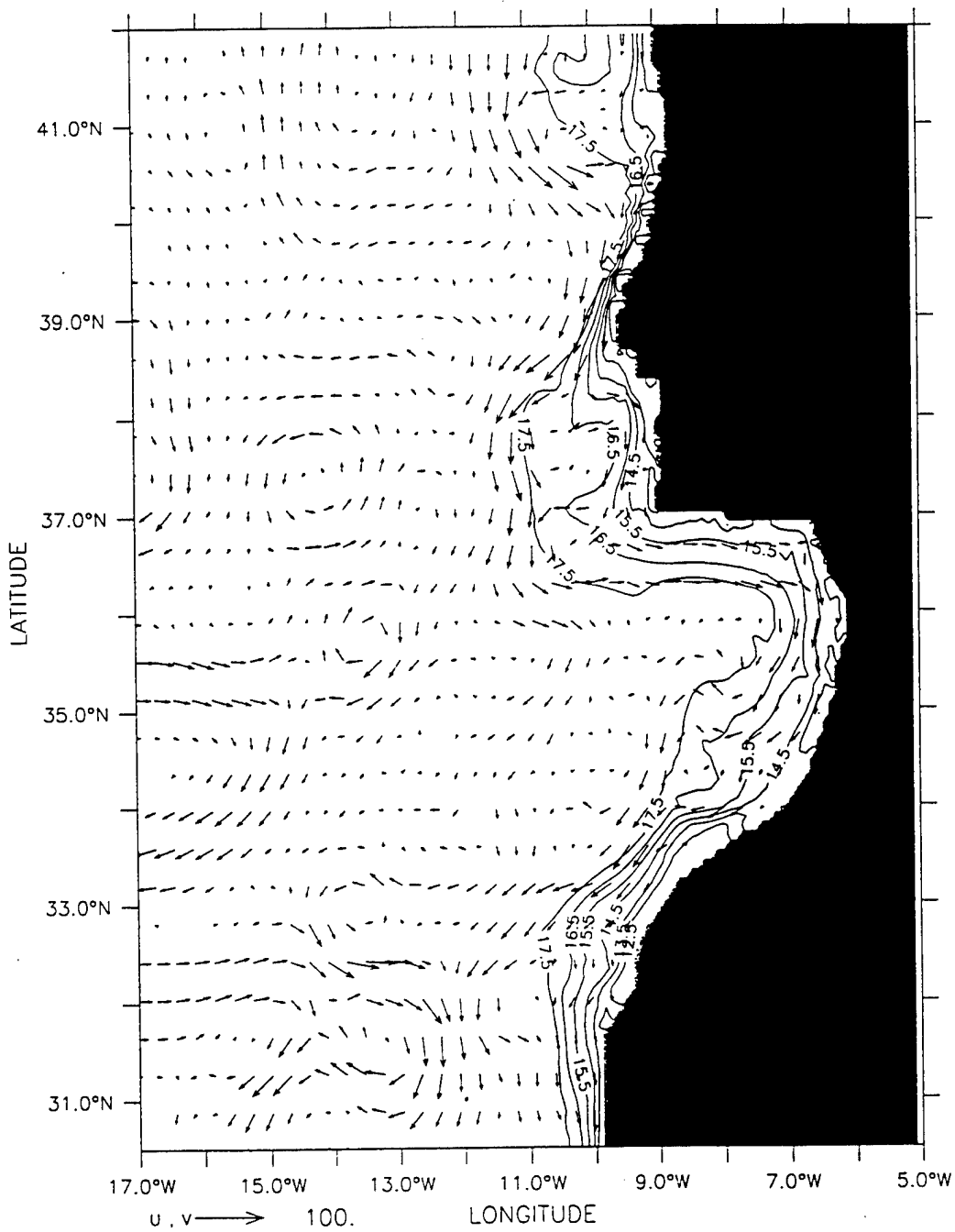
Figure 6. Temperature contours (b-e) and velocity vectors (a-e) at 30 m depth in the third year of the model simulation time-averaged over the months of (a) January, (b) June, (c) August, (d) September and (e) November. The contour interval is 1° C. Maximum current velocity is 100 cm/s.

DEPTH : 30m



b.

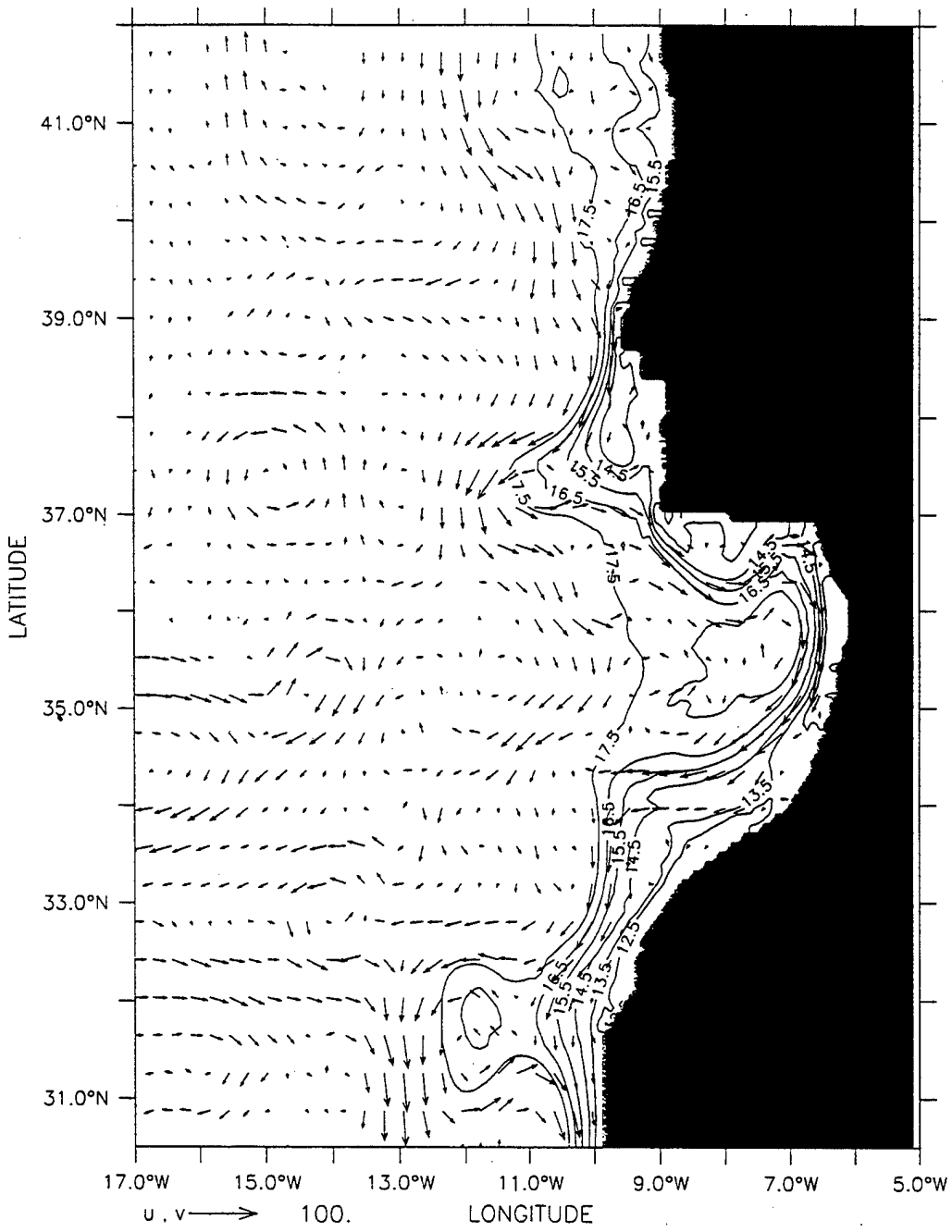
DEPTH : 30m



c.

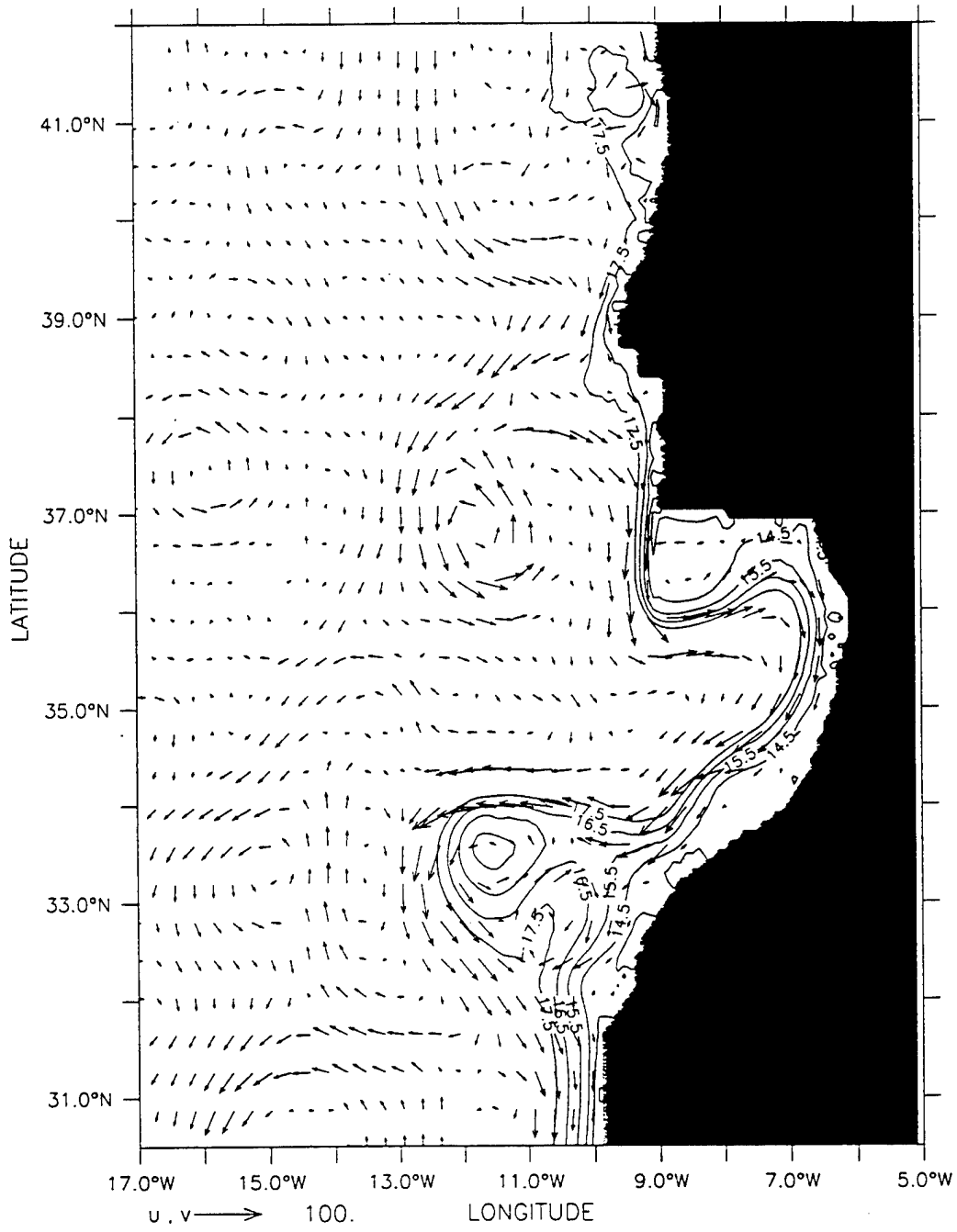


DEPTH : 30m



d.

DEPTH : 30m



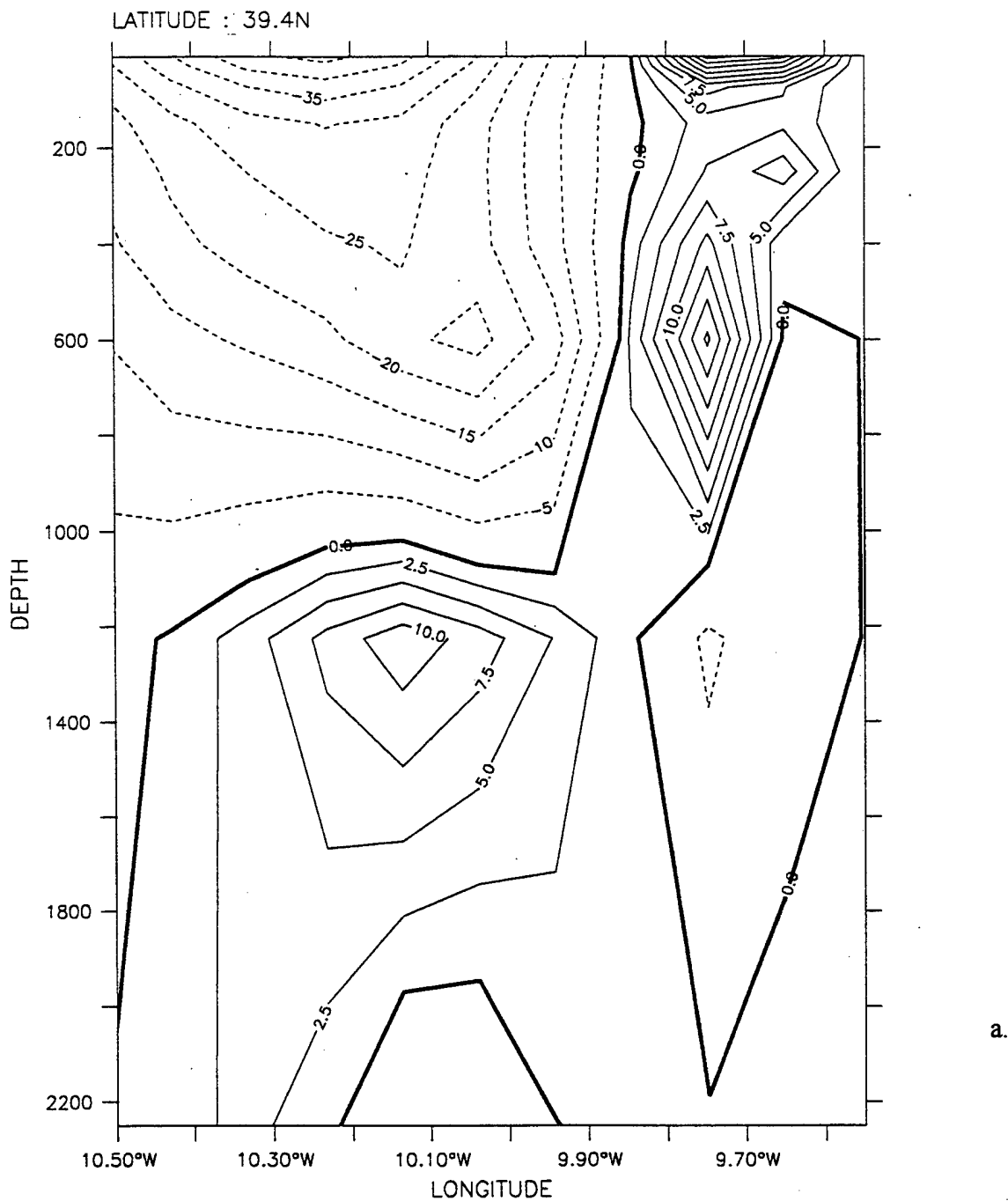
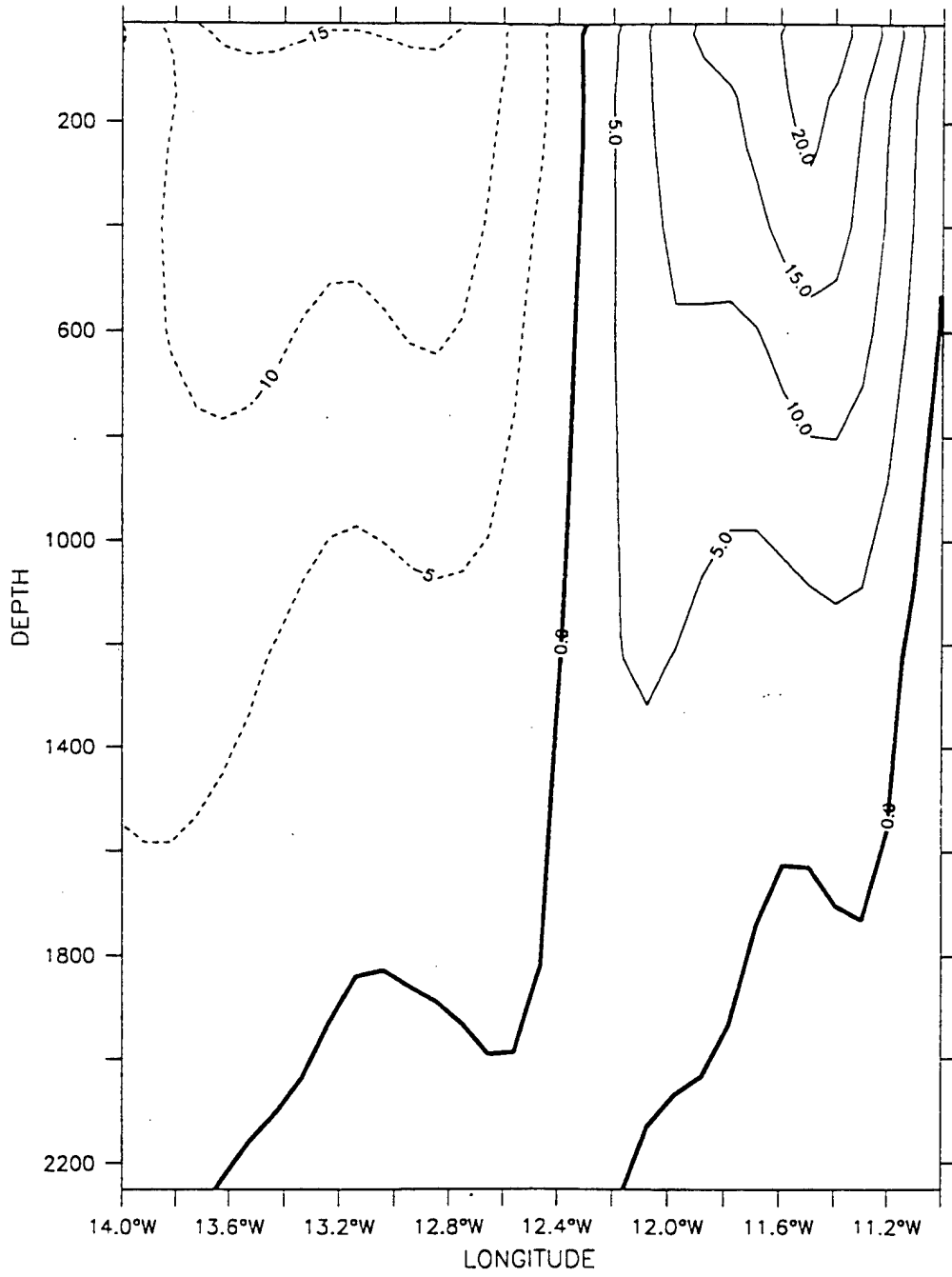


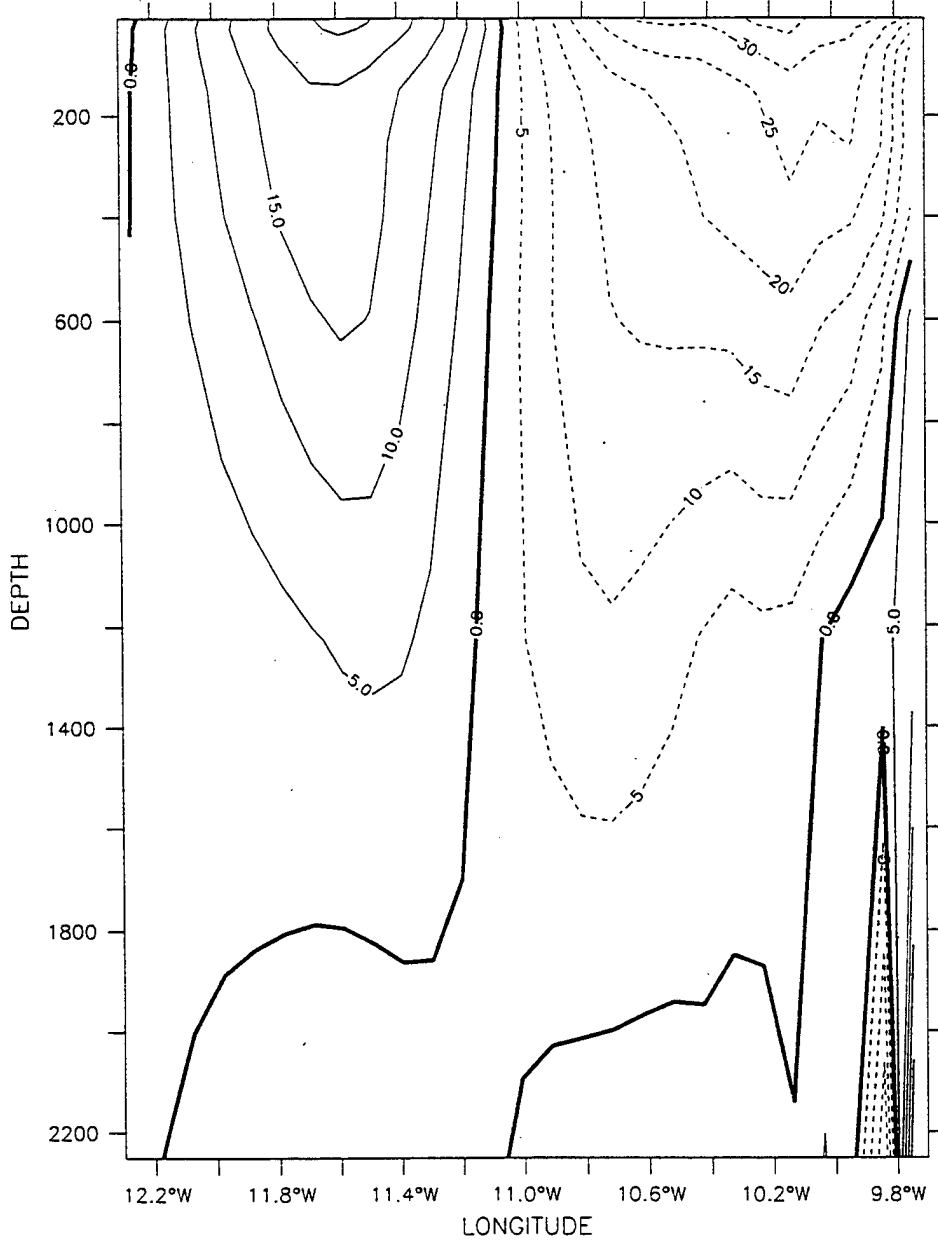
Figure 7. Cross-shore sections of meridional velocity ( $v$ ) in the third year of model simulation time-averaged for (a) January at  $39.4^\circ$  N, (b) June at  $38^\circ$  N and (c)  $38.6^\circ$  N, (d) August at  $37.5^\circ$  N and (e) December at  $41.5^\circ$  N. Solid lines indicate poleward flow, while dashed lines indicate equatorward flow. The contour interval is 2.5 cm/s for poleward flow in (a), (d) and (e), 5.0 cm/s for poleward flow in (b) and (c), and 5 cm/s for equatorward flow.

LATITUDE : 38N



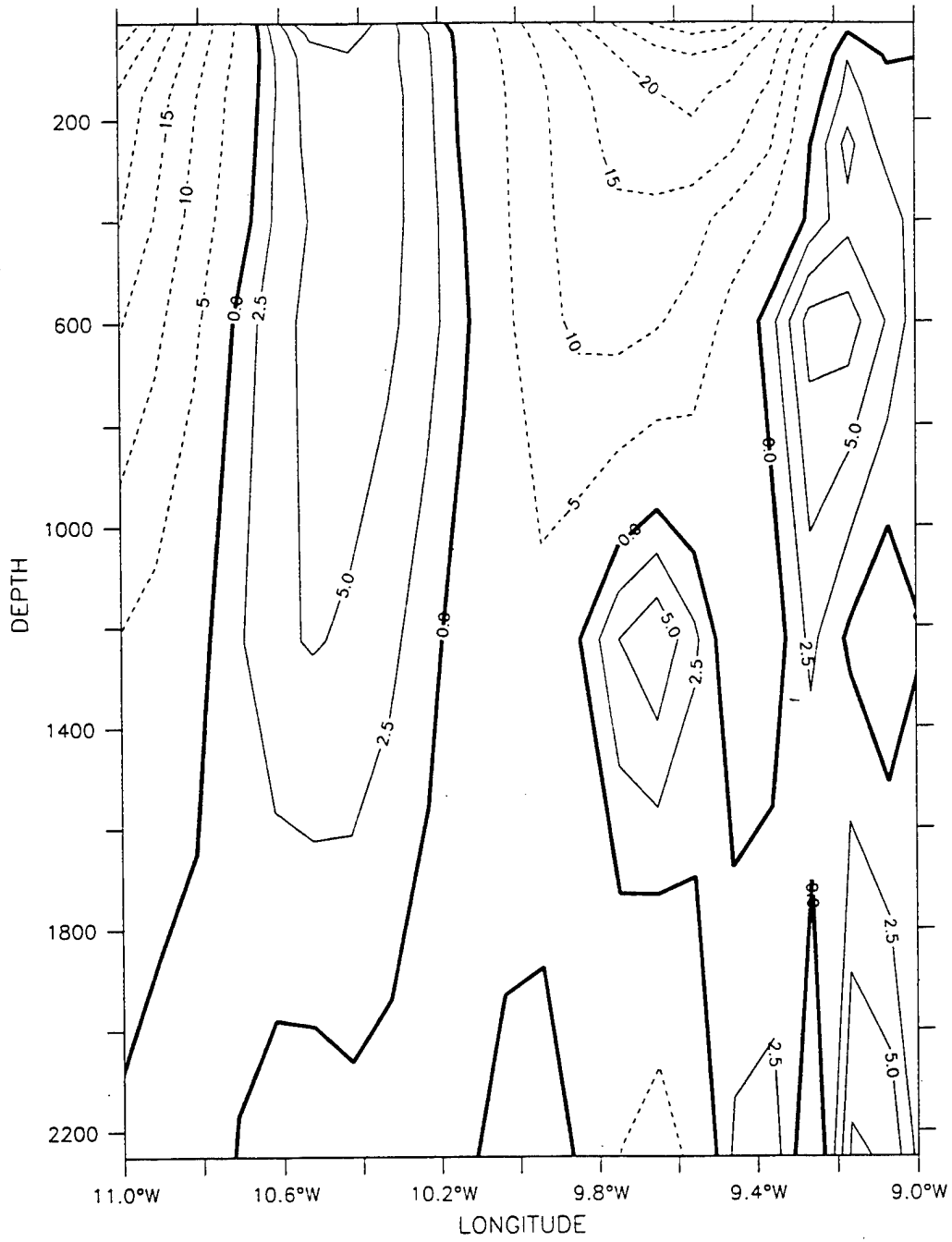
b.

LATITUDE : 38.6N

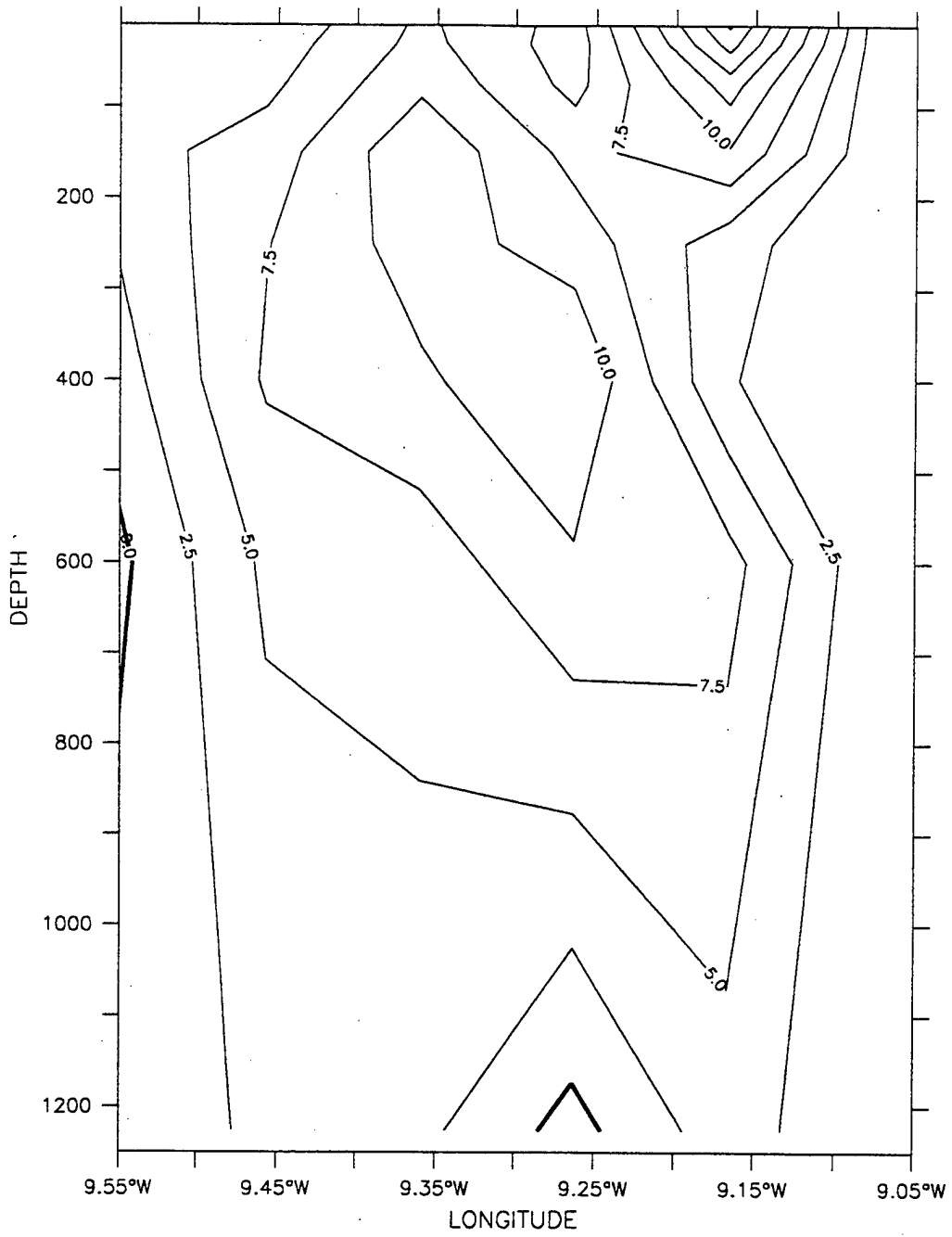


C.

LATITUDE : 37.5N



LATITUDE : 41.5N



e.

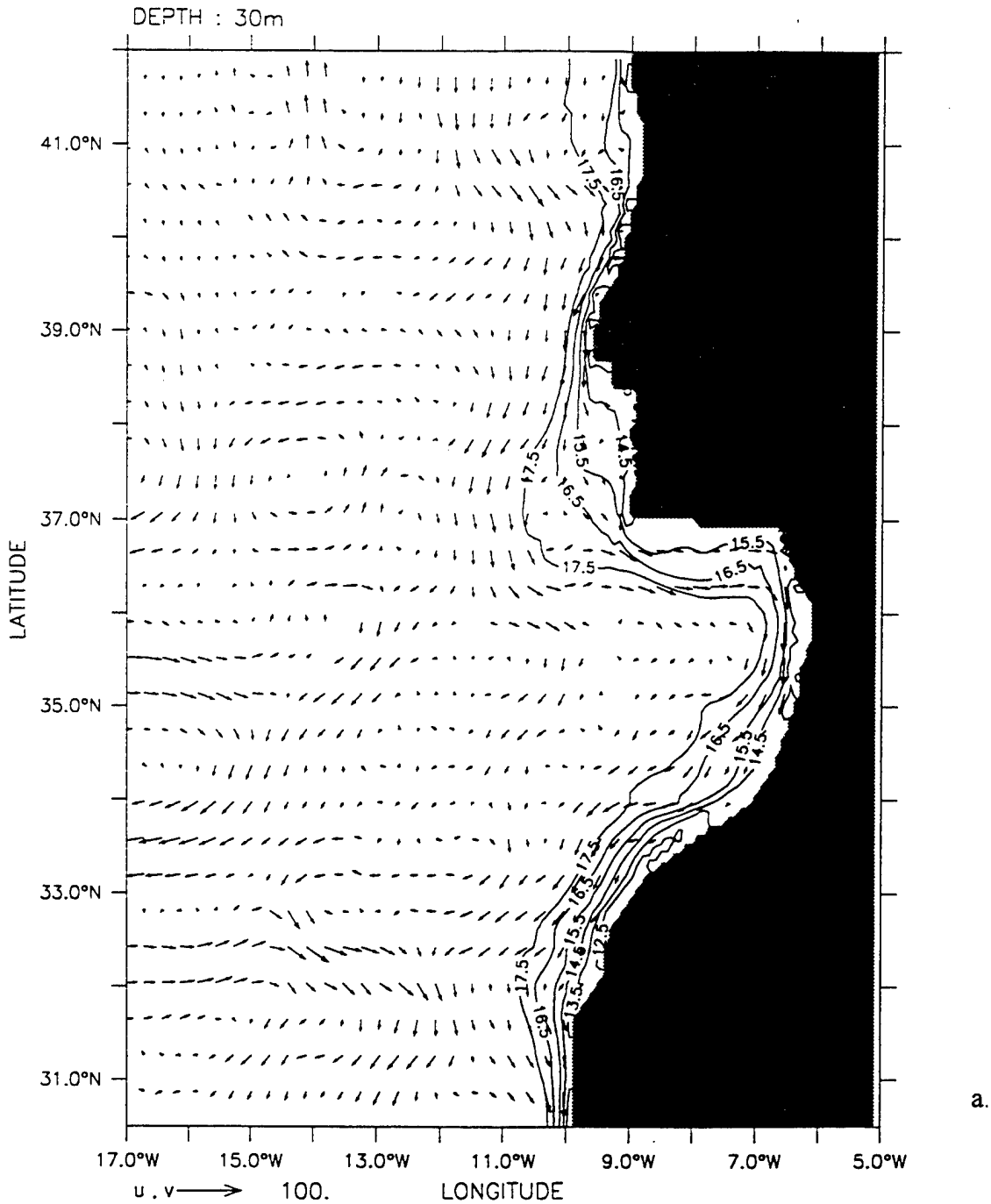
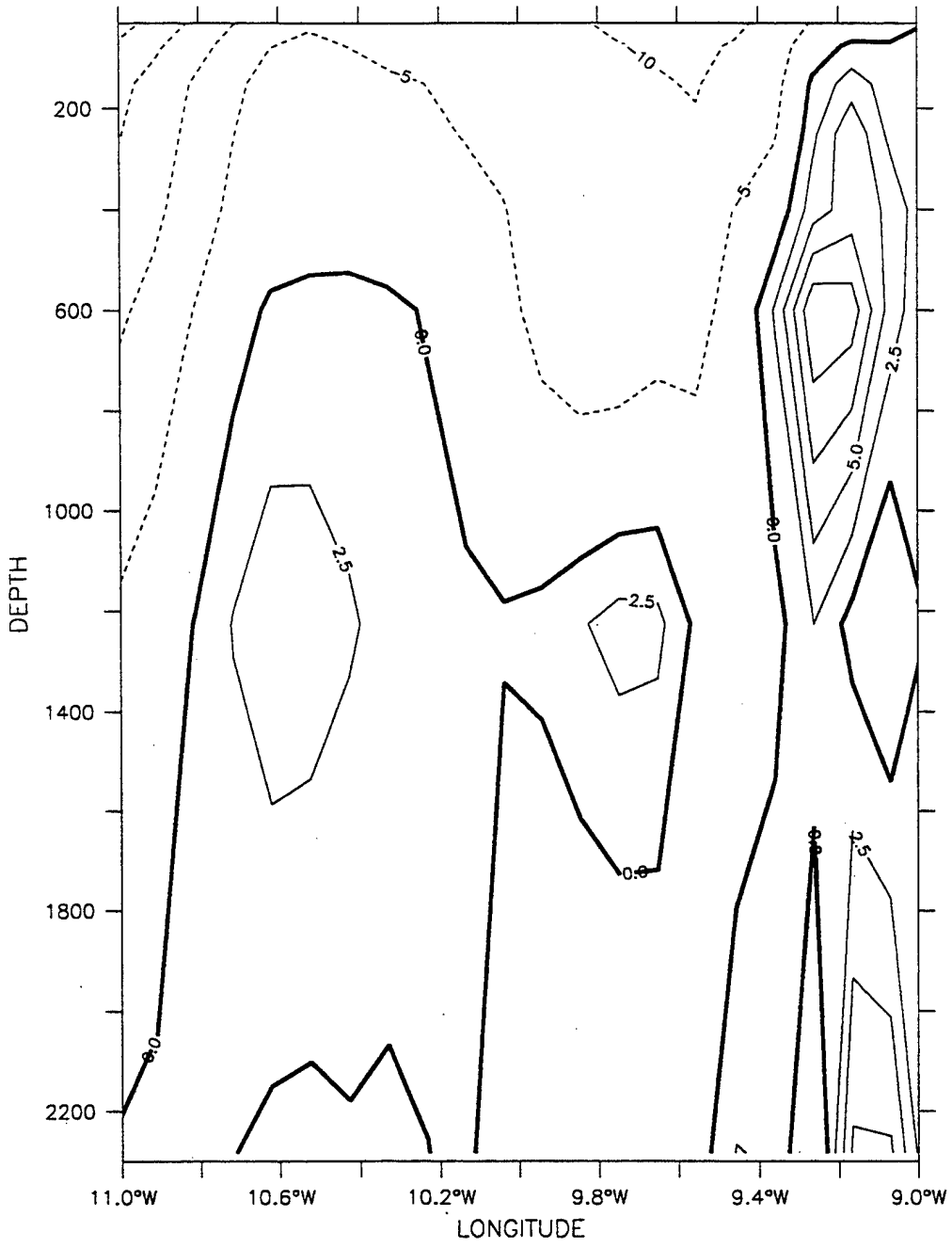


Figure 8. Time-averaged plots for the peak upwelling season (July-September) of temperature contours and velocity vectors (a) at 30 m depth and (d) at 1226 m depth, and a cross-shore section of velocity (v) at (b) 37.5° N, (c) 39° N and (e) 37.4° N . The contour interval is 1° C in (a). The maximum current velocity is 100 cm/s in (a) and 40 cm/s in (d). In (b), (c) and (e) solid lines indicate poleward flow, while dashed lines indicate equatorward flow. The contour interval for poleward flow is 2.5 cm/s in (b) and (c) and 5 cm/s in (e). The contour interval for equatorward flow is 5 cm/s.

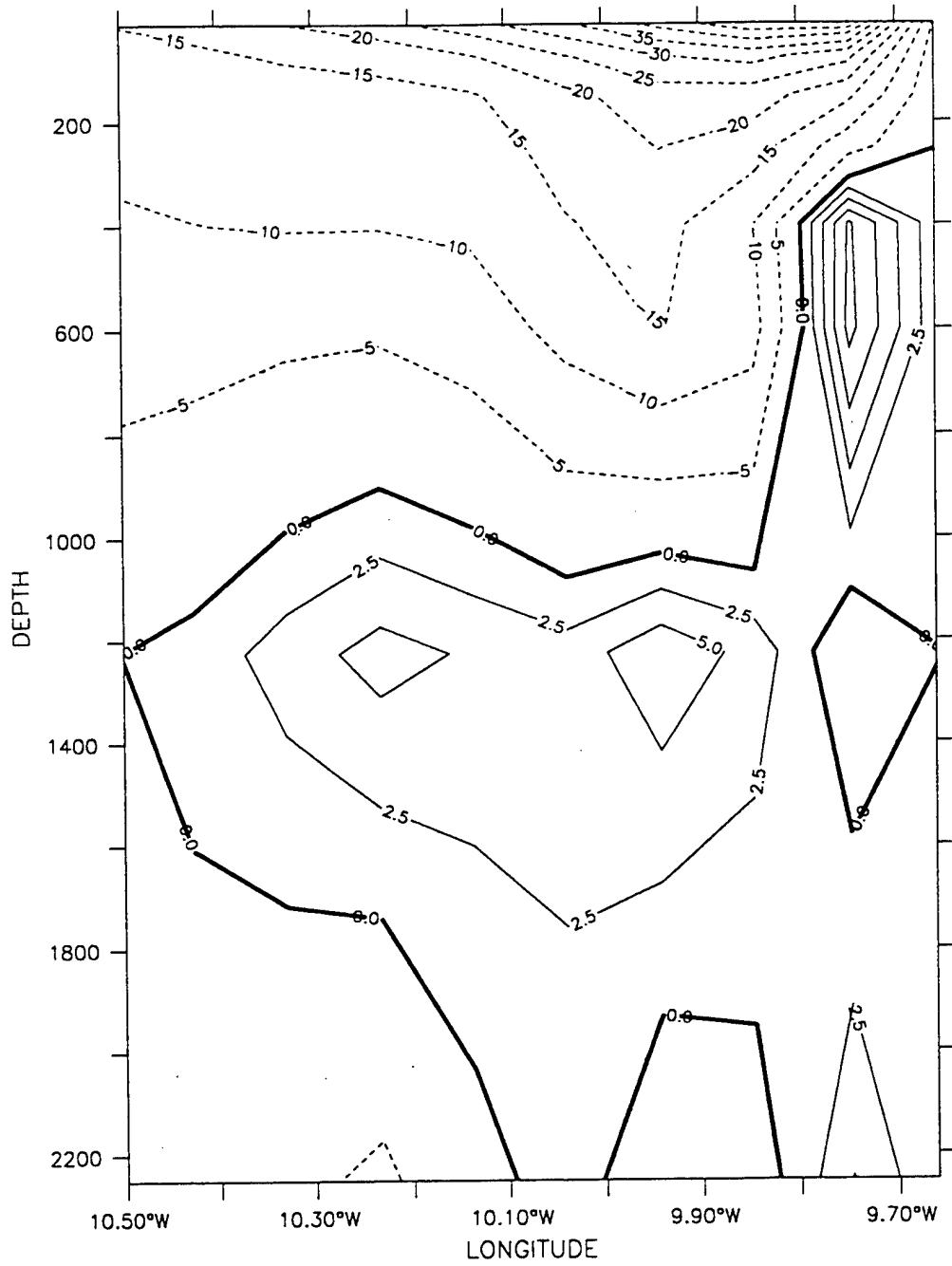


LATITUDE : 37.5N



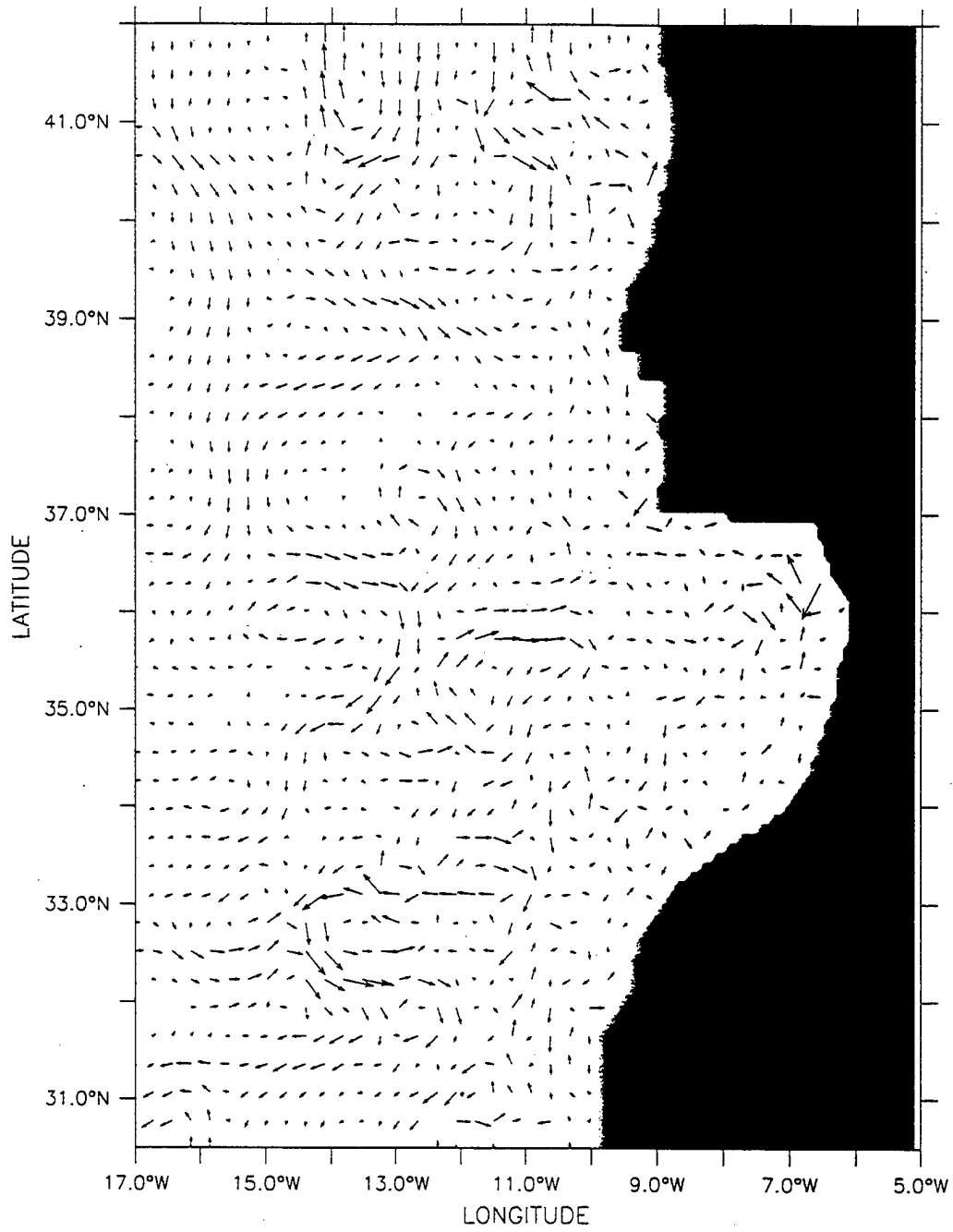
b.

LATITUDE : 39N



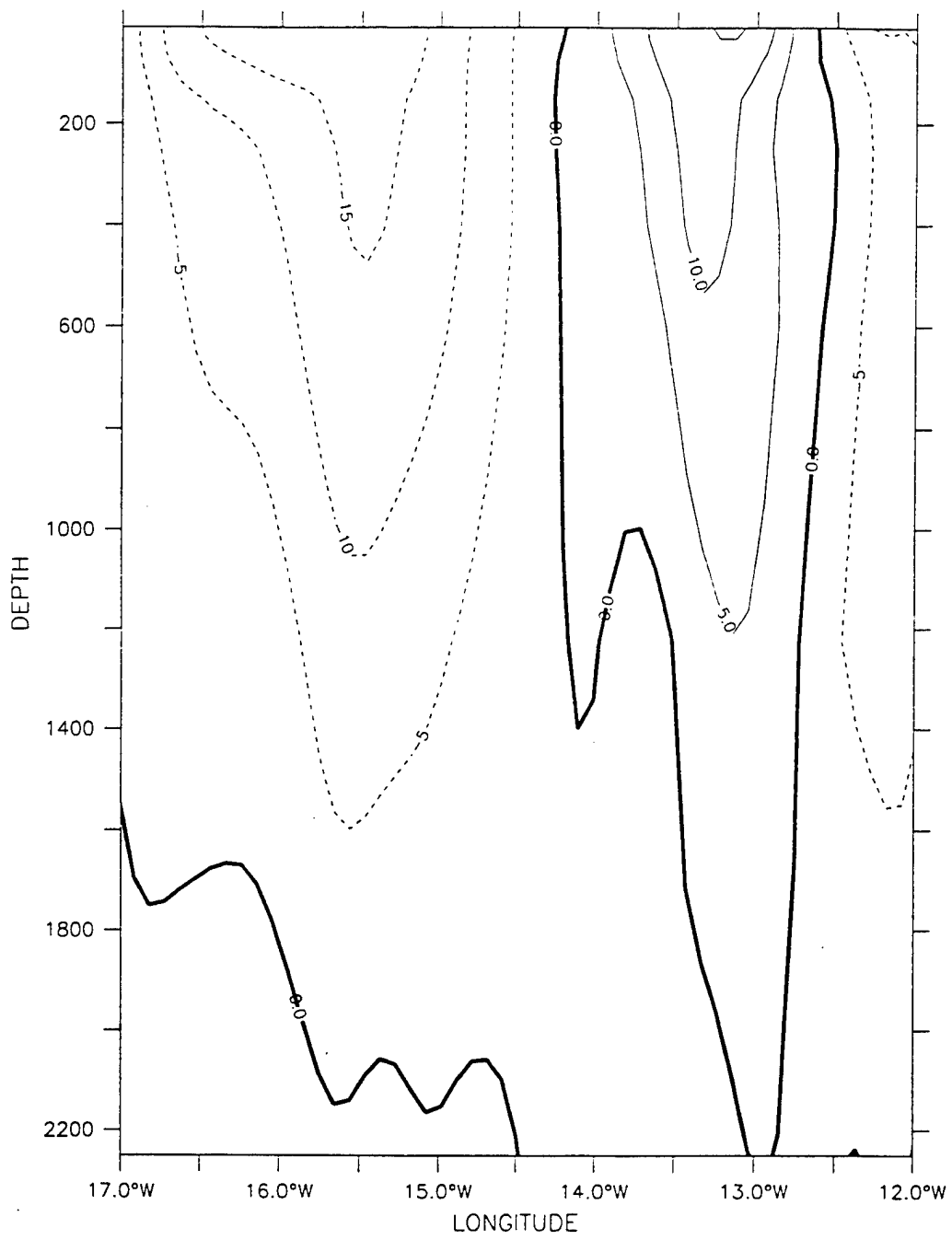
c.

DEPTH : 1226m



d.

LATITUDE : 37.4N



e.

DEPTH : 30m

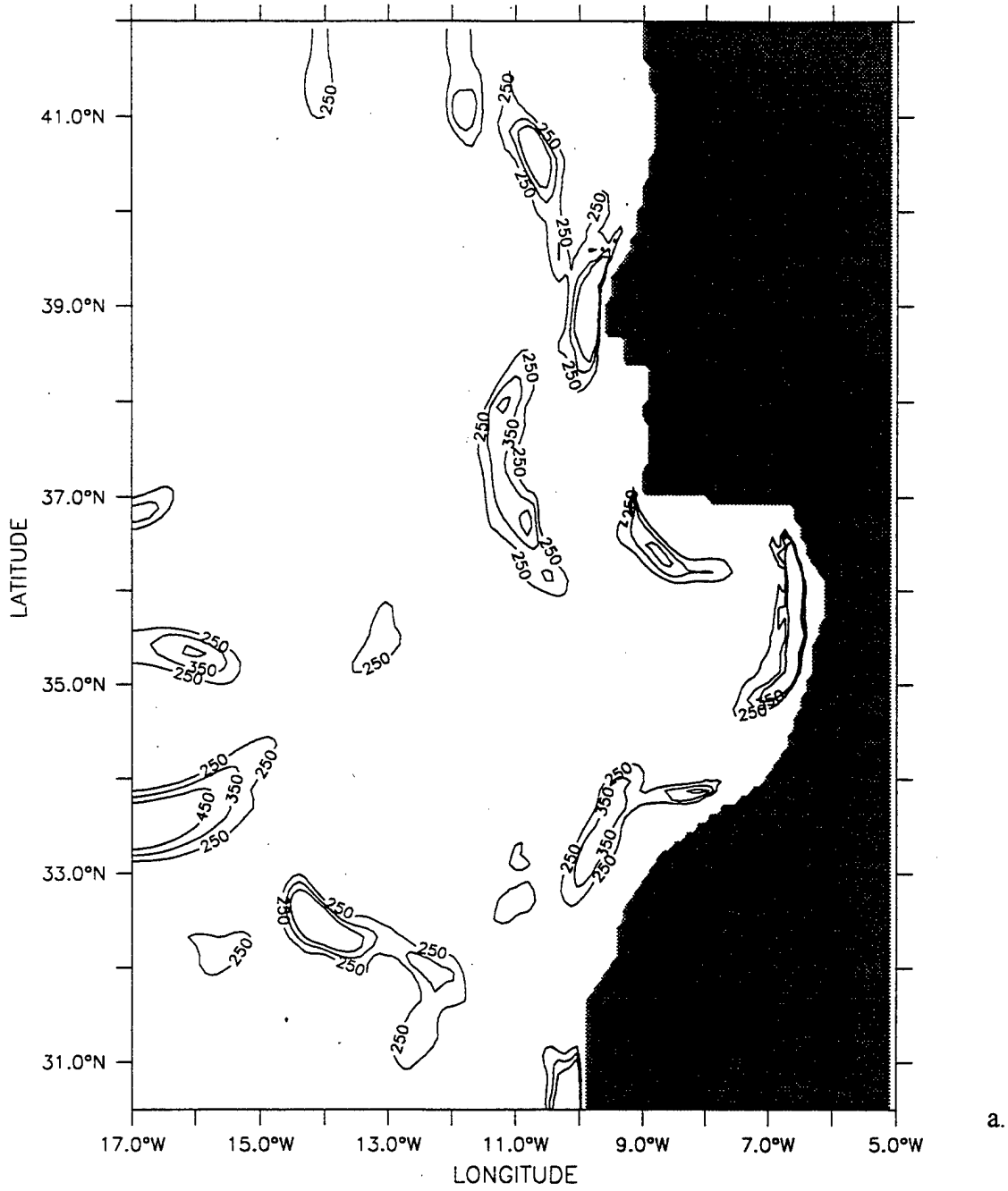
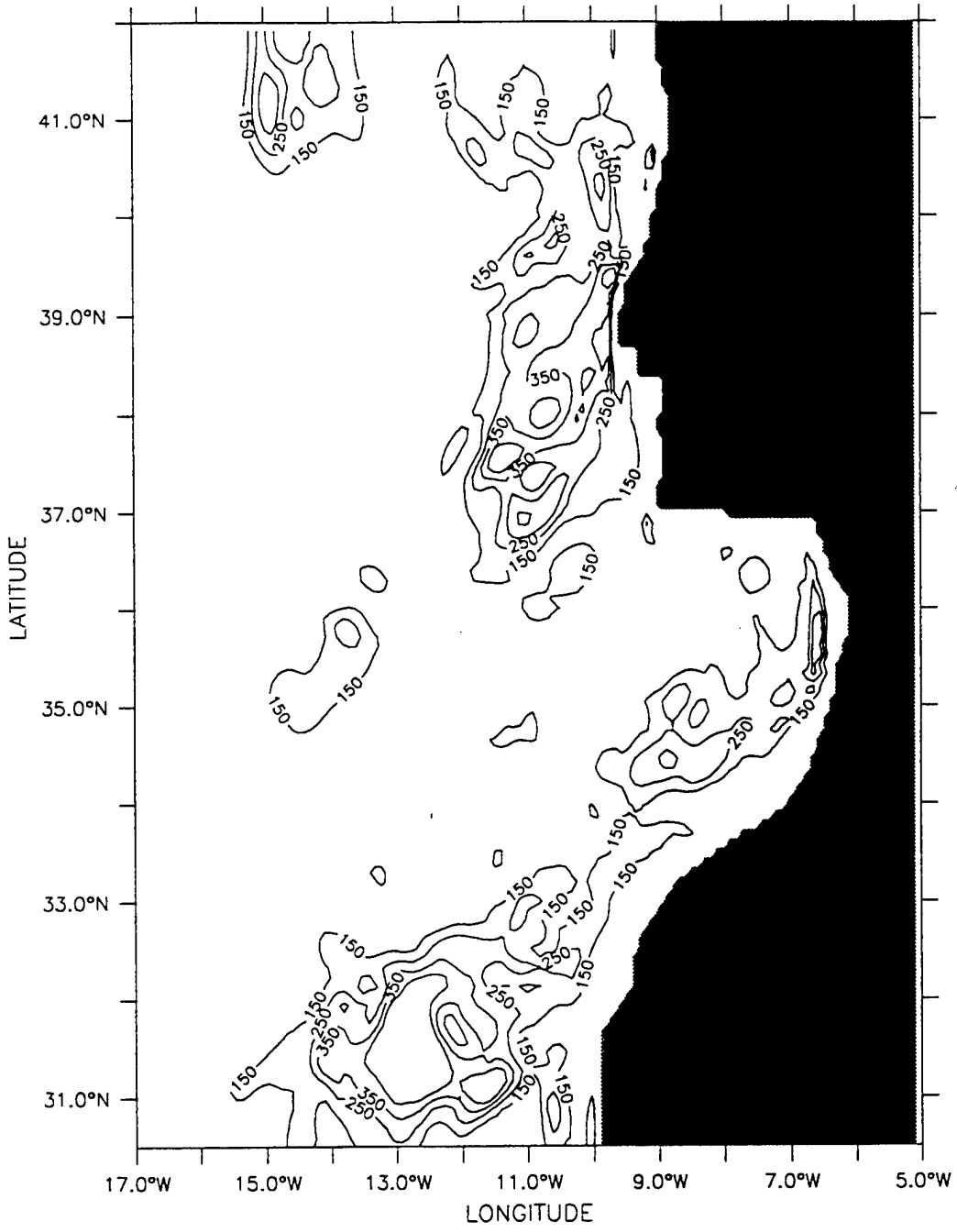


Figure 9. (a) Mean and (b) eddy kinetic energy at 30 m depth for the peak upwelling season (July through September). Contour interval is  $100 \text{ cm}^2/\text{s}^2$ .

DEPTH : 30m



b.

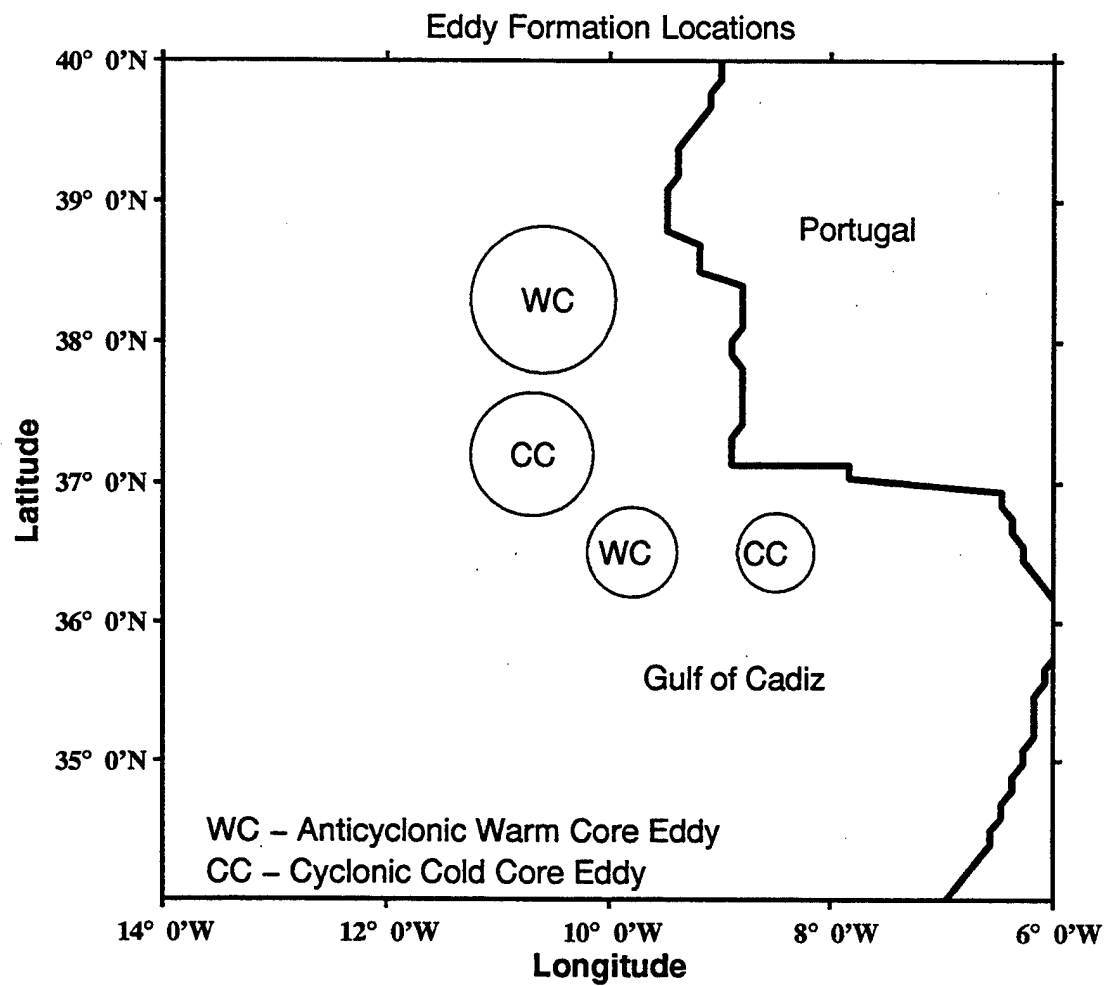


Figure 10. Computer representation of AVHRR NOAA7 Sea Surface Temperatures (SST) with observed eddy formations from 5 August 1982. "After Fiuza 1984."

DEPTH : 30m

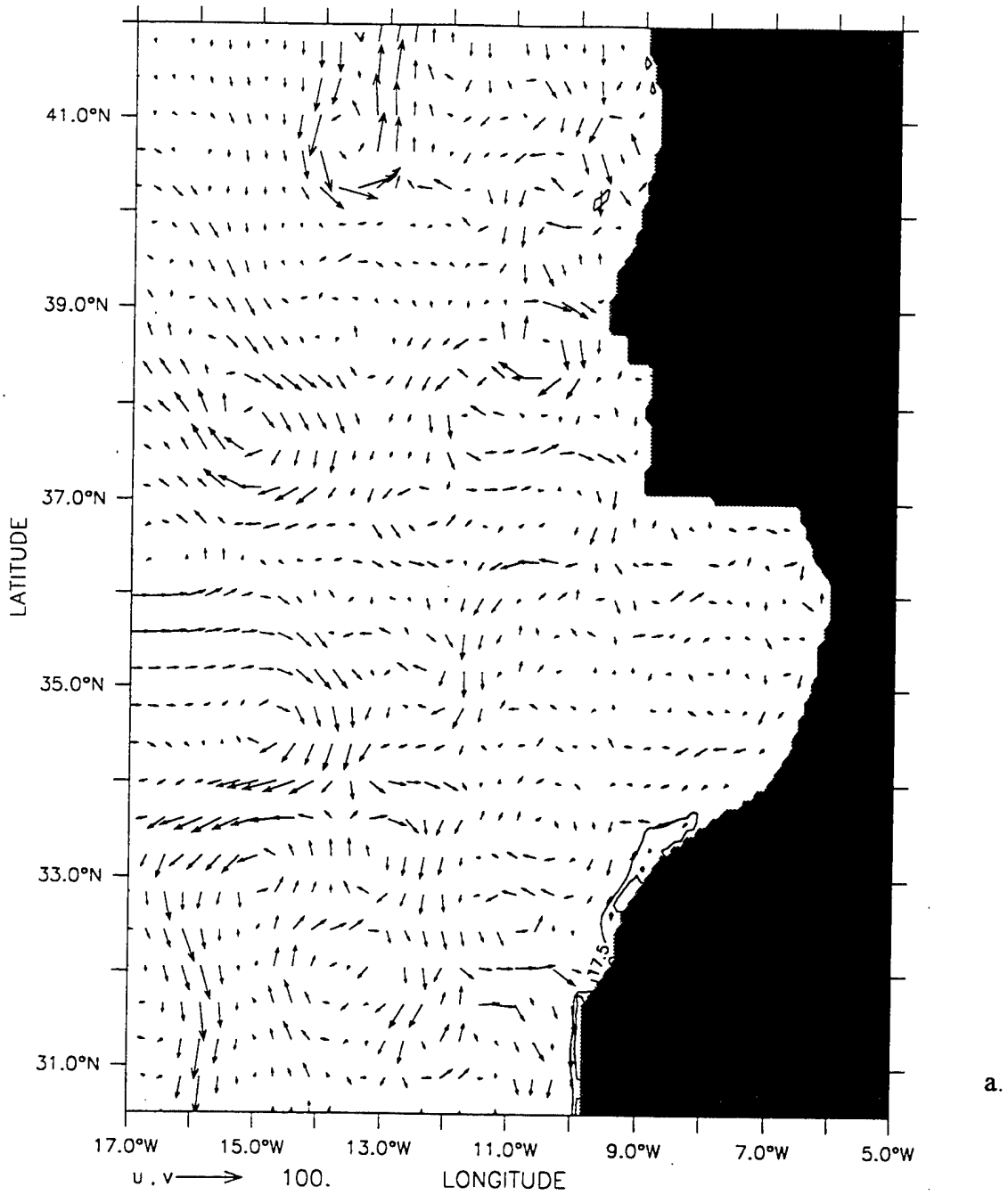
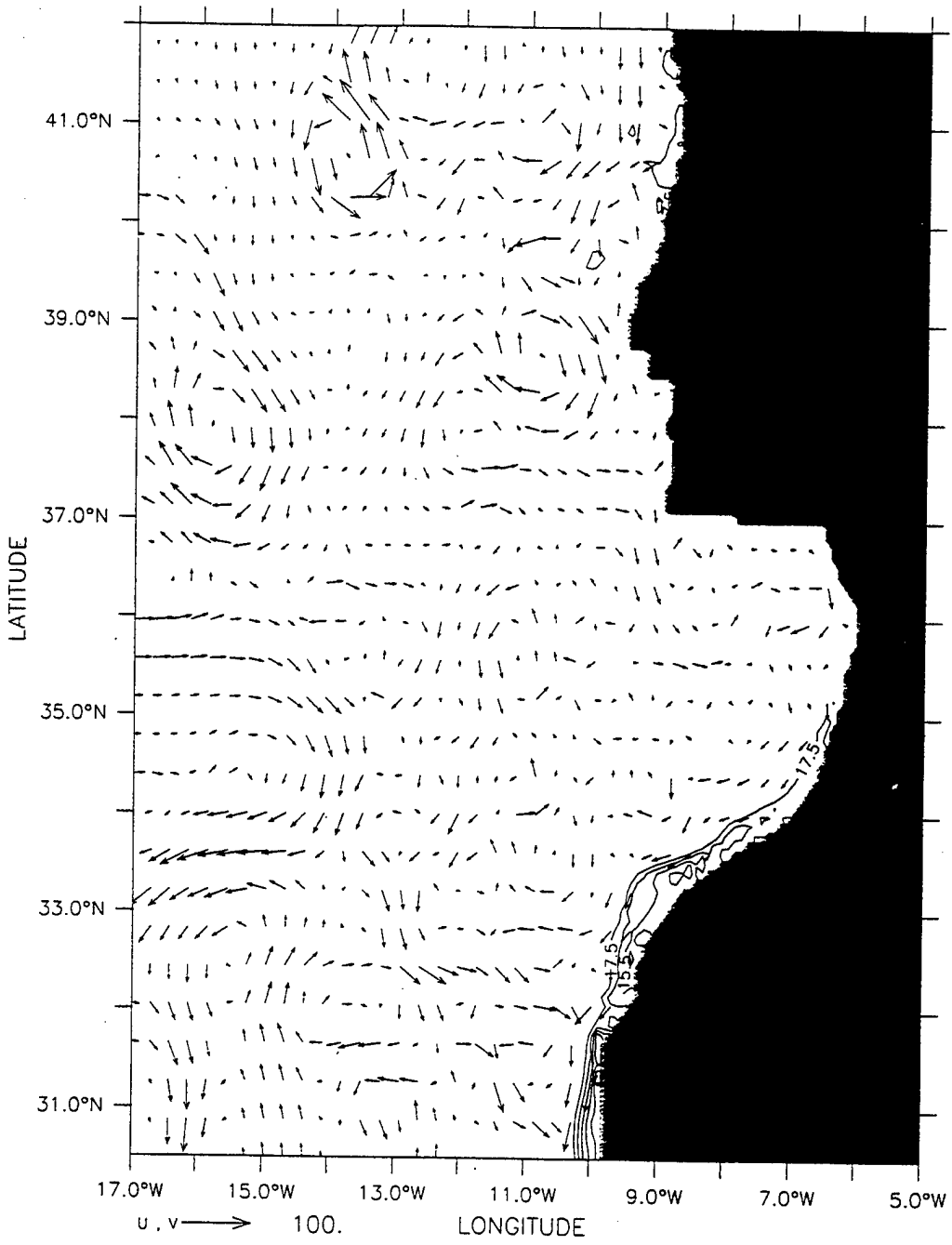


Figure 11. Temperature contours and velocity vectors at 30 m showing upwelling in the third year at day (a) 137, (b) 152, (c) 173, (d) 209, (e) 263, (f) 290, and (g) 317. The contour interval is  $1^{\circ}$  C. The maximum current velocity is 100 cm/s.

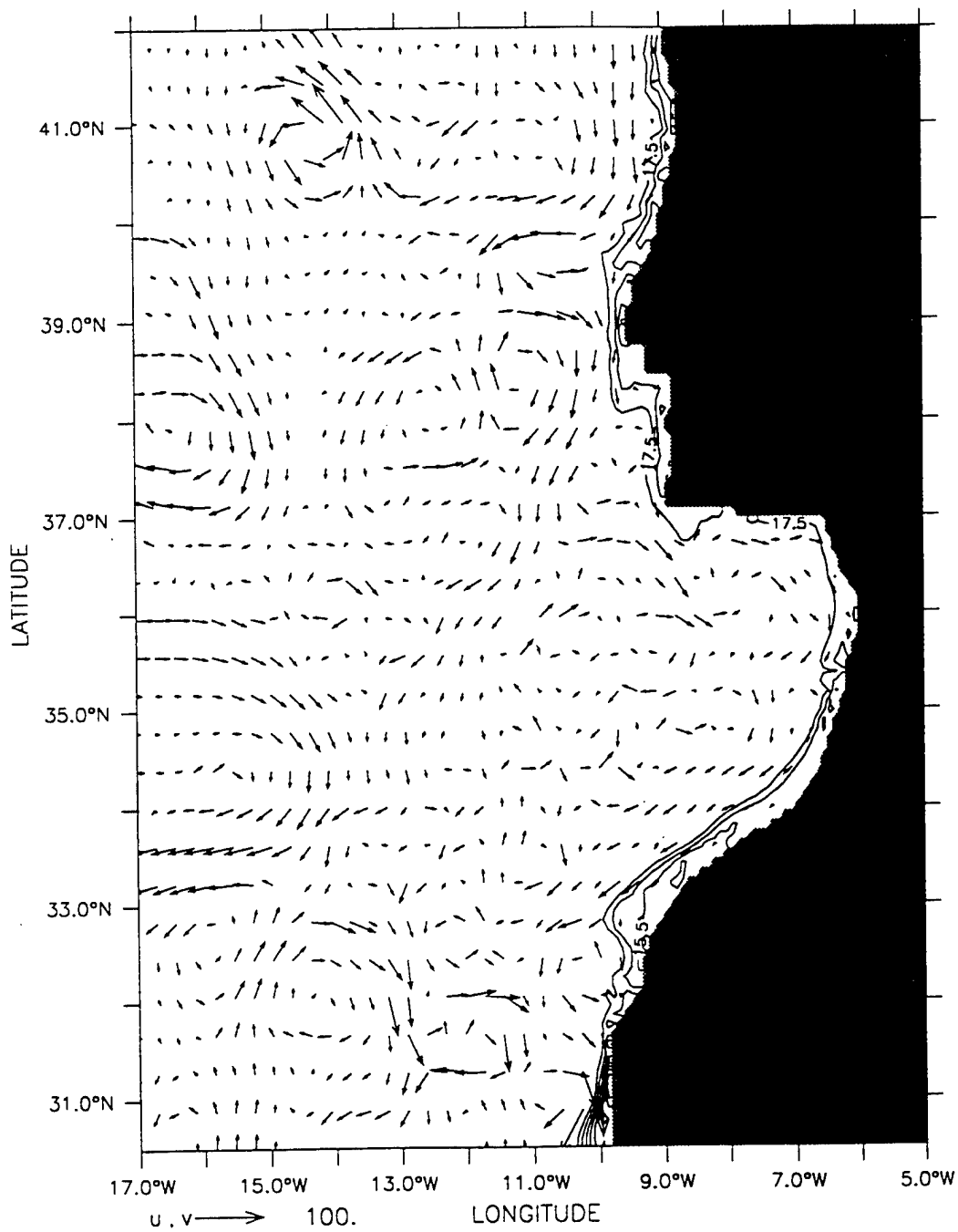


DEPTH : 30m

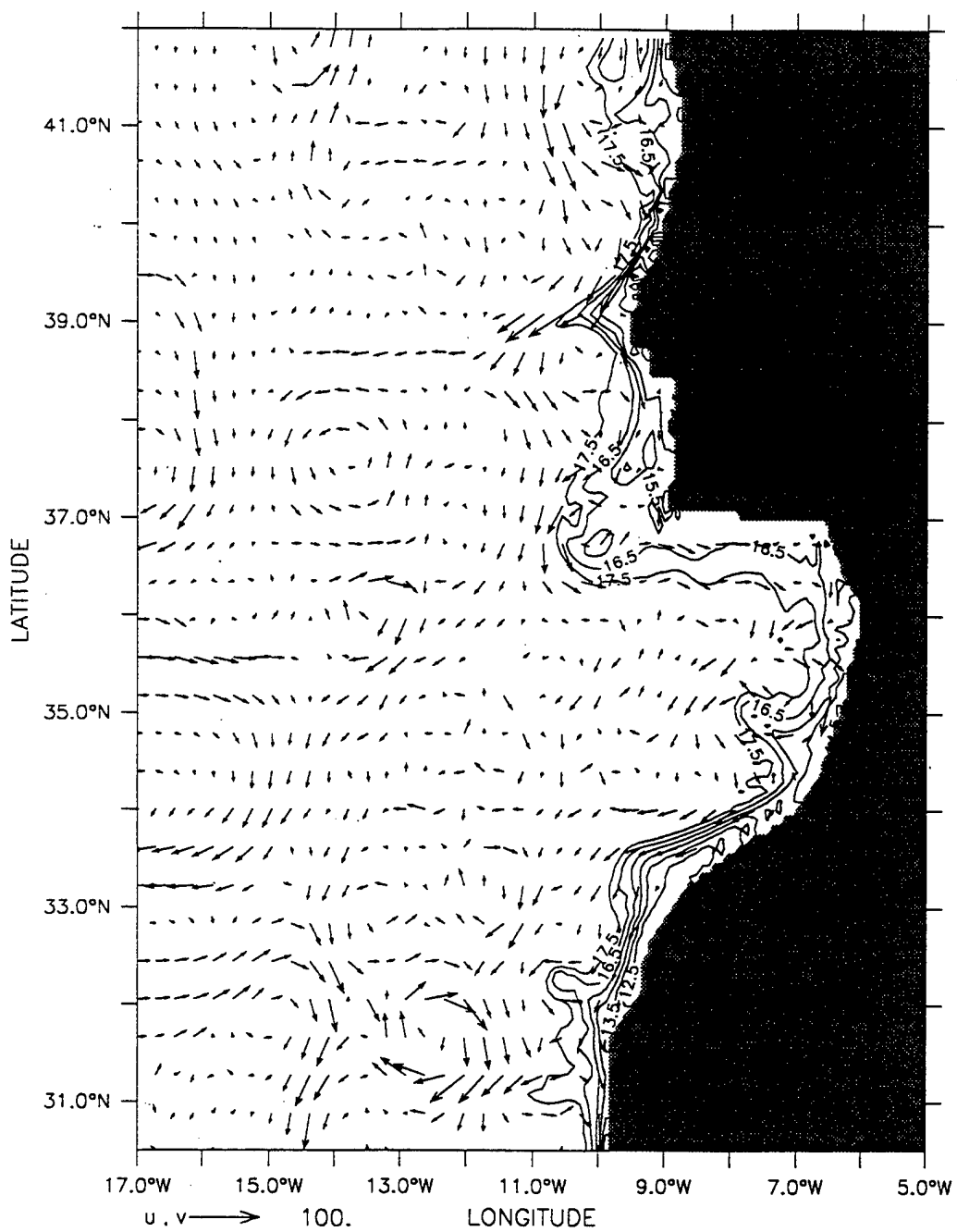


b.

DEPTH : 30m

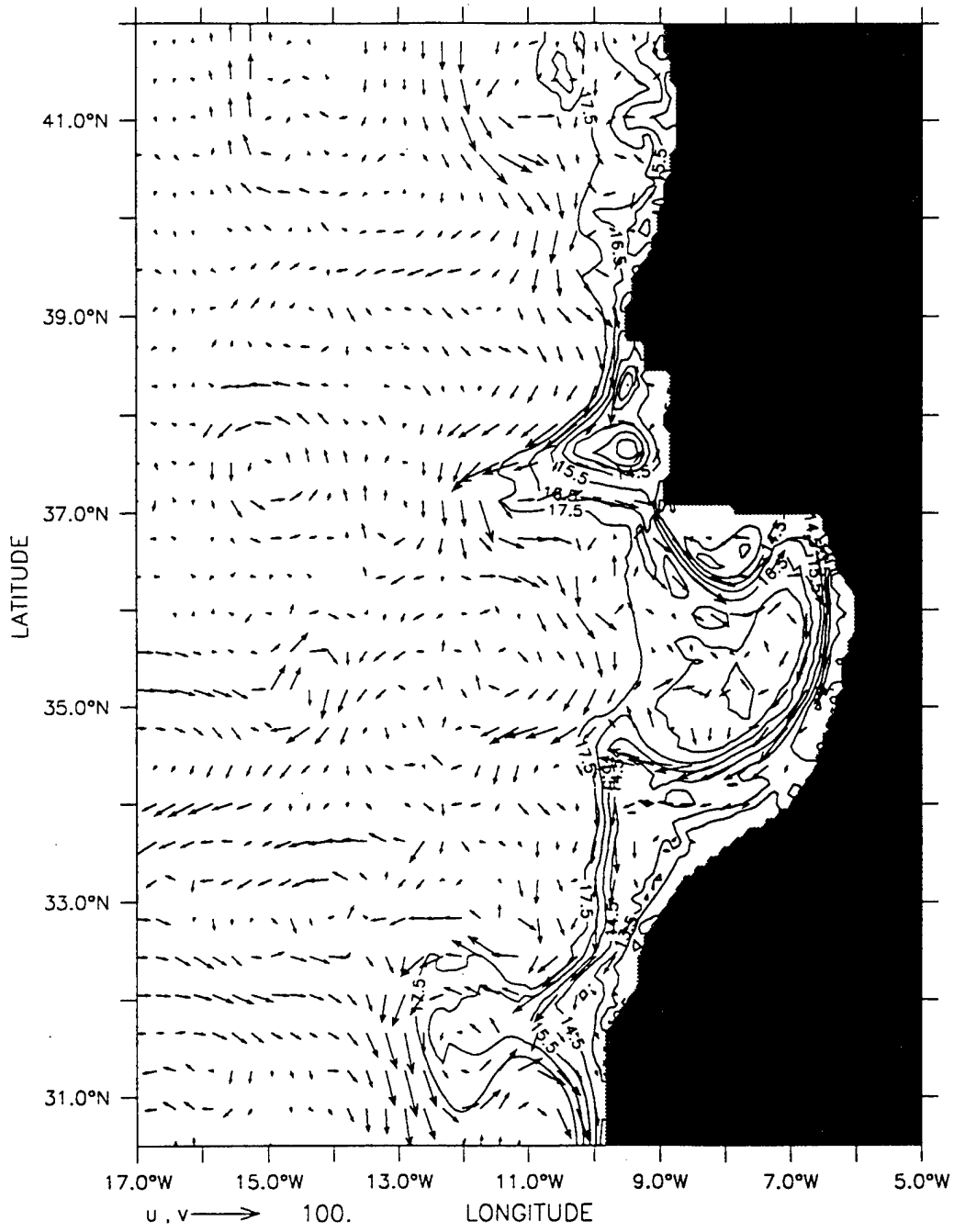


DEPTH : 30m



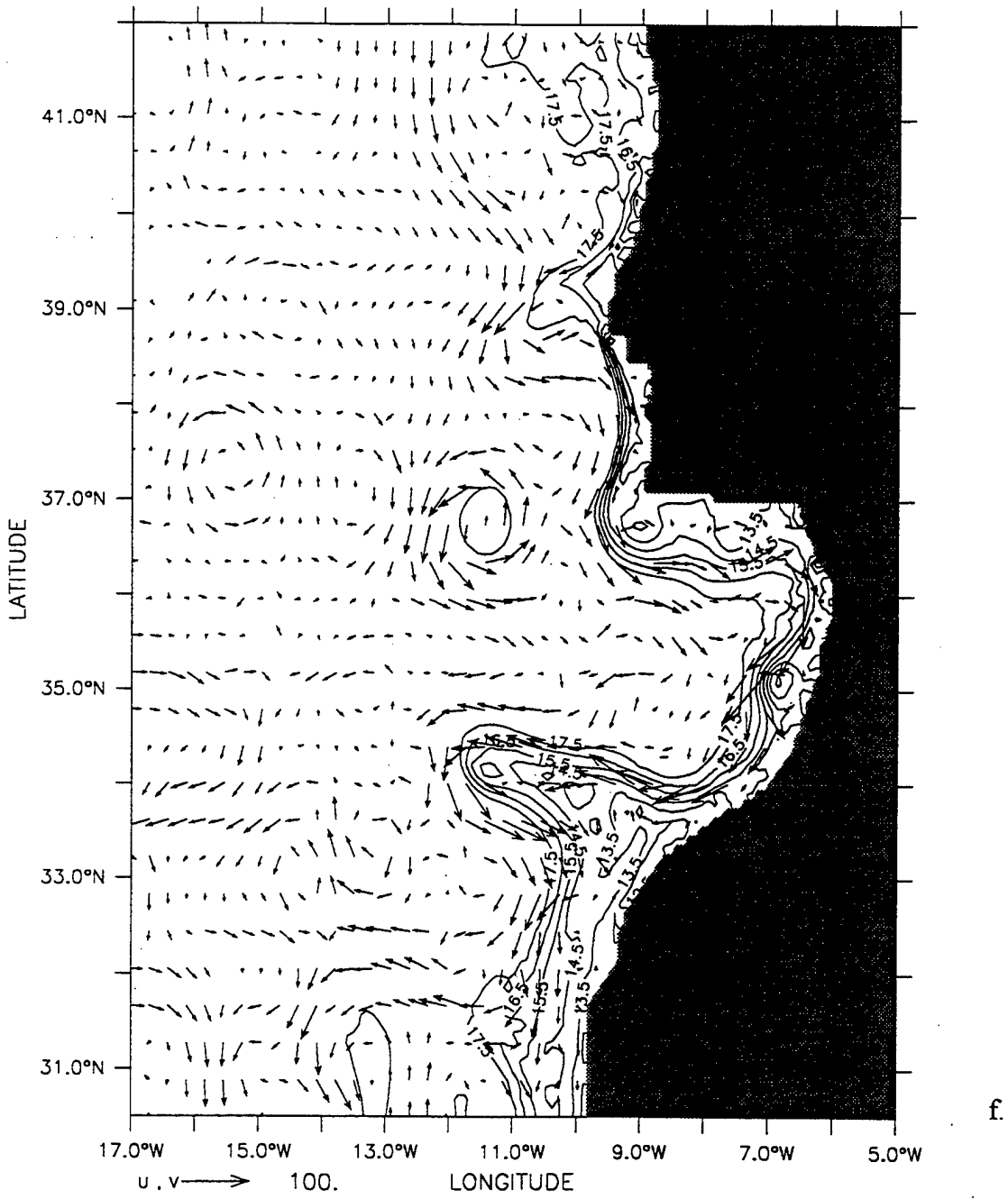
d.

DEPTH : 30m

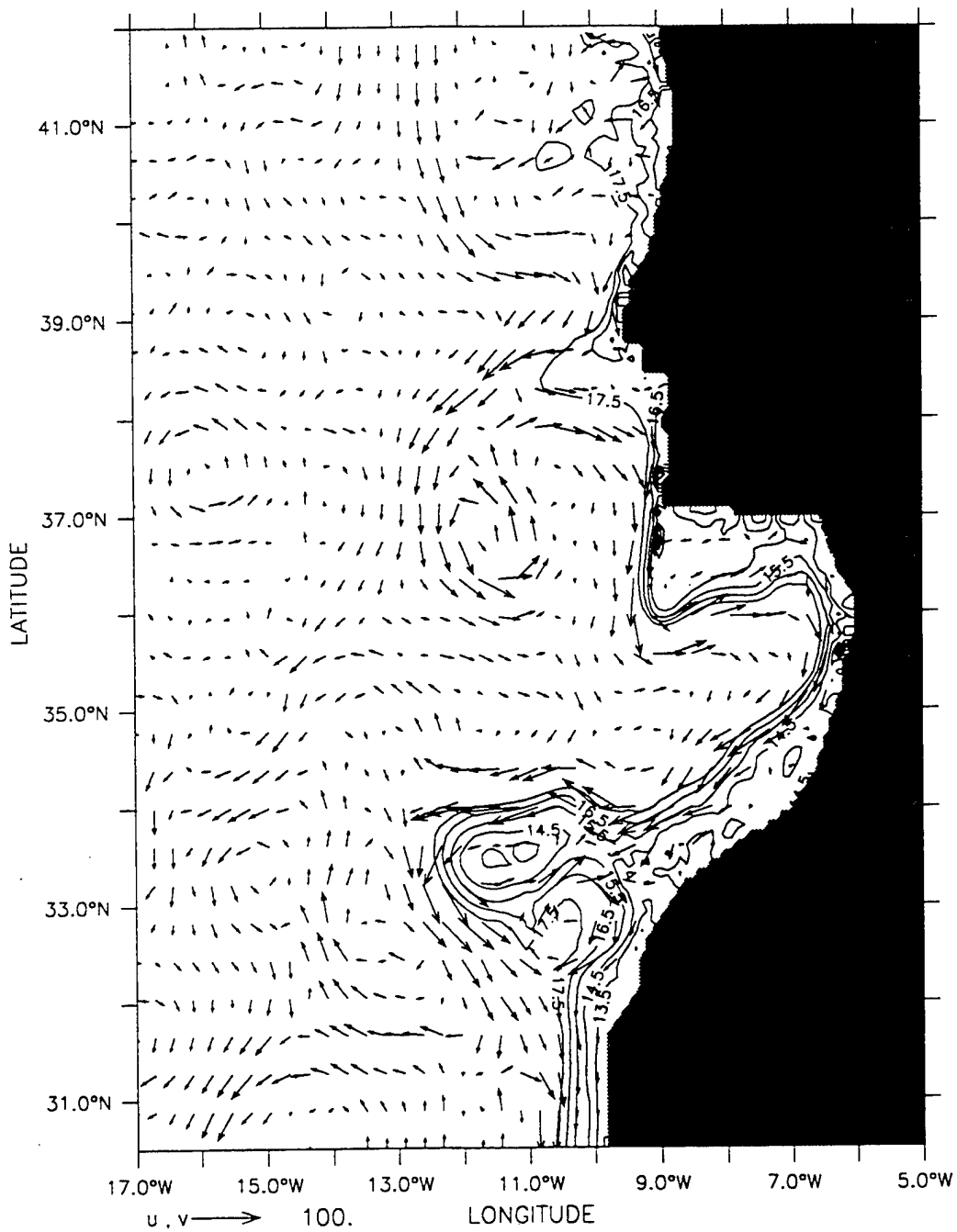


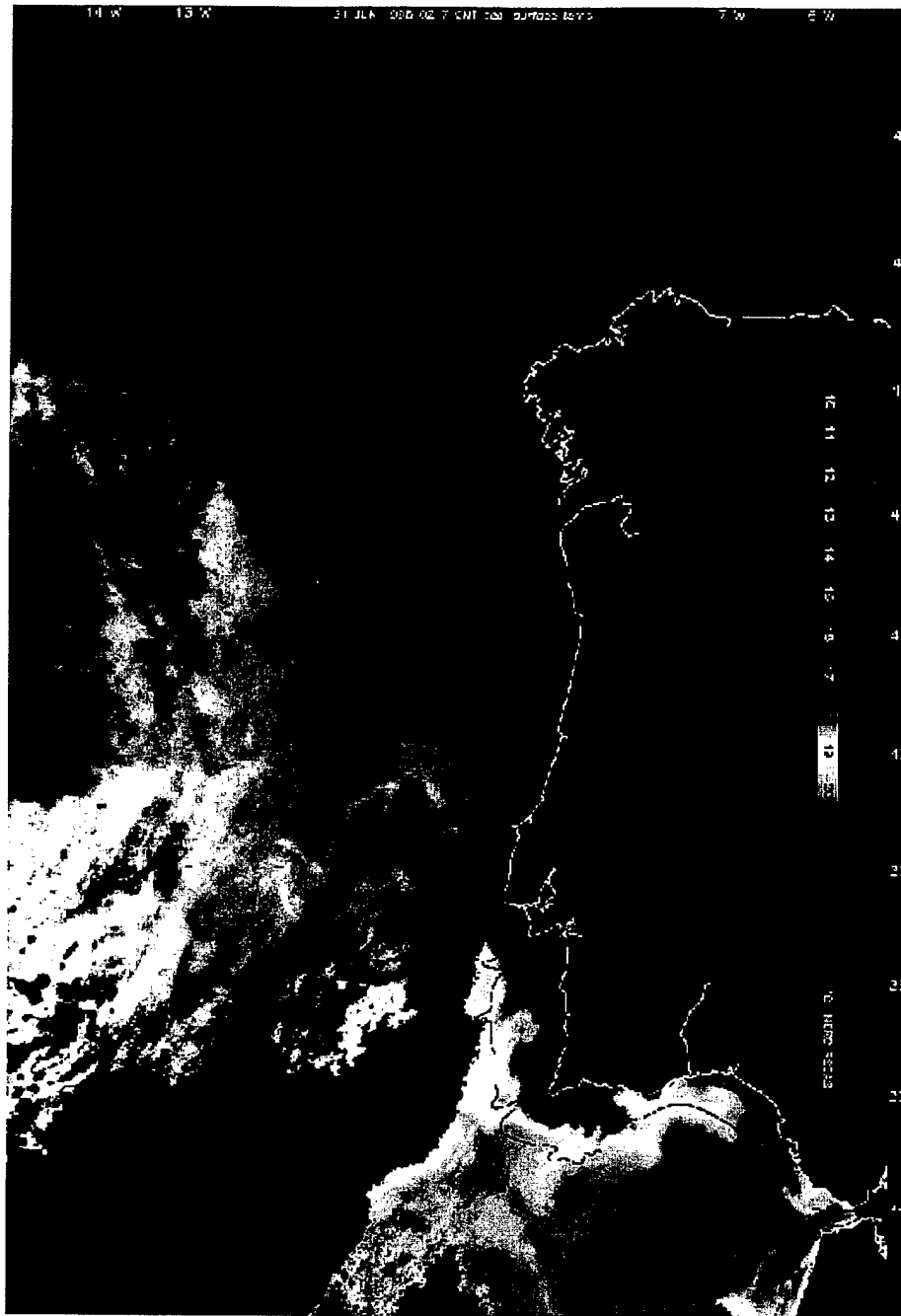
e.

DEPTH : 30m



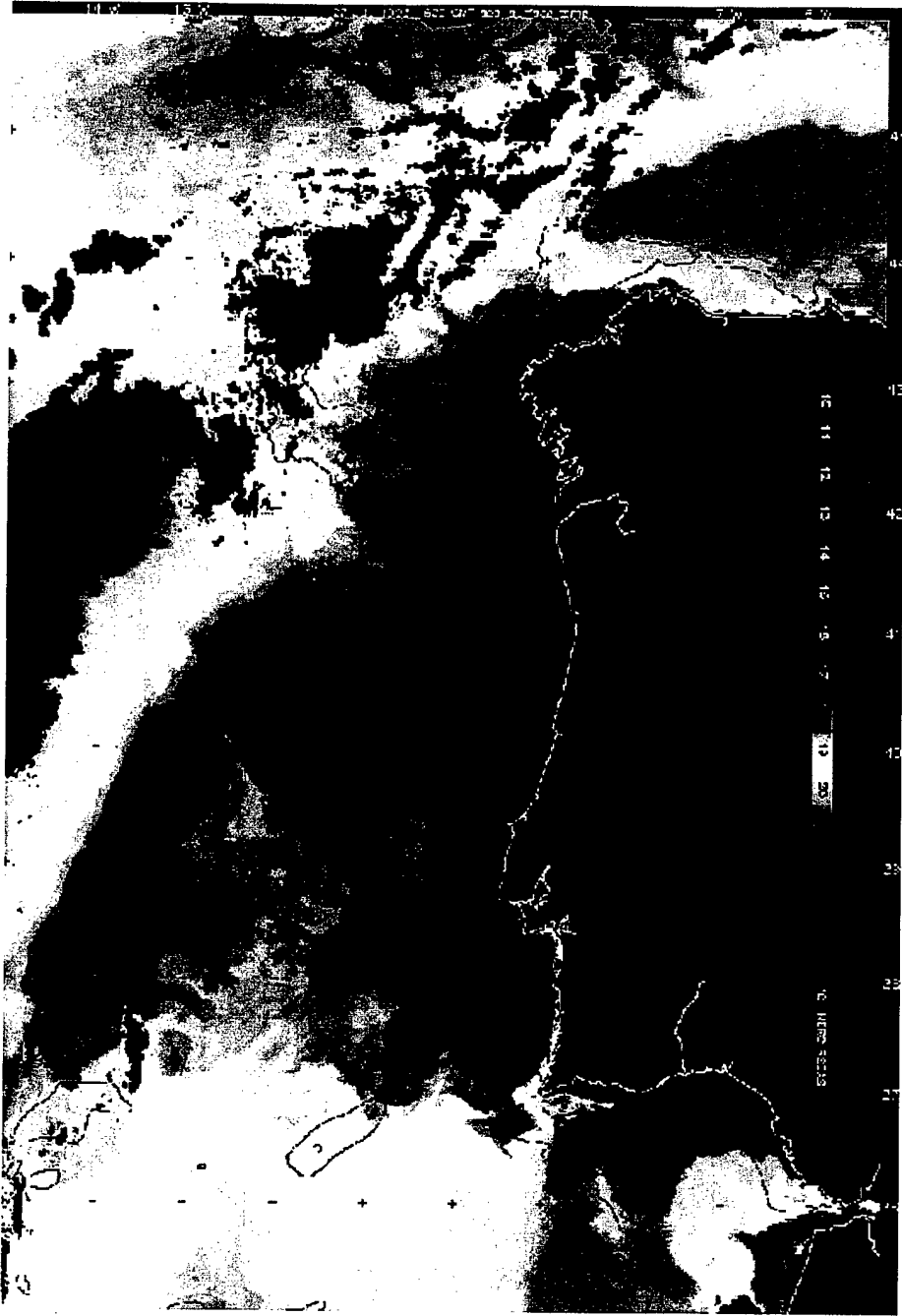
DEPTH : 30m





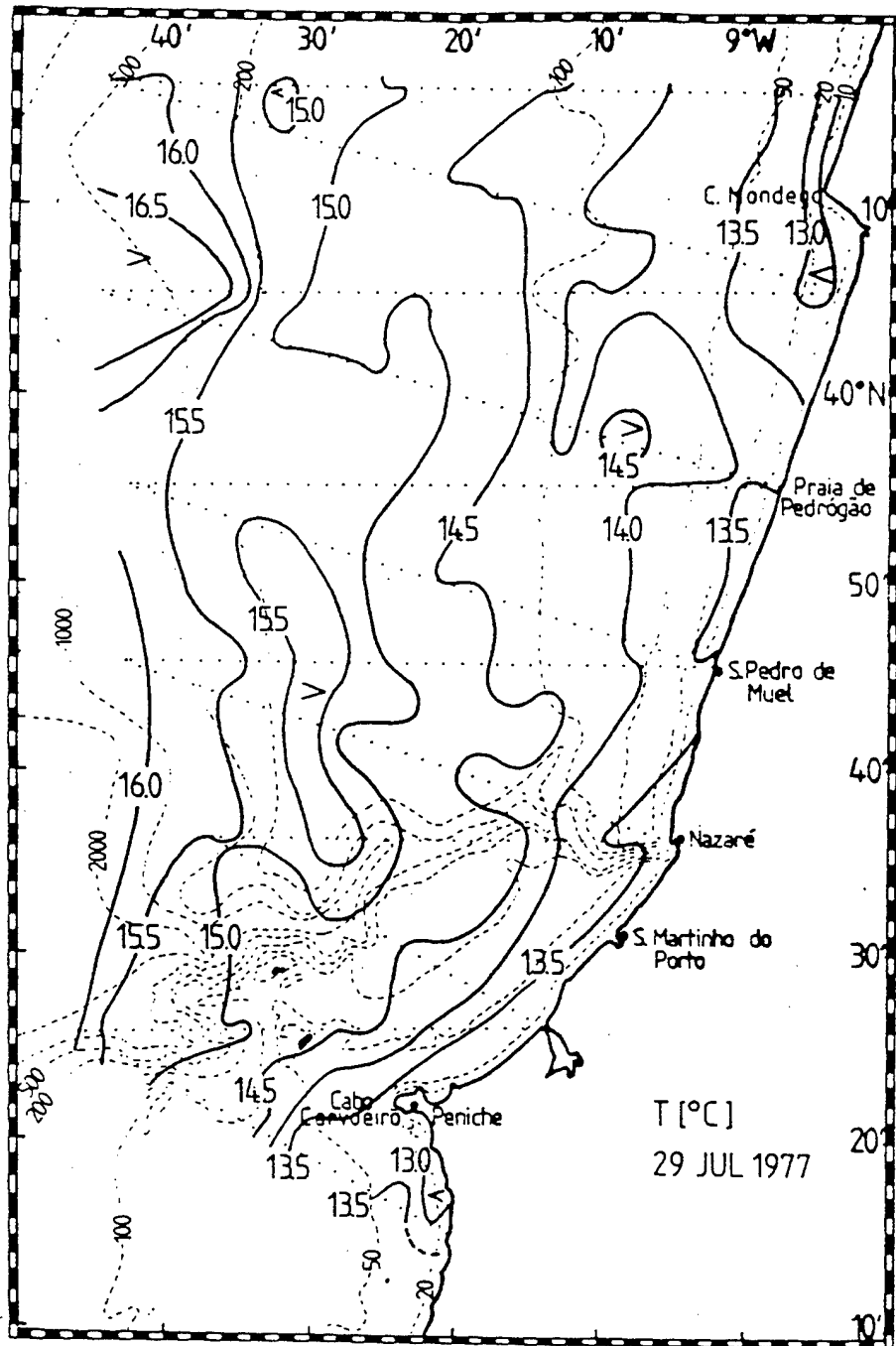
a.

Figure 12. AVHRR sea surface temperatures (SST) from (a) 21 June 1995 showing increased cold SST southwest of Cabo de Sao Vincent caused by intensified upwelling and advection of upwelled water around the cape and (b) 27 July 1993 showing strong upwelling and numerous filaments off the west coast of the IP. In (c) SST show intense upwelling north of Cabo da Roca on 29 July 1977. Figures (a) and (b) are from the Remote Sensing Data Analysis Service (RSDAS), Plymouth Marine Laboratory, UK. Figure (c) is from Fiuza (1982).



b.





c.



## APPENDIX. METHOD OF SOLUTION

Equations (1) through (7) comprise a closed system of seven scalar equations and seven unknowns,  $u$ ,  $v$ ,  $w$ ,  $p$ ,  $\rho$ ,  $T$ , and  $S$ . The variables,  $u$ ,  $v$ ,  $T$ , and  $S$  are prognostic variables whose time rates of change are predicted from (1), (3), (6) and (7), respectively. Although the diagnostic variables  $w$ ,  $p$ , and  $\rho$  can be determined from (3), (4), and (5), respectively, additional constraints are imposed on  $p$  and  $w$  by the choice of the rigid lid boundary conditions. The vertically integrated pressure can no longer be obtained by integrating the hydrostatic equation (4) for the free surface, and the vertically-integrated horizontal velocity is subsequently constrained to be non-divergent, i.e.,

$$\int_{-H}^0 \left( \frac{\partial u}{\partial x} + \frac{\partial v}{\partial y} \right) d\varepsilon = 0, \quad (\text{A1})$$

which is obtained by integrating (3) and applying the vertical boundary conditions where  $\varepsilon$  is a dummy variable representing the vertical coordinate.

For any quantity  $q$ , let its vertical average be denoted by  $\bar{q}$  and its departure (vertical shear) by  $q'$ . From (A1) the vertical mean flow can then be described by a streamfunction  $\psi$ , such that:

$$\bar{u} = -\frac{1}{H} \frac{\partial \psi}{\partial y}, \quad (\text{A2})$$

$$\bar{v} = \frac{1}{H} \frac{\partial \psi}{\partial x}. \quad (\text{A3})$$

The streamfunction  $\psi$  is predicted from the vorticity equation, which is derived by applying the curl operator to the vertical average of (1) and (2), and then using (A2) and (A3), the vorticity equation becomes

$$\begin{aligned}
\frac{\partial \zeta}{\partial t} &= \frac{\partial}{\partial t} \left[ \frac{1}{H} \left( \frac{\partial^2 \psi}{\partial x^2} \right) + \frac{1}{H} \left( \frac{\partial^2 \psi}{\partial y^2} \right) + \frac{\partial \psi}{\partial x} \frac{\partial H^{-1}}{\partial x} + \frac{\partial \psi}{\partial y} \frac{\partial H^{-1}}{\partial y} \right] \\
&= \left[ \frac{\partial}{\partial x} \left( \frac{f}{H} \frac{\partial \psi}{\partial y} \right) - \frac{\partial}{\partial y} \left( \frac{f}{H} \frac{\partial \psi}{\partial x} \right) \right] \\
&\quad - \left[ \frac{\partial}{\partial x} \left( \frac{g}{H \rho_0} \int_{-H}^0 \int_z \frac{\partial \rho}{\partial y} d\epsilon dz \right) - \frac{\partial}{\partial y} \left( \frac{g}{H \rho_0} \int_{-H}^0 \int_z \frac{\partial \rho}{\partial x} d\epsilon dz \right) \right] \\
&\quad + \frac{\partial}{\partial x} \left( \frac{1}{H} \int_{-H}^0 G dz \right) - \frac{\partial}{\partial y} \left( \frac{1}{H} \int_{-H}^0 F dz \right),
\end{aligned} \tag{A4}$$

where  $G$  and  $F$  represent the collected contributions of the nonlinear and viscous terms from equations (1) and (2).

The vorticity equation (A4) is solved by obtaining an updated value of  $\zeta$  by application of the leapfrog (or every 11 time steps, the Euler-backward) time-differencing scheme. The associated value of  $\psi$  can then be obtained from:

$$\zeta = \frac{1}{H} \left( \frac{\partial^2 \psi}{\partial x^2} \right) + \frac{1}{H} \left( \frac{\partial^2 \psi}{\partial y^2} \right) + \frac{\partial \psi}{\partial x} \frac{\partial H^{-1}}{\partial x} + \frac{\partial \psi}{\partial y} \frac{\partial H^{-1}}{\partial y}, \tag{A5}$$

which is an elliptic equation. A solution to (A5) is fully prescribed by specifying the values of  $\psi$  on the open and closed boundaries of the model domain. Currently, to solve (A5), the model uses an elliptic solver when there are no variations in coastline geometry and/or topography, and successive over-relaxation techniques when there are variations in coastline geometry and/or topography.

The vertical shear current ( $u'$ ,  $v'$ ) is predicted from (1) and (2) after subtracting the vertical mean flow. The results are:

$$\frac{\partial u'}{\partial t} = \frac{-1}{\rho_0} \frac{\partial p'}{\partial x} + f v' - A_M \nabla^4 u' + K_M \frac{\partial^2 u'}{\partial z^2} + F - \bar{F} - \frac{\tau^y}{\rho_0 H}, \tag{A6}$$

$$\frac{\partial v'}{\partial t} = \frac{-1}{\rho_0} \frac{\partial p'}{\partial y} - f u' - A_M \nabla^4 v' + K_M \frac{\partial^2 v'}{\partial z^2} + G - \bar{G} - \frac{\tau^x}{\rho_0 H}. \tag{A7}$$

In (A6) and (A7),  $p'$ , which represents the departure of the pressure from the vertical average, is, using (4), expressed in terms of  $\rho$  as:

$$p' = \int_z^0 \rho g d\epsilon - \frac{1}{H} \int_{-H}^0 \left( \int_z^0 \rho g d\epsilon \right) dz. \tag{A8}$$

The method of solution consists of predicting  $\nabla^2\psi, \psi, u', v', T$ , and  $S$  from (A4), (A5), (A6), (A7), (6) and (7), respectively. The total current is then obtained by adding the vertical shear part to the vertical average part, after the latter is obtained from  $\psi$  using (A2) and (A3). The diagnostics  $\rho$ ,  $w$ , and  $p'$  are then obtained explicitly from the equation of state (5), continuity equation (A1), and hydrostatic relation (A8), respectively.



**Table 1. Values of Constants Used in the Model**

| Constant   | Value  | Definition                                |
|------------|--|---|
| $T_0$      | 278.2°K  | Constant Reference Temperature            |
| $S_0$      | 34.7   | Constant Reference Salinity               |
| $\rho_0$   | 1.0276 gm cm <sup>3</sup>                      | Density of Sea Water At $T_0$ and $S_0$   |
| $\alpha$   | $2.4 \times 10^{-4} (\text{°K})^{-1}$          | Thermal Expansion Coefficient             |
| $\beta$    | $7.5 \times 10^{-4}$                           | Saline Expansion Coefficient              |
| $K$        | 10   | Number of Levels In Vertical              |
| $\Delta x$ | $9.0 \times 10^5$ cm                           | Cross-Shore Grid Spacing                  |
| $\Delta y$ | $1.1 \times 10^6$ cm                           | Alongshore Grid Spacing                   |
| $H$        | $4.5 \times 10^5$ cm                           | Total Ocean Depth                         |
| $\Delta t$ | 800 s  | Time Step                                 |
| $f_0$      | $0.86 \times 10^4 \text{ s}^{-1}$              | Mean Coriolis Parameter                   |
| $g$        | 980 cm s <sup>2</sup>                          | Acceleration of Gravity                   |
| $A_M$      | $2 \times 10^{17} \text{ cm}^4 \text{ s}^{-1}$ | Biharmonic Momentum Diffusion Coefficient |
| $A_H$      | $2 \times 10^{17} \text{ cm}^4 \text{ s}^{-1}$ | Biharmonic Heat Diffusion Coefficient     |
| $K_M$      | $0.5 \text{ cm}^2 \text{ s}^{-1}$              | Vertical Eddy Viscosity                   |
| $K_H$      | $0.5 \text{ cm}^2 \text{ s}^{-1}$              | Vertical Eddy Conductivity                |





## LIST OF REFERENCES

Ambar, I., Mediterranean influence off Portugal, in *Present problems of oceanography in Portugal*, Junta Nacional de Investigacao Cientifica e Tecnologica, Lisboa, 73-87, 1980.

Arakawa, A. and V. R. Lamb, Computational design of the basic dynamical processes of the UCLA general circulation model, *Methods Comput. Phys.*, 17, 173-265, 1977.

Barton, E. D., A filament programme in the Iberian upwelling region, *Coastal Transition Zone Newsletter*, 1, 2-5, 1986.

Batteen, M. L., Wind-forced modeling studies of currents, meanders, and eddies in the California Current System, *J. Geophys. Res.*, 102, 985-1009, 1997.

Batteen, M. L. and Y. -J. Han, On the computational noise of finite difference schemes used in ocean models, *Tellus*, 33, 387-396, 1981.

Batteen, M. L., C. N. Lopes da Costa, and C. S. Nelson, A numerical study of wind stress curl effects on eddies and filaments off the Northwest coast of the Iberian Peninsula, *J. Mar. Systems*, 3, 249-266, 1992.

Batteen, M. L. and J. T. Monroe, A large-scale modeling study of the California Current System, *Deep-Sea Res.*, submitted, 1998.

Batteen, M. L., and P. W. Vance, Modeling studies of the effects of wind forcing and thermohaline gradients in the California Current System, *Deep-Sea Res.*, in press, 1998.

Batteen, M. L., R. L. Haney, T. A. Tielking, and P. G. Renaud, A numerical study of wind forcing of eddies and jets in the California Current System, *J. Mar. Res.*, 47, 493-523, 1989.

Camerlengo, A. L. and J. J. O'Brien, Open boundary conditions in rotating fluids, *J. Comput. Phys.*, 89, 12-35, 1980.

Carton, J. A., Coastal circulation caused by an isolated storm, *J. Phys Oceanogr.*, 14, 114-124, 1984.

Carton, J. A. and S. G. H. Philander, Coastal upwelling viewed as a stochastic phenomena, *J. Phys Oceanogr.*, 14, 1499-1509, 1984.

Defense Mapping Agency Hydrographic/Topographic Center (DMAH/TC), *Sailing Directions (Planning Guide) for the North Atlantic*, DMA Pub. No. 140, Washington D. C., 390 pp., 1988.

Fiuza, A. F. de G., Circulation of the water of the Portuguese continental margin during the upwelling regime, Grupo de Oceanografia, Laboratorio de Fisica, Faculdade de Ciencias da Universidade de Lisboa, 1979.

Fiuza, A. F. de G., The Portuguese coastal upwelling system, in *Present problems of oceanography in Portugal*, Junta Nacional de Investigacao Cientifica e Tecnologica, Lisboa, 45-71, 1980.

Fiuza, A. F. de G., M. E. de Macedo, M. R. Guerreiro, Climatological space and time variation of the Portuguese coastal upwelling, *Oceanologica Acta*, Vol. 5, No. 1, 31-40, 1982.

Fiuza, A. F. de G., Upwelling patterns off Portugal, in E. Suess and J. Thiede (Editors), Coastal Upwelling. Its Sediment Record. Plenum Press, New York, pp. 85-97, 1983.

Fiuza, A. F. de G., Hidrologia e dinamica das Aguas costeiras de Portugal. Dissertacao apresentada a Universidade de Lisboa para obtencao do grau de Doutor em Fisica, especializacao em Ciencias Geofisicas. Univ Lisboa, 294pp., 1984.

Fiuza, A. F. de G. and F. M. Sousa, Preliminary results of a CTD survey in the Coastal Transition Zone off Portugal during 1-9 September 1988, *Coastal Transition Zone Newsletter*, 4, 2-9, 1989.

Folkard, A. M., P. A. Davis, A. F. de G. Fiuza, and I. Ambar, Remotely sensed sea surface thermal patterns in the Gulf of Cadiz and the Strait of Gibraltar: Variability, correlations, and relationships with the surface wind field, *J. Geophys. Res.*, 102, 5669-5683, 1997.

Frouin, R., A. F. G. Fiuza, I. Ambar, and T. J. Boyd, Observations of a poleward surface current off the coasts of Portugal and Spain during Winter, *J. Geophys. Res.*, 95, 679-691, 1990.

Hagen, E., C. Zulicke, and R. Feistel, Near-surface structures in the Cape Ghir filament off Morocco, *Oceanol. Acta*, 19, 6, 577-598, 1996.

Haidvogel, D. B., A. Beckmann, and K. S. Hedstrom, Dynamical simulation of filament formation and evolution in the coastal transition zone, *J. Geophys. Res.*, 96, 15,017-15,040, 1991.

Haney, R. L., A numerical study of the response of an idealized ocean to large-scale surface heat and momentum flux, *J. Phys. Oceanogr.*, 4, 145-167, 1974.

Haney, R. L., W. S. Shiver, and K. H. Hunt, A dynamical-numerical study of the formation and evolution of large-scale anomalies, *J. Phys. Oceanogr.*, 8, 952-969, 1978.

Haney, R. L., Midlatitude sea surface temperature anomalies: A numerical hindcast, *J. Phys. Oceanogr.*, 15, 787-799, 1985.

Haynes, R. and E. D. Barton, A poleward flow along the Atlantic coast of the Iberian Peninsula, *J. Geophys. Res.*, 95, 11425-11441, 1990.

Holland, W. R., The role of mesoscale eddies in the general circulation of the ocean-Numerical experiments using a wind-driven quasi-geostrophic model, *J. Phys. Oceanogr.*, 8, 363-392, 1978.

Holland, W. R., D. E. Harrison and A. J. Semtner Jr., Eddy-resolving numerical models of large-scale ocean circulation, II, in *Eddies in Marine Science*, edited by A. R. Robinson, 379-403, Springer-Verlag, New York, 1983.

Holland, W. R. and M. L. Batteen, The parameterization of subgrid scale heat diffusion in eddy-resolved ocean circulation models, *J. Phys. Oceanogr.*, 16, 200-206, 1986.

Ikeda, M., W. J. Emery, and L. A. Mysak, Seasonal variability in meanders of the California Current system off Vancouver Island, *J. Geophys. Res.*, 89, 3487-3505, 1984a.

Ikeda, M., L. A. Mysak, and W. J. Emery, Observations and modeling of satellite-sensed meanders and eddies off Vancouver Island, *J. Phys. Oceanogr.*, 14, 3-21, 1984b.

Levitus, S., and T. P. Boyer, World ocean atlas 1994, Vol. 4: Temperature, *NOAA Atlas NESDI 4*, 117 pp., U. S. Dept. of Commerce, Washington, D.C., 1994.

McClain, C. R., S. Chao, L. P. Atkinson, J. O. Blanton, and F. Castillejo, Wind-driven upwelling in the vicinity of Cape Finisterre, Spain, *J. Geophys. Res.*, 91, 8470-8486, 1986.

McCreary, J. P., Y. Fukamachi, and P. K. Kundu, A numerical investigation of jets and eddies near an eastern ocean boundary, *J. Geophys. Res.*, 92, 2515-2534, 1991.

McCreary, J. P., P. K. Kundu, and S. Y. Chao, On the dynamics of the California Current system, *J. Mar. Res.*, 45, 1-32, 1987.

Nelson, C. S., Wind stress and wind stress curl over the California Current, NOAA Tech Rep. NMFS SSFR-714, U. S. Dept. Commerce, 87 pp., 1977.

Pares-Sierra, A., W. B. White, and C. -K. Tai, Wind-driven coastal generation of annual mesoscale eddy activity in the California Current system: A numerical model, *J. Phys Oceanogr.*, 23, 1110-1121, 1993.

Pedlosky, J., Longshore currents, upwelling, and bottom topography, *J. Phys Oceanogr.*, 4, 214-226, 1974.

Philander, S. G. H. and J. H. Yoon, Eastern boundary currents and upwelling, *J. Phys Oceanogr.*, 12, 862-879, 1982.

Tomczak, M. and J. S. Godfrey, *Regional Oceanography: An Introduction*, Pergamon Press, New York, 422 pp., 1994.

Trenberth, K. E., W. G. Large, J. G. Olsen, The mean annual cycle in global ocean wind stress, *J. Phys Oceanogr.*, 20, 1742-1760, 1990.

Van Camp, L., L. Nykjaer, E. Mittelstaedt, and P. Schlittenhardt, Upwelling and boundary circulation off Northwest Africa as depicted by infrared and visible satellite observations, *Prog. Oceanog.*, 26, 357-402, 1991.

Weatherly, G. L., A study of the bottom boundary layer of the Florida Current, *J. Phys Oceanogr.*, 2, 54-72, 1972.

Wooster, W. S. and J. L. Reid, Jr., Eastern Boundary Currents in *The Sea, Vol. 2*, M. N. Hill, Ed., Wiley International, New York, 253-280, 1963.

Wooster, W. S., A. Bakun, and D. R. McLain, The seasonal upwelling cycle along the eastern boundary of the North Atlantic, *J. Mar. Res.*, 34, 131-140, 1976.

## INITIAL DISTRIBUTION LIST

|   | No. Copies |
|---|------------|
| 1. Defense Technical Information Center.....2<br>8725 John J. Kingman Rd, STE 0944<br>Ft. Belvoir, VA 22060-6218                  |            |
| 2. Dudley Knox Library .....2<br>Naval Postgraduate School<br>411 Dyer Rd<br>Monterey, CA 93943-5101                              |            |
| 3. Chairman (Code OC/Bf) .....1<br>Department of Oceanography<br>Naval Postgraduate School<br>Monterey, CA 93943-5122             |            |
| 4. Chairman (Code MR/Wx) .....1<br>Department of Meteorology<br>Naval Postgraduate School<br>Monterey, CA 93943-5114              |            |
| 5. Dr. Mary L. Batteen (Code OC/Bv) .....4<br>Department of Oceanography<br>Naval Postgraduate School<br>Monterey, CA 93943-5122  |            |
| 6. Dr. Curtis A. Collins (Code OC/Co).....1<br>Department of Oceanography<br>Naval Postgraduate School<br>Monterey, CA 93943-5122 |            |
| 7. Dr. Tom Curtin .....1<br>Office of Naval Research<br>800 N. Quincy Street<br>Arlington, VA 22217                               |            |

- 8. Dr. Tom Kinder .....1  
Physical Oceanography Division  
Office of Naval Research  
800 N. Quincy Street  
Arlington, VA 22217
  
- 9. LT Daniel W. Bryan.....2  
1840 Cox Rd  
Cocoa, Fl 32926